EXPERIMENTS AND PREDICTIONS WITH A FOIL THRUST BEARING SUPPORTED BY METAL MESH SCREEN

A Dissertation

by

TRAVIS ALEXANDER CABLE

Submitted to the Office of Graduate and Professional Studies of

Texas A&M University

in partial fulfillment of the requirements for the degree of

DOCTOR OF PHILOSOPHY

Chair of Committee,	Luis San Andrés
Committee Members,	Adolgo Delgado
	Junuthula N. Reddy
	Vikram Kinra
Head of Department,	Andreas A. Polycarpou

May 2020

Major Subject: Mechanical Engineering

ABSTRACT

Modern micro-turbomachines (MTM) often employ light weight rotors operating at speeds in excess of 50 krpm. These turbomachines require radial and thrust bearings capable of handling high speeds, while also often operating in extreme environments (high and low temperature). Flexible structure air bearings, or foil bearings, provide an economical and clean (no oil or contamination) means of rotor support in this niche.

To date, the most commonly utilized foil bearing is the bump-type foil bearing, which utilizes thin corrugated foil strips to support a smooth top foil on which hydrodynamic pressure builds. Despite its widespread use, each bump-foil is complex to build and model, requiring of extensive engineering knowledge and experience. As such, researchers continue to search for cheaper and less complex alternatives to the traditional bump-foil structure. Metal mesh, readily available and relatively cheap, is a viable option for radial foil bearings, but has yet to be investigated for use in foil thrust bearings.

The dissertation presents the design and manufacture of a novel Rayleigh-step thrust foil bearing, whose top foil is supported by a circular layer (or layers) of compliant metal mesh screen. Static and dynamic load excitation tests (no rotor speed) with the prototype bearing reveal a structural stiffness which increases with the mass ratio of the mesh screen and decreases with the number of mesh layers used to support the top foil. Dynamic load excitation tests, up to 300 Hz., give a material loss factor γ ~ 0.2 for the mesh structure which is relatively unaffected by frequency. Foil bearings rely on structural damping from material hysteresis, and bump-type foil

bearings exhibit a material loss factor which decreases quickly with an increasing excitation frequency, thus lending credence to metal mesh screen as a bearing support structure.

Despite the promise of the novel Rayleigh-step foil thrust bearing, experiments with rotor speed failed several of the prototype top foils, the root-cause of which is attributed to the waviness of the metal mesh layers. This waviness unevenly bulges the thin top foil towards the spinning collar, causing solid contact between the metal top foil and collar before hydrodynamic pressure builds over the pads to separate the surfaces. The failure of several prototype foils points to the need of a robust coating for foil bearings, which can not be ignored by designers.

Tests with a redesigned prototype, incorporating a circumferential taper and segmented pads, proved the bearing concept. A single pad bearing with a 55° arc extent and three layers of 40 OPI (openings per inch) mesh achieved a modest specific load of W/A = 35 kPa (per pad) at a rotor speed Ω = 40 krpm ($\omega \cdot R_{mid}$ ~ 160 m/s). Further tests with a six-pad circumferentially tapered metal mesh foil thrust bearing (MMFTB) determined an ultimate load capacity of W/A ~ 25 kPa for Ω = 40 krpm. At this load capacity, the bearing temperature rise (measured via a thermocouple on the top foil backside) exceeded 110 °C. The decreased load capacity for the six-pad bearing, as compared to the single-pad bearing, results from an uneven distribution of the thrust load between the six pads, as confirmed by temperature measurements on three of the top foil undersides. Similar to the Rayleigh-step top foil, the circumferentially tapered MMFTB suffered from taper height disparities between the pads, attributed to the waviness of the mesh, which is exacerbated by stacking multiple layers.

In addition to the experimental work with compliant surface thrust bearings supported by metal mesh screen, the dissertation provides a thermo-elastohydrodynamic model, validated (to some degree) with cases from the literature. However, bearing drag torque measurements and predictions for a six-pad MMFTB do not agree well. A simple Couette-flow approximation for the bearing drag torque shows that the bearing would need to operate with a uniform film thickness (h_{const} = 2.7 μm) to produce the measured bearing drag torque (T_{exp} = 180 N.mm). This minute film thickness is within typical combined roughness (rotor collar + pad roughness) values, and as such likely does not produce a full fluid film during operation. The simple analysis, along with post-test photographs of the thrust collar surface, corroborates the notion that the test bearing operated in the mixed-lubrication regime, with continuous sliding contact between asperities on the rotor collar and the pads coated with a sacrificial lubricant (MoS2).

A further analysis with the current model compares the steady-state performance of a MMFTB with 3 sheets of 40 OPI mesh to that of a well-known BFTB geometry from the literature. Predictions show that the MMFTB has a nearly identical drag toque to that of the BFTB for loads $10 \leq W/A \leq 50$ kPa and a large rotor speed Ω = 70 krpm ($\omega \cdot R_{mid}$ ~ 279 m/s), although it has a slightly smaller film thickness (and likely a lower ultimate load capacity).

Predictions with Ω = 70 krpm ($\omega \cdot R_{mid}$ ~ 279 m/s) and a specific load $W/A \leq 30$ kPa show that that the MMFTB operates slightly cooler than the BFTB (ΔT_{max} ~ 105 vs 115 K) when no cooling flow applies to the bearing. Applying cooling flow ($0 \leq Q_{cf} \leq 900$ LPM) through the bearing center can decrease the peak film and top-foil temperatures by ~ 40 °C, while decreasing the collar temperature by up to 10 °C. For the bearing geometry utilized in the current predictions (see Table 14), a cooling flow rate $Q_{cf} \geq 100$ LPM fully supplies the pad leading edge, such that the bearing draws no fluid from the ambient air surrounding the bearing. Increasing the cooling flow beyond this point cools the pads via forced convection in the areas beneath the pad tapers (albeit little). For the MMFTB, the mesh screens under the pad and in the land section obstruct cooling flow, such that the cooling is less effective (when compared to the BFTB). Importantly, utilizing an

aluminum collar (with a high thermal conductivity, κ = 130 W/m^2K) limits the thermal gradient through the collar thickness to 5 °C, reducing the possibility of thermal bending and a corresponding thermal runaway event.

The dissertation adds to the archival literature on gas foil thrust bearings and provides a model for prediction of their performance. The failures detailed herein provide important lessons for foil bearing designers and researchers. Further research is needed to either qualify or disqualify metal mesh sheets as a viable underspring structure for gas foil thrust bearings, although the following document provides several cautions against their use.

ACKNOWLEDGEMENTS

My most sincere thanks and gratitude go to my advisor, Dr. Luis San Andrés, without whose guidance, help and support, none of this would be possible. I am indebted to you for the training and the knowledge I gained during my tenure at the Turbolab. I truly consider myself blessed for the time, effort, and resources you invested in my development. Thanks also to the rest of my advisory committee, for reading and editing this work as well as for providing valuable insight along the way.

I acknowledge the Texas A&M Turbomachinery Consortium for financially supporting the majority of this work. I am also indebted to New Way Air Bearings for equipment donations and engineering expertise.

To my incomparably beautiful wife, I acknowledge your hand in this work. Your sacrifice, support and love made this possible. Your name should be right there with mine on the front-page Michelle. To both of our families, we could not have endured without your love, prayers and support.

To the Alpha and the Omega, the Beginning and the End, this was and is always yours.

CONTRIBUTORS AND FUNDING SOURCES

CONTRIBUTORS

This work was supervised by a thesis (or) dissertation committee consisting of Professor Luis San Andrés and Professors Adolfo Delgado and Junuthula N. Reddy of the Department of Mechanical Engineering and Professor Vikram Kinra of the Department of Aerospace Engineering.

FUNDING SOURCES

This work was funded in part by the Texas A&M University Turbomachinery Research Consortium.

Its contents are solely the responsibility of the authors and do not necessarily represent the official views of the Consortium.

NOMENCLATURE

A	Area [m^2]
c_p	Lubricant specific heat at constant pressure [kJ/(kg.K)]
D_h	Hydraulic diameter [m]
E	Elastic modulus [Pa]
g	Gravitational constant [m/s^2]
h	Film thickness [m]
$\overline{h}$	Heat convection coefficient [W/(m^2.K)]
K	Stiffness [N/m]
M	Mass [kg]
$\dot{m}$	Mass flow rate [kg/s]
n_{MM}	Number of metal mesh layers [-]
P, P_a	Pressure, ambient pressure [Pa]
Q	Shear force [N]
Q_s	Heat flux between film and bounding solids [W/m^2]
q_r, q_θ	Mean lubricant flow per unit width [kg/(s.m)]
$\dot{q}$	Heat flux [W/m^2]
R	Radius [m]
$\overline{R}$	Thermal inductance [(m^2.K)/W]
r, θ, z	Cylindrical coordinate system located at bearing center
T	Temperature [K]

T	Time [s]
U	Velocity [m/s]
$\bar{U}_r$, $\bar{U}_\theta$	Mean fluid flows [m/s]
V	Volume [m^3]
w	Top foil elastic deformation [m]
w_d	Wire diameter [m]
Θ_L	Angular distance from pad leading edge to step [°]
Ω	Rotor speed [rad/s]
β_T	Fluid volumetric expansion coefficient [1/K]
E	Permeability coefficient [-]
κ	Thermal conductivity [W/(m.K)]
μ	Dynamic viscosity [Pa.s]
ν	Poison ratio [-]
ρ	Density [kg/m^3]

Subscripts

a	Ambient
cf	Cooling flow
e, i	Exit, inner or inlet
MM	Metal mesh
TC	Thrust collar
tf	Top foil

TABLE OF CONTENTS

LIST OF FIGURES

LIST OF TABLES

1. INTRODUCTION

Micro-turbomachines (less than 400 kW) require of cost-effective and reliable rotor support elements, both axial and radial, for both high speed and severe (high or low) temperature applications. Oil-lubricated bearings are known for their large load carrying capacity; however, large parasitic (drag) losses at high speeds, and temperature limitations (both high and low) preclude their usage in specific applications, such as in cryogenic turbo expanders. In the early 1950's, Blok and Rossum [1] introduce compliant surface gas foil bearings, whose thin top foils elastically deform to handle rotor imperfections (such as mechanical runout) and thermal growth during operation.

Modern radial gas foil bearings employ a bearing cartridge, a smooth thin top foil(s) and a deformable underspring structure, manufactured in one of many varieties (corrugated, wing type, protuberant foils, etc.). Figure 1 depicts the components of a simple (Generation I) journal bump-type foil bearing (BFB) having a single corrugated bump foil layer, thin top foil and solid metal cartridge.

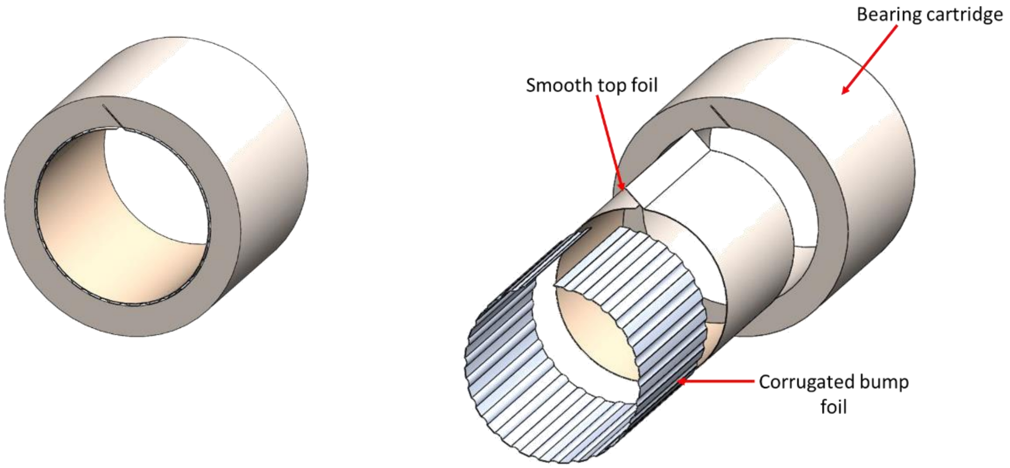

(a) Assembled (b) Exploded

Figure 1. Schematic views of a Generation I bump-type foil journal bearing showing both (a) an assembled view and (b) an exploded view, detailing the bearing components.

Hydrodynamic gas foil bearings utilize ambient air (or gas) as the lubricating fluid between a rotating shaft and a smooth, deformable top foil. The rotation of the shaft drags the lubricating fluid (gas in this instance) into a converging gap between the solid shaft and the compliant foil. The fluid flow through this converging wedge creates a positive pressure which lifts the rotor and allows it to float on the thin (a few micrometers) film. The damping and load capacity of this film depend on the lubricant viscosity; and as such, gas bearings tend to have a much lower load carrying capacity and (a miniscule) viscous damping compared to similar sized oil-lubricated bearings.

Instead of relying on viscous damping, gas foil bearings make use of compliant structures/materials (such as corrugated foils) to damp mechanical vibrations through frictional (Coulomb) and hysteretic material damping. Researchers continue to investigate different materials and geometries for a foil bearing underspring structure. Metal mesh dampers first became an alternative to traditional squeeze film dampers in the early 2000's [2]. Soon after, researchers incorporated metal mesh as an underspring structure in a gas foil bearing low cost and simple in manufacturing that demonstrated comparable performance to a bump-strip layer gas foil journal bearing (GFJB) [3].

Interest in GFJBs and gas foil thrust bearings (GFTBs), as shown by their presence in the literature, continues to increase. As early as 1969, GFJBs replaced rolling element bearings in aircraft air cycle machines (ACMs) [4]. In addition to air cycle machines, researchers have shown the promise of gas foil bearings (both radial and thrust) in micro gas turbines, small motor-generator systems, midsized aircraft gas turbine engines and turbochargers (TCs) for both passenger and commercial vehicles [4]. Recent research also shows promise for the implementation of MMFBs in small-size barrel-case centrifugal compressors and larger turbomachines [5-7].

In order to accommodate foil bearings in existing technologies, such as oil lubricated turbochargers, the diameter of the rotor at the journal bearing locations, as well as the diameter of any thrust collars, must increase to support the imposed axial and radial loads. Large diameter (OD ~ 100 mm) foil thrust bearings, such as those in Refs. [8], develop large temperature gradients due to local hot spots and asperity contact. These temperature gradients are affected by the bearing operating conditions as well as ambient conditions. After a certain point, large localized temperatures (or hot spots) can lead to thermal-runaway in a GFB and result in a decreased load carrying capacity and possibly catastrophic failure.

Reliable and cost-effective GFTBs will enable oil-free turbomachines with a lesser part count, better thermal efficiency and with lesser emissions (in the case of automotive turbochargers and turbofans). This dissertation develops a novel metal mesh thrust foil bearing (MMFTB) with dimensions and static properties (stiffness) identical to an open source GFTB [9]. After its completion, experiments on a dedicated test rig show the original design to be flawed, pointing to the inherent waviness of the mesh as an issue to overcome. A next iteration of the bearing design, incorporating a circumferential taper rather than a Rayleigh-step, supports a modest load (W/A ~ 5 psi) and proves the bearing concept. Finally, an existing isothermal computational model for bump-type foil bearings is extended to include thermal effects in the thin film and bounding solids.

2. LITERATURE REVIEW

2.1 FOIL THRUST BEARINGS

Thrust bearings maintain the axial position of rotating shafts in turbomachines, and as such, are integral mechanical components, requiring of thorough research and design. As in GFJBs, GFTBs incorporate a solid metal support, a compliant supporting layer (or layers) and a smooth metal top foil. Figure 2 displays a schematic of a simple (Generation I) bump type foil thrust bearing with six arcuate pads, each having a circumferential extent of 45°. Note that the thrust collar (not pictured) rotates counterclockwise to form the hydrodynamic wedge on each thrust pad. The bump foil strips (six in total) affix to the bearing support via either spot welds or some other simple fixing mechanism. This attachment method fixes the first (leading edge) bump while leaving the last (free end) bump free to displace along the circumferential direction.

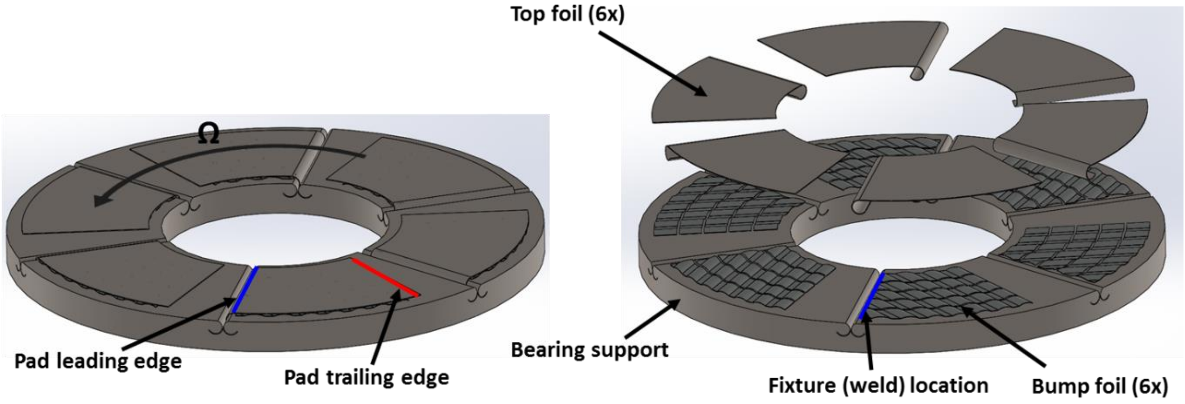

(a) Assembled bearing (b) Exploded view

Figure 2. Schematic of a bump type foil thrust bearing with six pads.

Beginning in the early 1980s Mohwak Innovative Technologies Inc. (MiTi), formerly MTI, became one of the leaders in the development of GFTBs. Heshmat *et al.* [12] provide a computational analysis of a GFTB with a single bump foil strip as the underspring structure. The authors determine the taper extent, taper height and pad angular extent which deliver the maximum load carrying capacity with an isothermal (and thus isoviscous) ideal gas and a uniformly distributed (constant) bump foil stiffness. Results show that for a foil thrust bearing with an OD to ID ratio of 2:1, the optimum geometric configuration has a pad with an angular extent of 45°, a taper height that exceeds 10 times the minimum film thickness on the land section, and a taper extent that equals to half the pad length (in this case $\beta = 22.5°$).

Extending the analysis from Ref. [12], Heshmat [13] evaluates the performance of a bump-type GFTB considering a linear variation (in the circumferential direction) of the bump foil stiffness from the foil fixed end to free end. Results show that when the dry-friction coefficient is small (μ~0), the bump-stiffness is uniform from the fixed end of the foil to the free end. Increasing the friction coefficient stiffens the foil, producing a nonlinear stiffness variation from the fixed end to the free end. For a foil thrust bearing with the optimum configuration forwarded in Ref. [12], a foil with its first bump being ~3 times stiffer than the last bump yields a bearing with the largest load capacity.

Ku [14] presents experiments aimed at determining the structural dynamics (stiffness and Coulomb damping) of a corrugated bump-foil strip for thrust foil bearings. In the paper, Ku utilizes a test rig consisting of an extensometer, dynamic load cell and hydraulic shaker to apply dynamic sinusoidal loads to a bump foil strip, measuring the resulting load and displacement. In the study, the bump foil and top foil are Inconel X-750 and are coated with either copper or Teflon to investigate the effect of the friction coefficient on the foil dynamics. Results for a fixed (low) excitation frequency (Ω = 1Hz) show that increasing applied static load or decreasing dynamic motion amplitude increases structural stiffness. In addition, Coulomb damping decreases with increasing motion amplitude.

Following the work of Hesmat [13], Iordanoff [15] presents an analysis of a bump-type GFTB including an analytical model as well as experimental results. His bump-type GFTB has multiple sectors in which the bump foil is welded to a bearing support at the sector's leading edge, and free at the sector trailing edge (as in Figure 2). The forwarded model calculates the compliance of both the fixed bump, and free bump assuming a linear variation of the bump compliance between these two bumps. For a GFTB with eight sectors (pads), an ID = 40 mm, OD = 80 mm, rotor speed comprised between Ω = 20-50 krpm, and a pad angular extent of 40°, results show that the tapered section should extend ~17° and have a height of 84 μm to optimize load capacity and reduce drag torque. Experimental results match well with predictions from the analytical model when the minimum film thickness is ~3 μm; however, the model over-predicts bearing power loss at low loads.

Beginning in the early 2000s Case Western Reserve University and the National Aeronautics and Space Administration (NASA) embarked on a concerted effort to elucidate the performance of Gen. I bump-type GFTBs. The first of a near decade long collaboration, Bruckner [16] presents an elasto-thermohydrodynamic model and experimental analysis of a GFTB with 8 pads. The analysis marks the first in the literature in which the author includes the energy equation in the thin film to predict the performance of bump-type GFTBs. Bruckner solves the coupled set of partial differential equations governing the generation of hydrodynamic pressure in the lubricated zone (Reynolds equation), elastic deformation of the top foil (bending dominated membrane) as well as the heat transfer in the lubricated zone (energy transport equation) to predict the bearing performance. The dissertation [16] focuses mainly on the development of the model with only a few predictions for an actual bearing, and even less experimental data. The few predictions show that the step-wise structural stiffness of the bump foil causes local high-points where metal-to-metal contact between the thrust collar and top foil is likely. Experiments corroborate predictions, showing wear on each pad near its center.

Dykas [17] and Dykas *et al.* [8] add to the literature on the Gen. I bump-type GFTB, presenting experimentally determined bearing drag torque, load capacity and pad temperature rise for increasing thrust collar speeds (Ω = 25-55 krpm). The test bearing(s) in the research is an 8-pad bump-type GFTB with a total pad area of $A_{bearing}$~44 cm^2. Load capacity measurements show that the bearing can support specific loads (W/A) up to ~100 kPa. Interestingly (and counterintuitively), the reported load capacity decreases with increasing rotor speed when the bearing is uncooled. Introducing cooling flow increases the overall load capacity for a given operating speed. Measurements of the bearing power loss (drag torque · rotational speed) versus applied load show that the power loss is low (less than 1 kW) for all speeds and loads (up to 100 kPa) and increases nearly linearly with applied load and rotor speed. A major takeaway from Refs. [8, 17] is that rotor thermal growths limit load carrying capacity in uncooled bearings.

Dykas *et al.* [9] present a detailed manufacturing method for a Gen. I GFTB to further disseminate information and encourage the use of gas foil bearings in more applications. The authors detail the necessary design tools and molds for construction of the top and bump foils along with their geometries, materials and advice on heat treatment. Brief experiments with the manufactured foil bearing show that the bearing operates with a small drag torque (less than 100 N.mm) and a moderate (W/A~27 kPa) load capacity for a rotational speed Ω = 23 krpm. The work is unique in the literature, providing a truly open source users guide for the construction of a GFTB.

Work by Dickman [18] and Stahl [19] completed the collaboration between Case Western and NASA. Dickman [18] presents load capacity and bearing drag torque measurements for three bump-type GFTBs, identical in manufacturing process and geometry. Experiments with the six-pad GFTB show that although the bearing geometry and manufacturing process was well controlled, for rotor speeds up to 40 krpm the three bearings vary in load carrying capacity by ~30%, a large margin. Further tests for one bearing show that the drag torque is proportional to rotor speed and also increases linearly with the applied axial load. In addition to the tests with the six-pad bearing, tests with a four-pad GFTB yields a decreased drag and load capacity, but better thermal stability.

Stahl [19] evaluates the drag torque and load capacities of three six-pad GFTBs, extending the measurements from Ref. [18] to include a rotor speed range comprised between Ω = 40-70 krpm. Results from Stahl corroborate the measurements presented in Ref. [19], showing that the bearing drag torque continues to increase linearly with applied load, even for high (above 40 krpm) rotor speeds. For speeds Ω = 40-70 krpm and specific loads between W/A = 0-15 psi, the bearing torque is small (less than 100 N.mm). Stahl also investigates the interchangeability of top foils and bump foils from one bearing to the next. Load capacity testing for bearings with intermixed foils shows that friction factor between the bearing support and bump foils to be of primary importance for increased load capacity.

Balducchi *et al.* [10] evaluate the lift-off speed, drag torque and bearing temperature rise for a six-pad bump-type GFTB, manufactured to the specs and in the manner outlined in Ref. [9]. The authors instrument each of the six pads with a single thermocouple, located near the pad's OD and the angular midspan. Tests for rotor speeds between Ω = 20-35 krpm and for small specific loads $W/A \leq 13$ kPa show that the pads have a non-uniform temperature rise, attributed to manufacturing abnormalities from one pad to the next. The reader gains little quantitative information on bearing temperatures or drag torque, as plots display both quantities in dimensionless form. Quantitatively, results show that the start-up/shut-down dimensionless torque increases linearly with the applied axial load. Unexpectedly, a large bearing temperature rise initially prevented operation for more than 2 minutes. An addition of several thru holes in the test bearing holding mechanism at the pads leading edges, allowed for passive cooling and a thermally stable operation for longer periods of time.

In a follow-up paper to Ref. [10], Balducchi *et al.* [11] evaluate the dynamic axial stiffness and equivalent damping of the same six-pad GFTB from Refs. [9, 10]. The authors modify the test rig from Ref. [10] to include an electromagnetic shaker which excite the test bearing in the axial direction. Before spinning the thrust collar against the test bearing, the authors determine the foil bearing's structural stiffness for increasing loads from $W/A = 6.5 – 32.5$ kPa, showing the structural stiffness to be similar to the bearing from Ref. [9]. A multifrequency waveform (from 200-750 Hz) applies to the test bearing, while a dynamic load cell records the dynamic load, three eddy current sensors record the bearing relative displacements and 3 accelerometers record the absolute accelerations. A dynamics model in conjunction with the measured data delivers axial force coefficients (stiffness and damping) for the bump-type GFTB. Results show that the damping is small (less than 500 N.s/m) and decreases with increasing excitation frequency, while the stiffness is large (2-30 MN/m) and increases with frequency. With the thrust collar spinning at $\Omega = 35$ krpm, a similar procedure shows that the structural stiffness acts in series with the fluid film stiffness, decreasing the overall bearing stiffness for a given load. In addition to the bearing stiffness, Balducchi *et al.* [11] report a material loss factor (a measure of material damping in a foil bearing) of ~0.2.

The works of Stahl [19] and Balducchi *et al.* [10, 11] represent only a small subset of the work on GFTBs over the past decade. Other researchers, to date, continue to push the envelope and the state-of the art for bump-type GFTBs [20-26]. The recent research focuses on ever more complex thermal models for these GFTBs as well as accounting for turbulence in the thin film. Several of the most recent papers have also focused on top foil sagging effects, operation with contaminants and debris, axial dynamic force coefficients (K, C) and the feasibility of applying foil bearing technologies into existing turbomachines [21-27].

Despite the dominance of the bump-type foil underspring structure, authors have also experimented with non-traditional materials and geometries. Somaya *et al.* [28] present experiments and predictions for a six pad thrust foil bearing with top foils supported by a viscoelastic silicon rubber layer. Ref. [28] shows the bearing to be easily assembled and capable of supporting an 84 kPa (~12 psi) specific load at a rotor speed of 20 krpm ($\omega \cdot r_{mid}$ ~80 m/s). However, this viscoelastic supported bearing is only applicable in mild temperature (less than 100 °C) environments. Zheng *et al.* [29] assemble a novel foil thrust bearing with multiple bronze foils, the lower foils having small dimples (protuberants) which act as stiffness elements. Experiments with eight different bearings proved the bearing concept, showing the protuberant foil bearing to have a maximum load capacity of 92 kPa (~13.3 psi) at 85 krpm ($\omega \cdot r_{mid}$ ~147 m/s). Yet to be proven in an actual machine, the protuberant foil design shows promise, but is still time intensive to manufacture as it contains multiple components. Most recently, Lai *et al.* [30] propose a thrust foil bearing with multiple foils, supported by a few (five at the most) small diameter copper wires. Although the paper is primarily computational, brief experiments show the copper wire supported foil thrust bearing (CWFTB) can withstand at least a modest 30 kPa (~4.4 psi) specific load at a rotor speed of 100 krpm ($\omega \cdot r_{mid}$ ~141 m/s). As with the protuberant foil bearing, the

CWFTB contains multiple foils, introducing complexity in modeling (as well as assembly), and is yet to be proven for loads in excess of 30 kPa.

2.2 THERMAL EFFECTS IN FOIL BEARINGS

As described in the previous section, early research on foil bearings (both radial and thrust) focused primarily on characterizing the bump foil undersrping structure as well as forwarding models which considered fluid-structure interactions. These models, increasing in complexity to bring model predictions closer to experimental measurements, initially ignored temperature effects in the thin film [13,15], or used an overly simplified energy equation [16]. Near the turn of the century, and the advance in computing power, researchers began investigating thermal effects in foil bearings in greater detail. Due to the complexity of the problem and thermal subsystems surrounding the foil bearing itself, research on the topic continues to this day.

Pinkus [31], in his book on *Thermal Analysis of Fluid Film Tribology* provides a comprehensive analysis of the physics in thin film flows, focusing on developing the governing equations and modeling thermal effects in fluid film bearings. Pinkus discusses several forms of the energy equation, detailing a simplified form for a compressible fluid and ideal gas, further simplified by considering only diffusion (second order) temperature gradients and advection (first order) velocity gradients across the thin film. A Couette Approximation (pressure extrusion terms are much less important than those due to fluid shear) of this simplified energy equation decouples the Reynolds and energy equations, leading to a more simplistic solution methodology for the governing equations. This equation became the basis for gas bearing thermal analyses in the literature near the turn of the 21st century.

Salehi *et al* [32] detail an experimental and theoretical analysis of a 100 mm diameter bump-type foil journal bearing (BFJB) for surface speeds up to ~157 m/s and specific loads (*W/A*) up to 76 kPa (~ 11 psi). The theoretical analysis solves the compressible fluid Reynolds equation, and a bulk flow Coutte Approximation of the energy equation to deliver bearing pressure and temperature fields for increasing rotor speeds and specific loads, as well as for increasing amounts of cooling flow across the bearing axial length. The model utilizes empirical temperature boundary conditions, measured during the parallel test program, to determine the amount of conduction into the rotating journal and the elastic top foil and bump foil structures. Five K-type thermocouples affix to the backside of the thin top foil, and at different circumferential and axial locations to determine the temperature field around the bearing surface. Results show a linear increase in maximum temperature rise with rotor speed, and a slight increase with applied load. For the range of applied loads ($19 \leq W/A \leq 38$ kPa) and speeds ($52 \leq R \cdot \omega \leq 157$ m/s), the maximum bearing temperature rise doesn't exceed 45 °C for a 60-minute test. A comparison of predicted and measured bearing temperature rise shows a maximum deviation of 15%, indicating that the simplified thermal model decently captures the physics in the thin film, but can still be improved upon.

Radil and Zeszotek [33] present an experimental analysis of a Gen III radial foil bearing for journal speeds comprised between 20-50 krpm ($52 \leq R \cdot \omega \leq 131$ m/s) and loads up to 222 N (*W/A* ~ 35 kPa). Nine K-type thermocouples instrument the test foil bearing, affixing to the backside of the bump foil, which is in contact with an Inconel top foil. Tests at four different speeds, and step-wise loads from 9 - 222 N (1.4 – 35 kPa), show that the fluid temperature is largest at the bearing midspan, decreasing towards its axial edges. Further experiments with the Gen. III bearing show that the foil temperature is more sensitive to the rotation speed than to the applied load, as with other bearings in the literature [15,17,18].

Bruckner [16], the first researcher in a decade-long collaboration between Case Western Reserve University and NASA, contributes a thermo-elastohydrodynamic model for bump-type foil thrust bearings, coupling the hydrodynamic pressure field to the heat generated in the thin film and to the elastic deformation of the top and bump-foil structures. The dissertation also presents brief test data for an eight-pad Gen. I BFTB with ID = 23 and OD = 45 mm. Because of the minute film thicknesses, the model includes gas rarefication effects by introducing slip boundary conditions, defined with the film Knudsen number, at the thrust collar and top foil surfaces. The model also simplifies heat transfer in the film and bounding solids by considering a constant temperature (and lubricant properties) across the film thickness and a simple approximation for heat transfer to the bounding solids. Bruckner [16] presents analyses of several one-dimensional bearing geometries (Rayleigh-step, taper-land, double-taper) before displaying predictions for the eight-pad BFTB. Since the dissertation does not provide a detailed model of heat transfer within the bounding solids, predictions including temperature effects consider adiabatic bounding surfaces (no heat conductive heat transfer to runner or bump/top foils). Figures display dimensionless, pressure, film thickness, and bearing drag torque, giving only qualitative information of the fields over a bearing pad. Burckner claims that the load capacity of the 8-pad bearing operating at Ω = 25 krpm is 414 kPa (60.1 psi) and with a drag torque of 46 N.mm.

Dykas and Radil [34] and Dykas *et al.* [8] continue the collaboration between Case Western and NASA, presenting pad temperature measurements for the same 8-pad Gen. I BFTB investigated by Bruckner [16]. Dykas and Radil [34] first instrument a single thrust bearing pad with three thermocouples at increasing radii and attached to the backside of the bump foil structure.

Experiments with rotor speeds from 25 – 65 krpm ($60 \leq R_O \cdot \omega \leq 125$ m/s) show that the bump-foil temperature gradient (from inner to outer radii) increases with rotational speed and approaches ~2.5 °C/mm for a power loss as small as 450 W. Load capacity tests with the 8-pad bearing show that the bearing load capacity decreases with increasing rotor speed (after a certain point) when no cooling flow applies to the bearing, displaying an effect known as thermal runaway. The authors posit that thermal gradients within the thrust collar and the foil cause elastic deformations of the rotating collar, which increases the local film thickness near the pad OD and leads to a lower load capacity. Results show that applying cooling flow to the bearing increases the bearing load capacity for a given rotational speed and delays the onset of thermal runaway (with respect to rotor speed). The experimental results in Refs. [8,34] point to the importance of thermal effects in not only the thin film, but the thrust runner and compliant underspring structure as well.

San Andrés and coauthors [35-39] present several analyses (experimental and analytical) over a five-year period, focusing on the performance of Gen. I and Gen. II BFJBs operating in hot environments and with increasing amounts of cooling flow. The analyses by San Andrés, Ryu and Kim [36-38] provide a comprehensive data set and analytical model for accurate prediction of the performance of bump-type foil journal bearings.

First, Kim *et al.* [35] characterize the structural stiffness and material damping (i.e. loss factor) of a corrugated bump foil, at increasing temperature (up to 188 °C) and applied load (up to $W/A = 6.75$ kPa). The results show that the bump-foil dynamic stiffness increases with applied load and excitation frequency, due to a stick-slip phenomenon, and decreases with increasing temperature. The bump foil equivalent viscous damping, on the other hand, is inversely proportional to the applied load, excitation frequency and foil temperature. An alternative

Coulomb damping model gives a dry friction coefficient which increases with both applied load and excitation frequency, thus giving credence to the idea that “bump stick” increases with both.

San Andrés and Kim [36] present a thermohydrodynamic model benchmarked versus experimental measurements by Radil and Zeszotk [33]. The thermal model includes a bulk-flow energy equation (integrated across the film) as well as conduction from the thin film to the bounding solids (rotating journal and top foil surface), and convection from the bounding surfaces to ambient (or cooling flow streams). Effective thermal resistances simplify the heat flow paths to the journal (and then to ambient) as well as to the foil (and then ambient or cooling flow). Importantly, the model accounts for centrifugal and thermal growths of the shaft for prediction of accurate bearing clearances. Despite a lack of full geometric information, a comparison predictions and measurements of foil temperature for a Gen III foil bearing from Radil and Zeszotk show good agreement, thus validating the predictive model.

San Andrés *et al*. [37-38] provide a two-part analysis of a lightweight rotor (1.065 kg) supported by two Gen II BFJBs, focusing on its rotordynamic performance at elevated rotor temperatures and with increasing amounts of cooling flow. Part I [37] gives rotor displacement measurements at both free and drive ends of the rotor operating with surface speeds to 60 m/s and a low specific load of ~1.5 kPa (imposed by the rotor weight). Increasing heat decreases amplitude of rotor vibration below the system first critical speed (13 krpm) and increases the overall coast-down time, indicating operation with a minute drag. Experiments with increasing amounts of cooling flow indicate that a laminar cooling flow is more effective than a turbulent one, and that cooling flow is only effective at elevated operating temperatures (200 °C for example).

In Part II of the two-part analysis, San Andrés *et al*. [38] utilize the thermohydrodynamic model from Ref. [36] in conjunction with an in-house rotordynamic program to predict shaft motions for the rotor-bearing system described in [37] and rotor surface speeds up to 60 m/s. Predictions and measurements are in good agreement for bearing temperature rise, again, validating the simple thermal model. Predictions show bearing direct stiffness increases with rotor speed and heater temperature (due mainly to decrease in operating clearances caused by rotor and cartridge thermal growths). Equivalent viscous damping decreases with increasing rotor speed but increases with heater temp. Rotordynamic measurements and predictions at both the drive and free ends match well for speeds below 20 krpm but diverge from 20 – 30 krpm.

Ryu and San Andrés [39] detail the failure of the same lightweight rotor in Refs. [37,38] supported by two Gen II BFJBs due to a lack of applied cooling flow, and operation at high temperature. With operation at 37 krpm ($R_O \cdot \omega$ ~ 74 m/s) a cartridge heater (inserted into the hollow rotor) increased the bearings' operating temperature in fixed increments, over a period of 60 minutes, allowing the rotor-bearing system to reach thermal equilibrium. During the tests, infrared thermometers measured the temperature of the rotor OD at the free and drive ends, while thermocouples measured bearing and housing temperatures. Note that fiberoptic sensors also measured the rotor horizonal and vertical motions at both free and drive ends. After ~3 hours of operation, an increase in the cartridge heater temperature (to ~600 °C) caused a rotor seizure event, failing the free end bearing (where the rotor temperature was the highest). Surprisingly, neither the rotor temperature, nor shaft vibration measurements, hinted to the impending seizure, during testing. A simple analysis to predict the top foil temperature during solid contact between the rotor and top foil show that the top foil temperature approaches its melting point over a period of ~15 s. While the analysis is simplistic in nature, though physically sound, the results show that preventative measures could be taken to avoid foil bearing failures, if the bearing is instrumented at the proper locations. Ref. [39] shows, above all, that adequate thermal management for foil bearings (usually achieved by the application of cooling flow) is essential to their reliable operation at elevated temperatures.

Lee and Kim [40] provide the first analysis of a BFJB considering a full three-dimensional energy equation in the thin film as well as thermal energy transport equations for the bounding solids (rotating journal and compliant foundation). The thermal model of the top foil assumes conduction only occurs in the radial direction (across its thickness). At the backside of the top foil, heat conducts through the bump foil, governed via a thermal resistance per bump (empirically determined). In addition, heat convects from the back of the foil (to either ambient or a cooling flow stream) in the areas between bumps. The analysis considers a hollow rotor whose temperature varies along the radial and axial directions (constant shaft temperature in circumferential direction for a given axial location). Numerical predictions show a top foil temperature which closely resembles that of the (average cross-film) temperature, with a maximum at the pad axial midspan (as shown in several experimental analyses [32,33]). The authors benchmark the model with experimental data from Ref. [33], showing good agreement despite a lack of information on the proprietary bearing design (bump foil geometry for example). Further predictions with the model show a significant (~ 15 °C) axial temperature gradient across the rotor length for operation with a surface speed of 37 m/s and under a specific load W/A ~ 9 kPa. Results also show that more heat transfers to the rotor than the top foil when no cooling flow applies to the bearing. For increasing amounts of cooling flow across the bearing axial length, more heat transfers through the foil thickness and to the cooling flow streams. Most importantly, predictions show a pronounced influence on the temperature boundary conditions, indicating the necessity of appropriate heat convection coefficients in the accurate modeling of foil bearings.

Lee and Kim [41] extend the TEHD model from Ref. [40] to predict the performance of a Rayleigh-step bump-type foil thrust bearing, operating in an enclosed plenum and with increasing amounts of cooling flow. The analysis solves a 3D energy equation in the thin film, as well as energy equations for the bounding solids and also for the plenum enclosure. Ref. [41] presents a significant advancement in the state-of-the-art, solving for the air temperatures and mass flows surrounding the foil bearing in order to provide accurate thermal boundary conditions for the solids and thin film. Although the model does include temperature effects in the rotating thrust collar, the authors simplify the situation by considering a constant temperature through the collar thickness and circumferential directions. For a constant load applied load W/A = 30 kPa, predictions show the thrust collar temperature increases from ~ 140 °C to ~ 290 °C for surface speeds of $\omega\cdot R_{mid}$ = 172, 259 m/s, respectively. Even at a high surface speed ($\omega\cdot R_{mid}$ = 259 m/s), the rotor collar temperature varies by only ~10 °C from its center to the outer diameter. In Ref. [41], two BFTBs bound the thin (5 mm) rotor collar (one on each side). Due to heat inputs on both sides of the rotor collar, a simple model for the thrust collar thermal expansion shows that the collar expands towards the bearing surface by more than 40% of the film thickness. Further predictions show a film temperature which is relatively constant in the land section but does vary across the film thickness in the portion before the Rayleigh-step. In addition, predictions show that the temperatures of the bounding solids are more sensitive to the rotor speed than to the applied load.

Lehn *et al.* [42] and Lehn [43] detail a complex TEHD analysis for BFTBs, including thermal effects in the bounding solids as well thermally induced elastic deformations of the thrust collar governed by the constitutive equations for a linear elastic solid (for small displacements). The analysis in Ref. [42] extends the earlier analysis of Lee and Kim [41] by including an analytical model for the contact resistance between bump and top foils along with including realistic thermally induced deformations of the rotating collar. Predictions for a 6-pad BFTB operating with a minimum film thickness (undeformed) of 5 μm show that the rotor collar experiences thermal bending away from the bearing surface and increasing with surface speed. At a surface speed of $\omega \cdot R_{mid}$ = 115 m/s, the maximum thermal deflection occurs at the collar (and pad) outer diameter and equals 7 μm. For very large surface speeds ($\omega \cdot R_{mid}$ = 337 m/s), the maximum thermal deformation occurs at the pad center, exceeding 15 μm. Predictions show that the bearing load capacity increases with rotor speed to a certain point, after which, increasing speed decreases the bearing load capacity. Experimental data presented by Dickman [18] and Stahl [19] show a similar behavior, lending credence to the concept that this decrease in load capacity (termed thermal runaway) is indeed due to the thermal bending of the collar.

In a follow up paper, Reiken *et al*. [44] utilize the TEHD model from Refs. [42,43] to analyze a six-pad BFTB having top and bump foils made from high thermal conductivity metals. The authors investigate three different metals for use in foil bearings: Inconel X-750 (E = 210 GPa, v = 0.30 & κ = 12 W/m.K), DURACON® (E = 180 GPa, v = 0.30 & κ = 55 W/m.K), and CuNi1Si (E = 147.5 GPa, v = 0.325 & κ = 250 W/m.K). For a rotor speed Ω = 120 krpm ($\omega \cdot R_{mid}$ = 286 m/s) and a minimum film thickness h_{min} = 5 μm, predictions show that the maximum top foil temperature rise ΔT_{max} ~ 240, 205 & 180 K, for the Inconel, DURACON® and CuNi1Si foils, respectively. As shown in their previous paper [42], high temperatures in the fluid film induce thermal deformations of the thrust collar away from the bearing surface and reaching a maximum at the collar outer radius. Utilizing the CuNi1Si foil (κ = 250 W/m.K) decreases this thermal deformation by 33% when compared to the bearing operating with Inconel foils (10 μm versus 15 μm). A collar with less thermal distortion has a smaller film thickness across the thrust pad, and consequently, increases the bearing load capacity by ~10% (when compared to the bearing operating with Inconel foils). Without the addition of cooling flow to the bearing, it operates too hot ($\Delta T > 150$ K), even with the CuNi1Si foil. However, the addition of high thermal conductivity foils does aid in passive cooling and may be used in tandem with forced cooling to manage thermal effects in foil bearings (not studied in the current work).

Qin *et al.* [45] utilize commercial software to present a TEHD analysis of a BFTB which considers the momentum and energy transport equations in the thin film along with energy and structural deformation equations in the bounding solids. The model considers only a single bearing pad with dimensions and operating conditions giving by Dickman [18]. Predictions for the single pad bearing involve a complex coupling scheme between the fluid flow, thermal, and structural deformation equations. Note that a single numerical simulation, utilizing a personal computer (PC), executed on 12 cores (simultaneously) and a 2.5 gigahertz (GH) processor, requires a computation time between 10 and 15 days. The authors present a comparison of the bearing performance operating with $\Omega = 21$ krpm ($\omega \cdot R_{mid} = 42$ m/s), $W/A = 24$ kPa with either air and CO_2 as the working fluid. Results show that the majority of the heat (~90% for operation with air) convects to the rotating collar. Due to the low density and thermal conductivity of air, the circumferential flow only carries away ~3% of the total heat generated by fluid shear and pressure extrusion. In the case of CO_2, increased fluid density and thermal conductivity increase the amount of heat carried away by the fluid, when compared to operation with air as the working lubricant (30% versus only 3%). Results show that while all of the thermal subsystems surrounding the thrust bearing pad are important, correct modeling of the heat flow through to the rotating thrust collar is essential for accurate prediction of the temperature field in a foil thrust bearing. The analysis in Ref. [44] does not consider thermal deformations of the thrust collar, but the more detailed dissertation by Qin [45] notes that including collar thermal deformations is essential for high rotor speeds (50 krpm or greater).

2.3 METAL MESH DAMPERS AND BEARINGS

The underspring structure in GFBs dissipates mechanical energy through Coulomb (frictional) damping and material hysteresis. The bump-type foil bearing, although the most prevalent in the literature, is expensive to manufacture, requiring of precision-made dyes and engineering expertise for design. In addition, the bump crests are narrow and provide only a small area for heat conduction to the thrust bearing support. Researchers continue to forward alternatives to the typical bump-foil, one such alternative being metal mesh.

Hara [47] first investigates the frictional damping capabilities of steel metal mesh, showing the material held promise for numerous applications. In the early 2000s, John Vance and his students [48, 49] as well as Ertas [50, 51] thoroughly investigated the structural properties (stiffness and damping) of metal mesh dampers. Refs. [47-51] show that metal mesh dampers have similar damping capabilities to similar sized squeeze-film dampers. In addition, the damping inherent to the metal mesh structures is relatively insensitive to excitation frequency, temperature, or oil entrainment. Metal mesh material dampers are also relatively inexpensive and much less complex when compared to squeeze-film dampers. Extending the work on mesh dampers, Ertas [6] first implemented two metal mesh dampers into a compliantly damped hybrid (hydrostatic and hydrodynamic) gas bearing, showing that the 110 mm ID bearing had promise for implementation in moderately sized turbomachines.

Around the same time, San Andrés and Chirathadam [52] first implement metal mesh as a *true* underspring structure in a small (42 mm ID) hydrodynamic foil bearing. A comparison of the performance of the small metal mesh foil bearing (MMFB) performance to that of a similar sized bump-type foil journal bearing shows that the MMFB has a larger material loss factor (measure of energy dissipation) as well as an earlier lift off speed and slightly lower operational drag torque when compared to the BFB [3].

Feng *et al.* [53] present a small diameter (ID ~ 37 mm) hybrid metal mesh bearing consisting of metal mesh blocks placed in-between the bumps of a typical bump-type foil bearing. The hybrid MMFB shows improved damping capabilities when compared to a similar sized bump-type foil bearing. In addition to Ref. [51], Feng *et al.* [54] forward the only analytical model in the literature for the deformation of a metal mesh underspring structure, showing that predictions from the model correlate well with experimental static load versus deflection data.

With an increased interest in MMFBs, researchers attempted to extend the technology to larger tubomachinery applications. De Santiago and Solórzano [5] present temperature measurements of two identical large diameter (ID = 90 mm) hydrodynamic MMFBs supporting a 57 kg rotor (W/A ~ 12 kPa per bearing) with five centrifugal compressor impellers and a balance drum. Before a failure of the free end bearing, attributed to bearing top foil coming disconnected, the two MMFBs effectively supported the compressor rotor to a speed on 9 krpm (surface speed $R\Omega$ ~ 43 m/s). Recently, Delgado [7] reports dynamic force coefficients for a large (ID = 110 mm) compliantly damped hybrid gas bearing utilizing two metal mesh dampers. Measurements indicate that the bearing has adequate damping and can accommodate vibration amplitudes larger than the machined bearing clearance, due to the compliance of the bearing pads.

Most recently, Zhang *et al.* [55] present a thermo-elastohydrodynamic model for the hybrid metal mesh journal bearing in Ref. [53]. The authors utilize a test setup involving a small (1.25 W) electric heater and two K-type thermocouples to determine the thermal resistivity of the bump-foil and metal mesh blocks of the hybrid bearing. For stainless steel metal mesh blocks having 40% compactness, the test setup revealed a mesh thermal resistivity of R_{MM} ~ 2 K/W (i.e. κ_{MM} ~ 1.6 W/m.K) which is approximately ten times smaller than that of the base metal itself. Predictions match well with experimental data, showing a larger temperature at the bearing midspan. With no applied cooling flow, most of the heat conducted into the top foil conducts through the mesh bumps. When cooling flow applies to bump-foil channels underneath the top foil, more heat transfers to the bump foil, and conducts to the bearing housing as well as convecting to the cooling flow stream. Predictions show that even with the forced cooling flow to the hollow rotor center, as well as to the bearing substructure, peak film temperatures can reach up to 400 °C for $R\cdot\omega$ = 188 m/s and W/A = 93 kPa (~13.5 psi).

Researchers are still in search of an underspring material for compliant surface foil bearings which provides adequate stiffness and material damping as to enhance bearing load capacity and attenuate axial vibrations. The underspring structure should include paths for forced cooling flow and be simple to manufacture and implement. Metal mesh screen, readily available and cheap to procure, is an interesting alternative to the various materials and geometries researched in the past. As previous researchers [3,5,6] have utilized metal mesh in radial bearings (large and small), its extension to foil thrust bearings should be investigated.

3. DESIGN AND MANUFACTURIING OF A METAL MESH FOIL THRUST BEARING AND A TEST RIG FOR ITS EVALUATION[1]

3.1 A RAYLEIGH-STEP METAL MESH THRUST FOIL BEARING

In 1918 Lord Rayleigh performed the first analysis of a fixed geometry, infinitely long step bearing [54] and determined an optimum step configuration that produces the largest load. Since 1918, researchers such as Archibald and Hamrock [58] as well as Maday [59, 60] and others furthered the analysis of the gas lubricated Rayleigh step bearing. Hydrodynamic gas foil thrust bearings typically utilize a uniform circumferential taper to develop the lubricant wedge that generates a hydrodynamic pressure. Recently, Lee and Kim first analyze a bump-type Rayleigh-step thrust foil bearing [41].

Figure 3 displays two thrust foil bearing configurations, one in which a bump foil underspring structure supports a circumferentially tapered foil, and the other where a metal mesh structure supports a Rayleigh-step top foil.

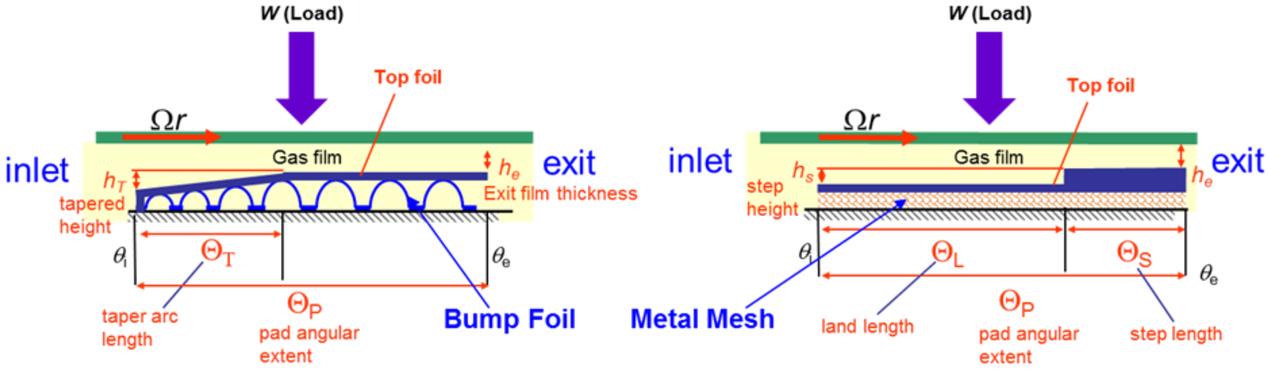

Figure 3. Schematic views of (a) a tapered bump-type and (b) a Rayleigh-step metal mesh thrust foil bearing.

---

[1] The majority of this section is reproduced with permission from Cable, T.A., and San Andrés, L., 2018, "On the Design, Manufacture and Premature Failure of a Metal Mesh Thrust Bearing: How Concepts that Work on Paper, Actually Do Not," ASME J. Eng. Gas Turbines Power, 140 (12), pp. 1-13. Copyright 2018 ASME.

Figure 4 displays views of a prototype Rayleigh-step thrust foil bearing consisting of three individual components, a solid metal bearing support, a thin circular metal mesh layer (or layers) and a thin metal Rayleigh-step top foil.

Table 1 lists the geometry of each component (backing, mesh subsutructure and top foil). The bearing support is 316 stainless steel with a thickness of 9.53 mm. The support contains six small threaded holes (3-48 UNF) to fix both the circular mesh layers and Rayleigh-step top foil; in addition, the support has six milled slots to provide cooling flow to the bearing pads. The copper metal mesh layers have outer diameters equal to that of the support, and inner diameters equal to that of the top foil. The 316 stainless steel Rayleigh-step top foil consists of six sector shaped pads, each with circumferential extent of Θ_P = 45°, and with inner and outer diameters of 50.8 mm and 101.6 mm, respectively. Each pad has a step etched into the metal to a depth of ~19 μm. The top foil thus has a piecewise thickness $t_{tf} = 0.108$ mm for $0 \leq \theta < \Theta_L$ and $t_{tf} = 0.127$ mm for $\Theta_L \leq \theta \leq \Theta_P$ (as indicated in Figure 3 (b)).

Table 1. Dimensions of a prototype Rayleigh step thrust foil bearing with a metal mesh substructure.

	Bearing Support	**Mesh Substructure**
Material	316 Stainless Steel	Copper
Inner Diameter	45.72 [mm]	50.8 [mm]
Outer Diameter	120.65 [mm]	120.65 [mm]
Thickness	9.53 [mm]	~0.40 [mm]

Table 1 Continued. Dimensions of a prototype Rayleigh step thrust foil bearing with a metal mesh substructure.

	Rayleigh-Step Top Foil
Material	316 Stainless Steel
Top Foil Thickness, t_{tf}	0.127 mm
Step Depth, h_S	19.1 μm
Coating	Parylene N
Coating Thickness	3 μm
Number of Pads, N_{PAD}	6 [-]
Outer Pad Diameter, D_{PO}	101.6 mm
Inner Pad Diameter, D_{PI}	50.8 mm
Pad Arc Extent, Θ_P	45°

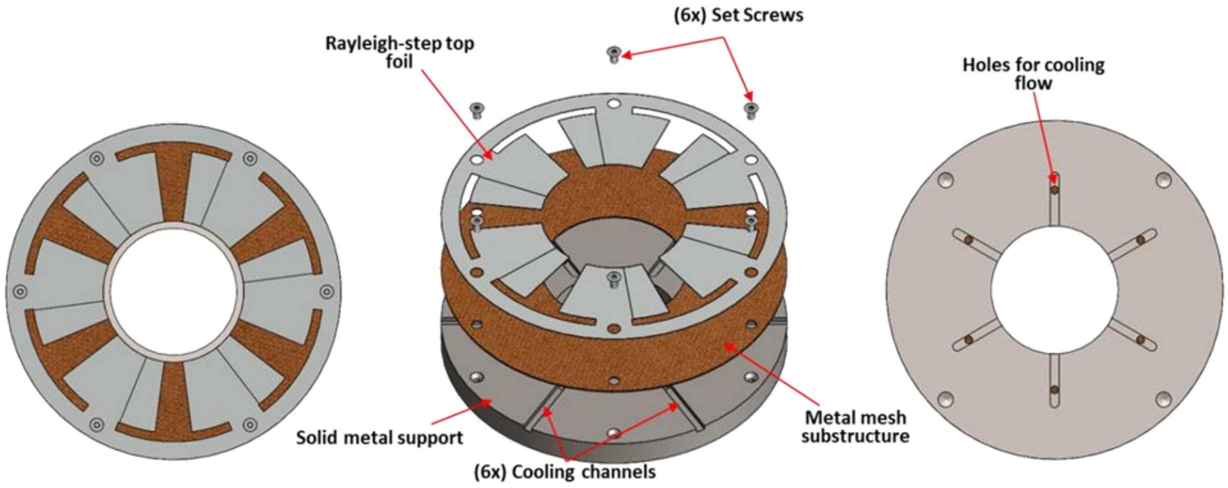

(a) Front View (b) Exploded View (c) Back View

Figure 4. (a) Assembled front view (b) an exploded view and (c) assembled back view of a Rayleigh-step metal mesh thrust foil bearing.

3.2 MANUFACTURING METAL MESH LAYERS

Figure 5 displays a dimensional drawing (dimensions in inches) of a single metal mesh layer. The mesh manufacturer, TWP Inc., uses a laser cutting process to separate each circular mesh layer from a sheet of uniform metal mesh. The six small holes on the 110.5 mm (4.35 in.) bolt circle as well as the 50.8 mm center hole are also laser cut, such that the diameters are nearly exact, and each of the mesh layers is nearly identical. Also of note, the copper mesh manufacturer produces metal mesh of uniform dimensions and with consistent weight per square foot, which is essential for uniformity.

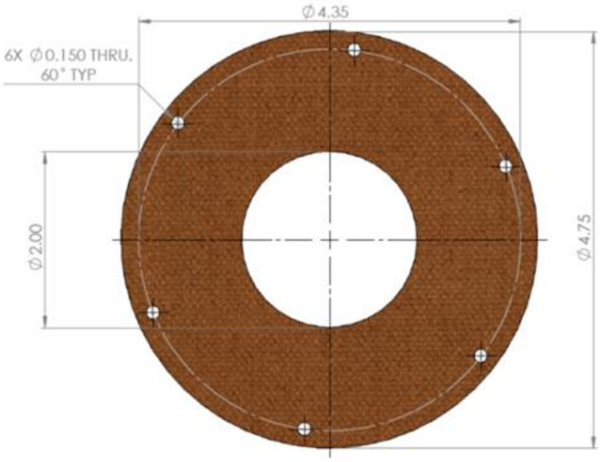

Figure 5. Dimensional drawing of a single circular metal mesh layer for a metal mesh thrust foil bearing (dimensions in inches).

Figure 6 displays a photograph showing three distinct mesh substructures. The metal meshes have different wire diameters (w_d) and are classified by the manufacturer in "openings per inch" (OPI). From the left to the right, in Figure 6, the meshes are 20, 30 and 40 OPI, respectively. Unlike a radial metal mesh bearing, the layers for a MMTFB sit on top of one another and are not compressed into a single solid. However, a mass ratio can be construed for a MMTFB, considering the ratio of the mass of a single mesh layer to that of the layer if it was solid copper. A mass ratio follows as

$$MR = \frac{m_{MM}}{A_{MM}\, w_d\, \rho_c} \tag{1}$$

where m_{MM} is the measured mass of a mesh layer, A_{MM} is its area, w_d is the wire diameter (or height) and ρ_c is density of copper.

(a) 20 OPI (b) 30 OPI (c) 40 OPI

Figure 6. Photographs of several mesh substructures with various wire diameters and densities. (OPI: opening per inch)

Table 2 summarizes the mesh parameters for each mesh type. The mass ratio MR = 0.44, 0.51 and 0.59 for the 20, 30 and 40 OPI meshes, respectively. Note that more OPI results in a finer mesh and a higher mass ratio. Metal mesh journal bearings typically utilize mesh structures with mass (or compactness) ratios greater than 0.25. For the current experiments, TWP provided ten sheets of each configuration, for a total of 30 mesh sheets. Each mesh is weighed on a precise digital scale (±0.01 g) prior to use.

Table 2. Parameters for metal mesh substructures. Density of Copper, ρ_c = 8,960 kg/m^3. (OPI: opening per inch)

	20 OPI	**30 OPI**	**40 OPI**
Wire Diameter, w_d [mm]	0.406	0.305	0.254
Square Opening Size, o_w [mm]	0.864	0.533	0.381
Measured Mass per Circular Sheet, m_{MM} [g]	15.00 (±0.10)	13.00 (±0.10)	12.55 (±0.10)
Circular Sheet Area, A_{MM} [cm^2]	93.4	93.4	93.4
Mass Ratio, MR [-]	0.44	0.51	0.59

3.3 MANUFACTURING A RAYLEIGH-STEP TOP FOIL

As mentioned earlier, the Rayleigh-step top foil is 316 stainless steel and has six arcuate pads, each containing a small Rayleigh-step. For rigid geometry step bearings, the steps are typically machined into the bearing surface via traditional means, such as milling. Manufacturing multiple small (less than 25.4 μm) steps into a thin (~0.127 mm thick) metal sheet requires of a non-conventional method. Photochemical milling (or etching) exposes metal to UV light through engineered phototools with predesigned images. Areas on the sheet with no laminate are eroded when exposed to the UV light, forming the intended shapes of the foil. A second photoetch develops the steps in each of the foils by exposing the intended areas to UV light over a shorter duration, eroding only some of the metal. This process produces extremely uniform steps on all of the foils.

Figure 7 displays three Rayleigh-step top foils, each with pad inner and outer diameters of 50.8 mm and 101.6 mm, respectively. The foils are each 0.127 mm thick and have a thin (5.08 mm) circular band connecting the six pads at the foil outer diameter. Six small fixture holes, located on a 110.5 mm (4.35 in.) bolt circle, provide locations to fix the top foil to the mesh substructure and the solid metal backing.

Figure 7 (a) shows a top foil where a 19 µm step occurs 15° from the pad leading edge, and Figure 7 (b) shows a pad where the step occurs 22.5° from the leading edge. The schematic in Figure 7 (c) depicts a new concept, a “negative slant” Rayleigh step configuration, where the step starts at the outer diameter of the pad at the leading edge and finishes at the inner diameter at the pad trailing edge. The orientation of the negative slant intendeds to oppose the centrifugal pumping effect that typically forces lubricating fluid out of the hydrodynamic loading zone. For the experiments herein, three prototypes are manufactured for each configuration, for a total of nine test top foils.

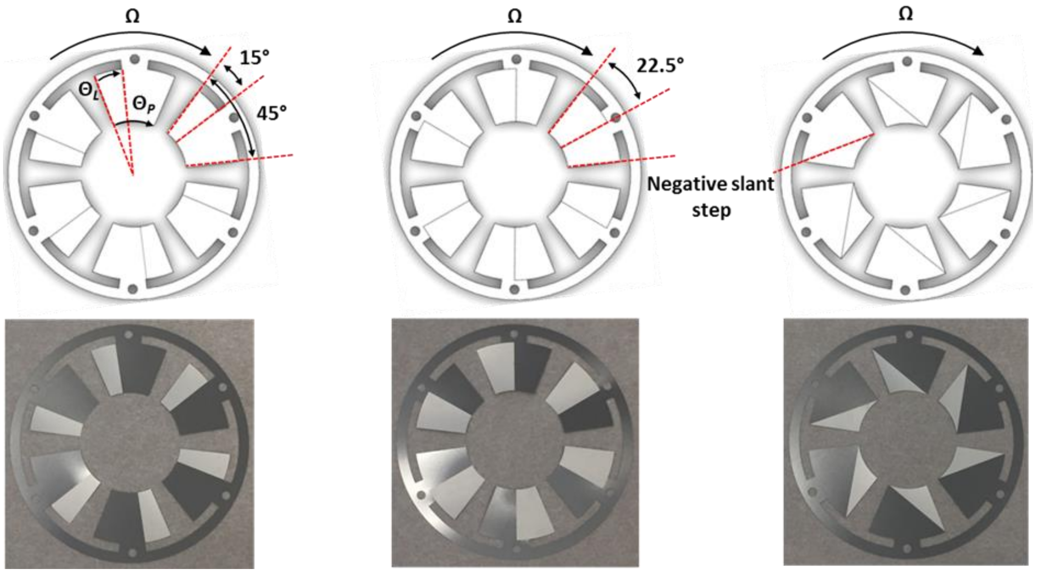

(a) $\Theta_L / \Theta_P = 1/3$ (b) $\Theta_L / \Theta_P = 1/2$ (c) $0 \leq \Theta_L \leq 45°$

Figure 7. Schematics and photographs of three manufactured six-pad Rayleigh-step top foils.

During startup and shutdown, foil bearings experience solid contact between the rotor and top foil, and thus need enduring coatings to reduce wear [17]. The Rayleigh-step top foil necessitates a coating that is robust, yet thin enough as to not interfere with the step height (19 μm). Traditional foil bearings implement MoS_2, PTFE or a NASA designed PS304® coating to reduce the coefficient of friction between the top foil and the collar [9,12]. As MoS_2 and PTFE require coating thicknesses of at least 25.4 μm, and the NASA PS304® coating requires a run-in process at a high (~300° C) temperature, the Rayleigh-step top foil requires a different coating. To reduce the coefficient of friction between the foils and the thrust collar, the thrust collar has a 25.4 μm thick layer of thin dense chrome and the top foils have a thin (~3 μm) Parylene N® coating (Table 3 lists some properties for the coating).

The Parylene coating, manufactured by Paracoat Technologies, is deposited via a vapor deposition process, yielding a coating which is uniform, conformal, flexible and robust. The uses of Parylene range from o-rings to medical implants to electrical components. Note that the three top foils in Figure 5 are not coated, while the other two sets of foils have the Parylene coating.

Table 3. Physical and thermal properties of Parylene N®, manufactured by Paracoat Technologies.

	Magnitude
Yield Strength	2.4 GPa
Density	1.11 g/cm^3
Static Coefficient of Friction	0.25
Dynamic Coefficient of Friction	0.25
Melting Temperature	410 °C
Thermal Conductivity	0.12 W/m.K

3.4 A TEST RIG FOR THE EVALUATION OF HYDRODYNAMIC FOIL THRUST BEARINGS

Gas thrust bearing test rigs [10, 15, 18] typically measure bearing load capacity, drag torque, bearing temperature rise and axial force coefficients. Most test rigs share a similar design, consisting of a floating load shaft and a thrust collar which is spun by either an electric motor or an impulse turbine. An aerostatic bearing (or bearings) typically levitates the load shaft, on which the test bearing resides, allowing the bearing to rotate and translate axially without friction.

Figure 8 displays a photograph and a cross-section view of a test rig for characterizing the static and dynamic forced performance of gas hydrodynamic thrust foil bearings. The test rig consists of four main components, a solid steel thrust collar spun by a 2.2 kW router motor (40 krpm max), a thrust load shaft, an aerostatic loading plenum, and a test bearing. As depicted in Figure 8, the aerostatic plenum contains two porous carbon bushings which float the load shaft, on which the test bearing fixes via threaded connections. The following sections detail each of the test rig components as well as instrumentation and operating capabilities.

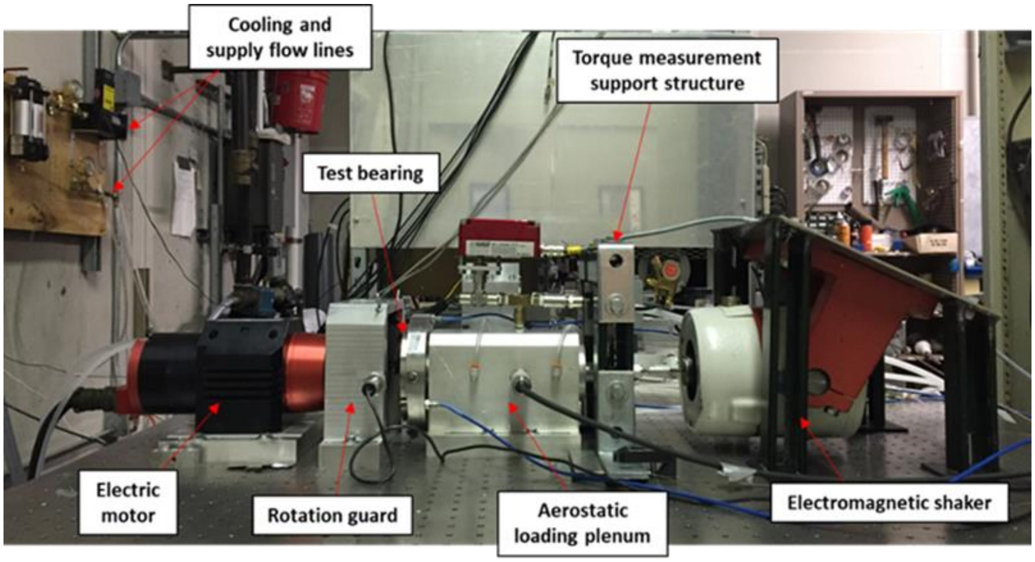

(a) Isometric View

Figure 8. Isometric and cross-section views of a test rig for the evaluation of hydrodynamic foil thrust bearings.

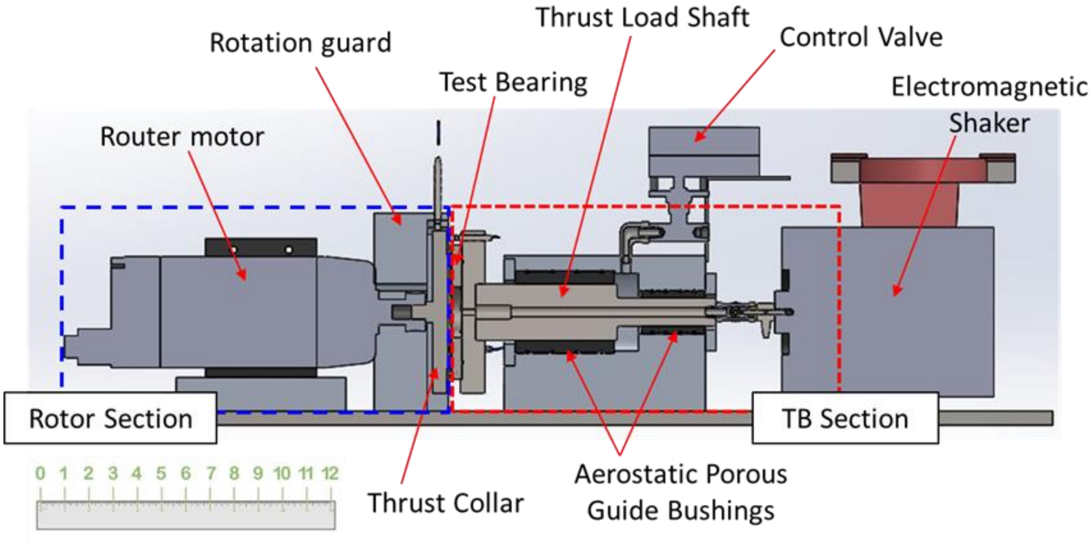

(b) Cross-section view

Figure 8 Continued. Isometric and cross-section views of a test rig for the evaluation of hydrodynamic foil thrust bearings.

The section on the left side of the schematic in Figure 8 (b), labeled “Rotor Section”, consists of a metal disk (collar) fixed in a router motor via a collet and precision nut. Figure 9 displays dimensional drawings of the 4140 steel thrust collar, having an outer diameter of 146mm (5.75 in.). The front face of the thrust collar has a stepped area with a diameter of 102.1mm (4.02 in.) and a 25.4 μm layer of thin dense chrome. A test bearing mates against this stepped area to develop hydrodynamic pressure. The recessed ridge, from 102.1 mm to 146 mm, provides a location for three non-contacting displacement sensors to measure the relative displacement between the thrust collar and a test bearing. As machined, the measurement surface has ~25 μm of mechanical runout, while the stepped ridge has less than 15 μm. The collar is precision balanced and has a residual imbalance of 0.014 g-cm.

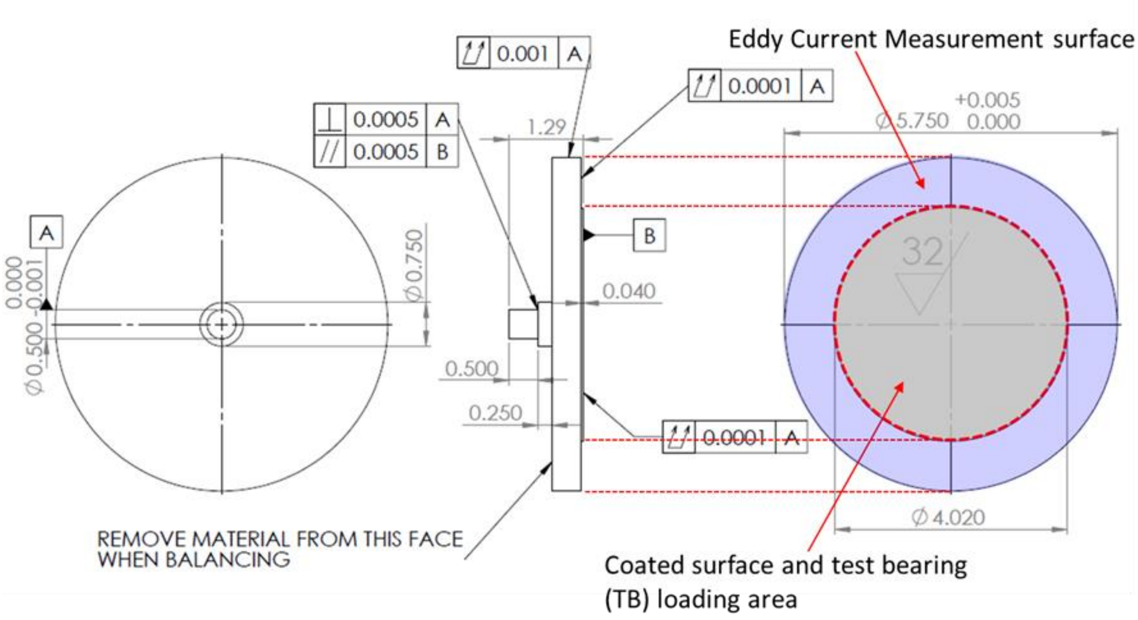

(a) Back View (b) Side View (c) Front View

Figure 9. Dimensional drawings of 4140 steel thrust collar for a thrust bearing test rig (dimensions in inches).

The right portion of the test rig, labeled TB Section in Figure 8, consists of an aerostatic plenum with two porous guide bushings, a load shaft and a test bearing. Figure 10 displays both isometric and exploded views of the load shaft and attached test bearing, indicating the individual components. The cylindrical bushing shaft is 21.6 cm long and has diameters slightly smaller than the porous carbon guide bushings (25.4 and 50.8 mm, respectively). Although not pictured in Figure 10, a small diameter thru hole locates at the center of the load shaft, allowing cooling flow to the test bearing. The step at the center of the bushing shaft provides an area (A_{SL} ~ 14.7 cm^2) for the chamber pressure (described in more detail below) to create a static load, pushing the test bearing into the thrust collar.

A circular 316 stainless steel loading flange bolts onto the bushing shaft and holds the test bearing as well as three eddy current sensors. At the back end of the bushing shaft, an 1/8th" NPT connection allows for the application of cooling flow as well as providing attachments for a dynamic load cell and a torque arm for determining the bearing drag torque. Finally, an o-ring, placed between the test bearing and loading flange, ensures that the entirety of the supplied cooling flow reaches the test bearing.

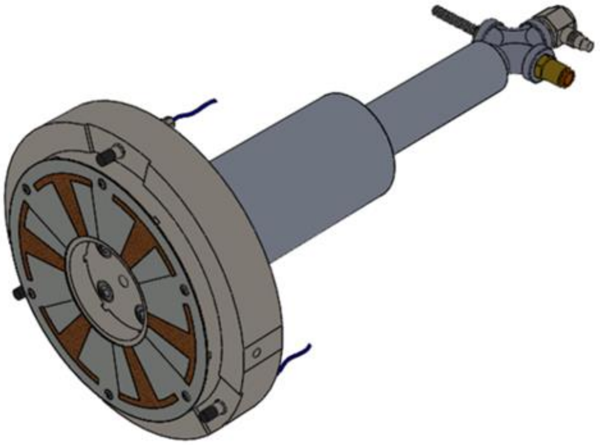

(a) Isometric view

Figure 10. Schematic views of load shaft for thrust bearing test rig.

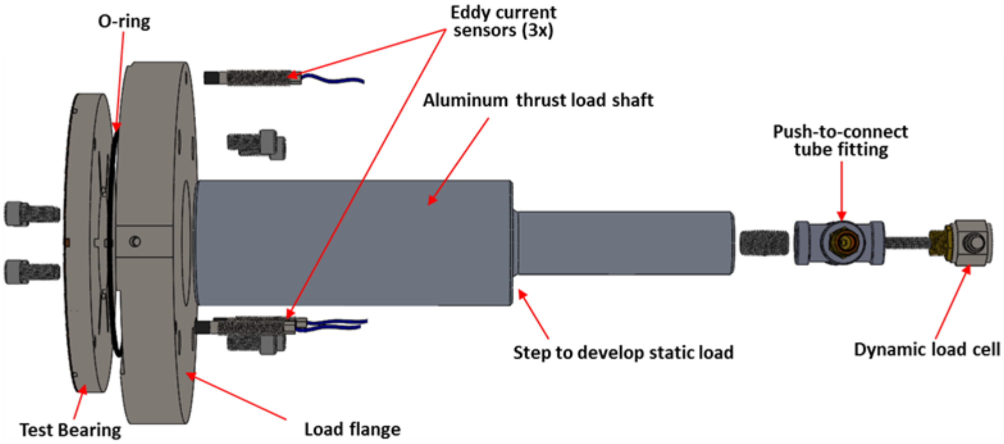

(b) Exploded view of a thrust load shaft with individual components labeled

Figure 10 Continued. Schematic views of load shaft for thrust bearing test rig.

Figure 11 displays an isometric view and an exploded view of the aerostatic plenum, indicating the individual components. Pressurized air, up to 7.9 bara (115 psia), supplies two hydrostatic porous graphite bushings through two push-to-connect fittings threaded into the plenum body. Some of the flow through the bushings escapes to ambient, while some travels to the central cavity, increasing its static pressure. The porous graphite bushings float the shaft on a small (~ 4 μm) air film and also act as seals for the central cavity due to their extremely tight radial clearance. A high precision (+/- 0.08%) static pressure transducer measures the pressure in the central chamber, while a precise motor actuated control valve (CV = 0.03) sets the pressure in the center chamber to achieve a desired static load on the test bearing. The resulting static load on the test bearing is approximately $F \approx \Delta P A_{SL}$, where A_{SL} = 14.7 cm^2. A cross-section view of the plenum and load shaft, shown in the next figure, helps to illustrate this concept.

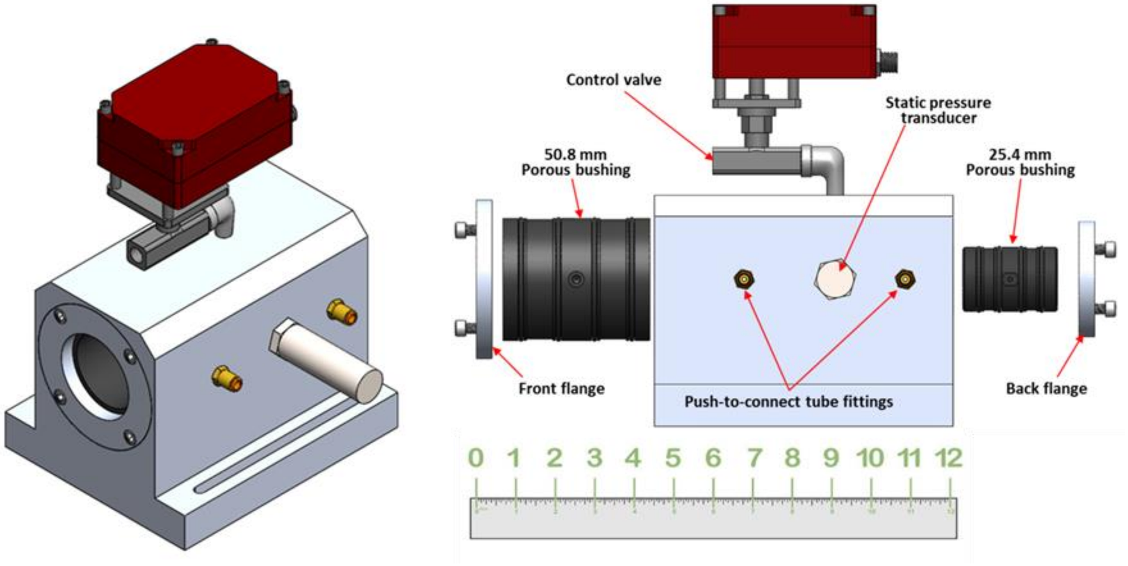

(a) Isometric view (b) Exploded view with individual components labeled

Figure 11. Schematic views of an aerostatic load plenum for test rig.

In addition to the supply flow to the bushings, a thru hole along the shafts center allows for compressed air to cool a test bearing. A precision needle valve (CV = 0.47) controls the cooling flow to the bearing while a mass flow meter measures the flow (max of 500 SLPM). Figure 12 shows the piping for the supply flow and cooling flow as well as a schematic cross-section view of the TB load shaft assembled in the aerostatic plenum, indicating the directions of the supply and cooling flows as well as the resulting static load from the pressure in the center chamber.

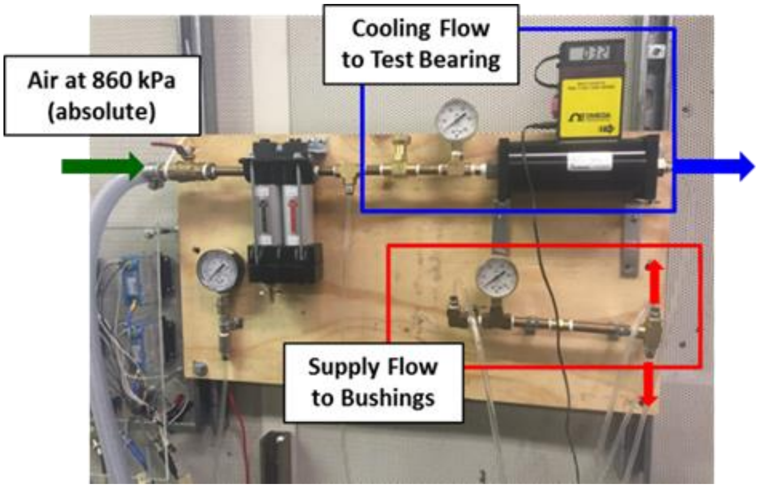

(a) Flow loop for supply and cooling flow

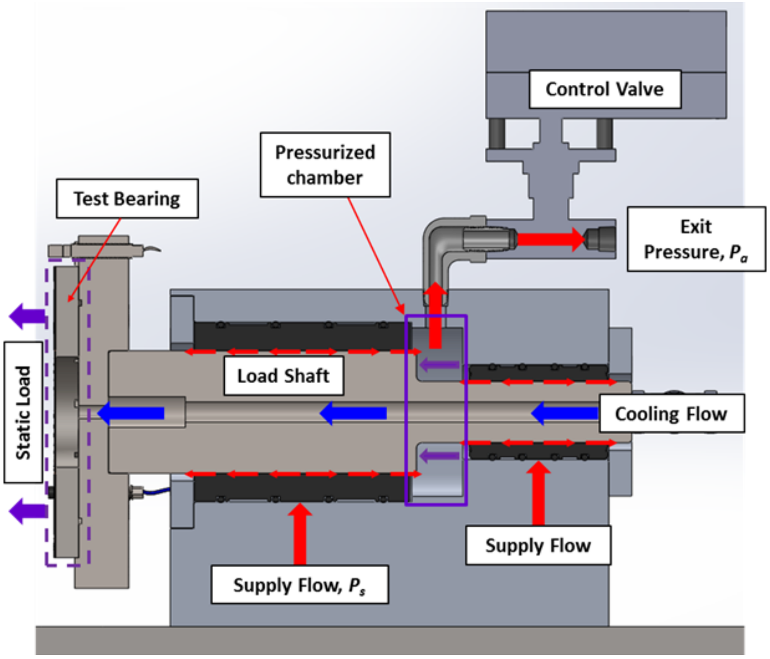

(b) Cross-section of aerostatic plenum with load shaft installed

Figure 12. (a) Photograph of air flow piping and (b) a cross-section view of aerostatic plenum and TB load shaft.

3.5 INSTRUMENTATION AND OPERATING CAPABILITIES OF A FOIL BEARING TEST RIG

Table 4 lists the instrumentation on the test rig as well as the quantities they measure and their associated uncertainties. In total, the rig has 5 eddy current sensors, 4 thermocouples, a static pressure transducer, a static load cell, an infrared tachometer, dynamic load cell, and an accelerometer. All of the data is recorded using commercial data acquisition (DAQ) software and in-house LabVIEW® programs.

Table 4. Instrumentation on thrust bearing test rig.

	Quantity	**Measurement**	**Precision**
Eddy Current Sensor	3	Test bearing relative axial displacement	± 0. 3% of probe distance
Thermocouple	4	Test bearing and motor temperatures	±2.2 °C or 0.75% of measurement
Mass Flow Meter	1	Cooling flow rate	± 5 SLPM
Static Pressure Transducer	1	Chamber pressure	± 0. 08 psi
Static Load Cell	1	Bearing drag torque	0.26 N
Dynamic Load Cell	1	Test bearing dynamic load	± 1 N
Accelerometer	1	Test bearing absolute acceleration	$\leq 0.5\ m^2/s$
Infrared Tachometer	1	Thrust collar rotational speed	±10 rpm
Valve Controller	1	Valve position	2°

Table 5 lists the capabilities for the thrust foil bearing test rig. The router has two sets of angular contact ball bearings, with a total static axial load capacity of 1.4 kN. The motor-torque curve from the manufacturer indicates that the 2.2 kW motor can deliver torque up to 1.1 N.m. In short, the rig can apply static loads up to 580 N (W/A ~ 127 kPa (18.4 psi) for the current bearing), and dynamic loads up to 100 N via an electromagnetic shaker whilst spinning the thrust collar to a max speed of 40 krpm ($R\Omega$ = 212 m/s). The thru hole in the TB load shaft facilitates cooling flow to the test bearing with a range from 0 – 200 SLPM. The load flange on the load shaft can accept foil thrust bearings with outer diameters (ODs) equal to 101.6 mm. At the bearing outer diameter, the surface speed of the thrust collar is ~212 m/s.

With a test thrust bearing in place, the rig allows the measurement of bearing drag torque, pad temperatures, static load versus deflection behavior, dynamic axial force coefficients and load capacity. All of these measurements can also be performed with increasing amounts of cooling flow.

In addition to the instrumentation on the rig, a National Instruments DAQ hardware consists of a CDAQ-9174 chassis and four analog output/input modules: 9205 (±10 V analog input module), 9263 (±10 V analog output module), 9234 (±5 V sound and vibration input module), and 9211 (±80 mV temperature input module).

Table 5. Rig capabilities.

Operating Speed, $R_{PO}\Omega$	0 – 40 krpm (212 m/s)
Motor Torque Capability	1.1 N.m
Bearing OD Limit	101.6 mm
Static Load	0 - 580 N
Dynamic Load	0 – 100 N
Cooling Flow	0 – 300 SLPM

4. EXPERIMENTS WITH A RAYELIGH-STEP METAL MESH THRUST FOIL BEARING[2]

4.1 TESTS WITH NO ROTOR SPEED

Figure 13 depicts a MMFTB installed on the test rig from Figure 8. Three eddy current sensors locate on the outer diameter of a loading flange (labeled in Figure 13) on which the test thrust bearing mounts. The three sensors, located on a diameter of ~143 mm and spaced 120° apart, record the relative displacements between the test bearing and the thrust collar. Before conducting the load versus deflection tests, the test bearing mounts to the load shaft, but has no foil or mesh layers in place (solid metal bearing support only). A static load (up to 300 N) pushes the thrust bearing support into the thrust collar, while the DAQ records the relative displacements of the three eddy current sensors. Alignment between the two surfaces is adjusted by shimming the plenum and repositioning it until the relative displacements between the sensors and the collar are within 5 μm of each other at the maximum applied load.

---

[2] The majority of this section is reproduced with permission from Cable, T.A., and San Andrés, L., 2018, “On the Design, Manufacture and Premature Failure of a Metal Mesh Thrust Bearing: How Concepts that Work on Paper, Actually Do Not,” ASME J. Eng. Gas Turbines Power, 140 (12), pp. 1-13. Copyright 2018 ASME.

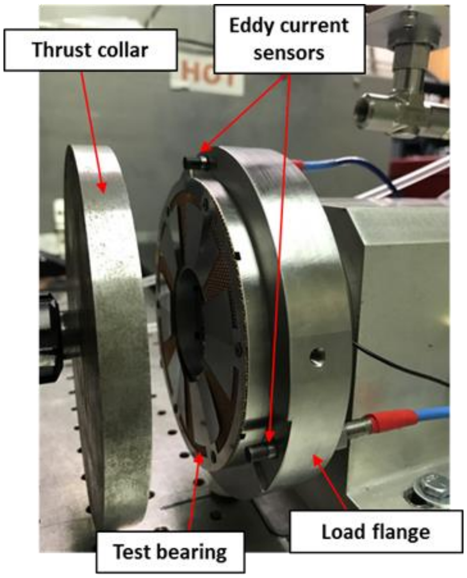

Figure 13. Photograph of a metal mesh thrust bearing installed on test rig.

The goal of the current research is to compare the performance of the MMFTB to that of a similar size BFTB in the literature [19]. To compare the performance between two foil bearings, it is desirable for the MMFTB to have a structural stiffness (stiffness of the metal mesh underspring structure) similar to that of the BFTB. The number of mesh layers for the assembled bearing depends on the application. Conventional wisdom indicates that a MMFTB with more layers has a smaller structural stiffness than a MMFTB with fewer layers (the layers act as springs in series). In addition, the MMFTB with more layers should have a larger material damping (more wire connections allow for more energy dissipation through sliding friction).

Figure 14 displays static specific load (*W/A*) versus bearing deflection for the MMFTB having 1, 2 or 3 layers and with mesh sizes of 20, 30 and 40 OPI. The deflections displayed in Figure 14 are the average displacement of the three eddy current sensors, thus representing the axial translations of the bearing center. In addition, each of the curves is an average of three load cycles.

Note that the bearings are preloaded with 30 N *(W/A*~10 kPa) before the tests begin to avoid an area where a small force causes a large displacement. Figure 14 displays only the load cycles, and not the unload data, due to the uncharacterized pressure hysteresis from the air pressurized plenum.

Figure 14 (a) shows that the MMFTBs with a single sheet are very stiff, with deflections less than, or equal to 25 μm for loads up to 70 kPa. Increasing the number of mesh layers softens the bearing, thus producing a larger deflection amplitude. In general, using sheets with a finer mesh (higher mass ratio, *MR*) creates a stiffer bearing. Essentially, a looser mesh weave and a larger wire size allow for more movement of the individual wire.

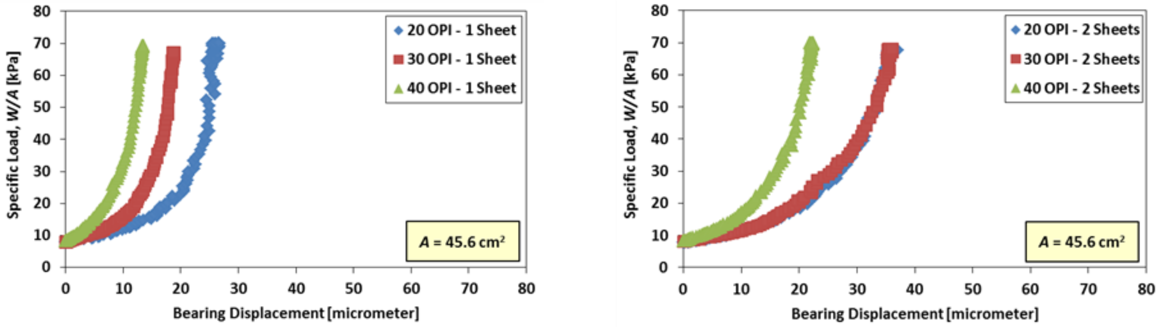

(a) Bearing with 1 metal mesh sheet (b) Bearing with 2 metal mesh sheets

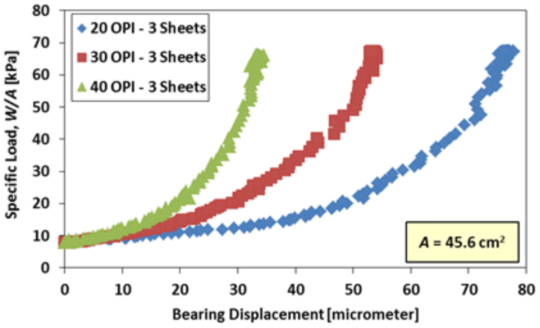

(c) Bearing with 3 metal mesh sheets

Figure 14. Specific load (*W*/*A*) versus bearing displacement for bearings assembled with up to three metal mesh sheets and with increasing mesh density (OPI varies).

The illustration in Figure 15 lends physical insight into this hardening nonlinearity, for a single sheet of interwoven mesh wires. In its undeformed state, the mesh layer is not entirely flat, but the wires intertwine in a sinusoidal-like pattern, one over another. When a static load applies to the structure, the mesh wires elongate, losing their curvature and forming a flat layer of mesh. Intuitively, this suggests that mesh layers with larger wires and a lesser OPI (i.e. more room to expand) should be more flexible, as confirmed by the results in Figure 14.

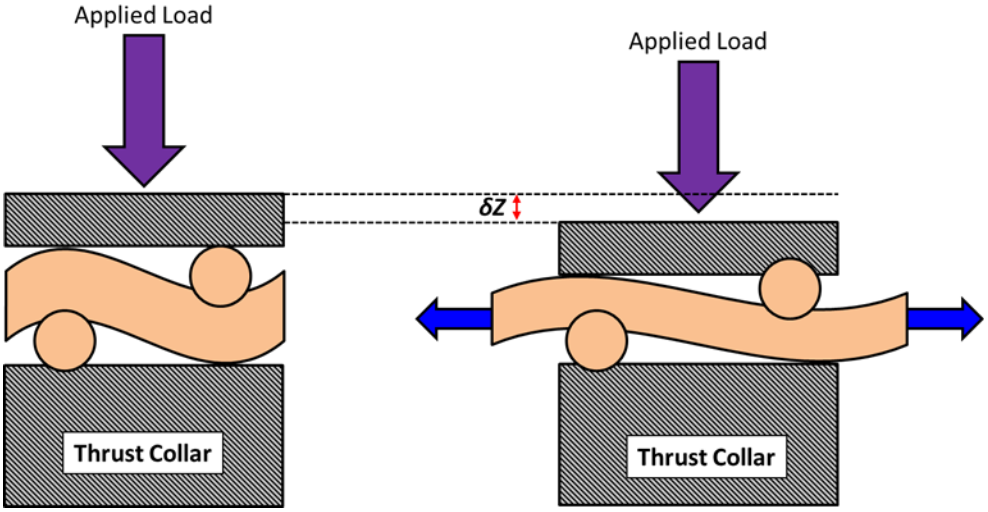

(a) Un-deformed mesh layer (b) Deformed metal mesh layer

Figure 15. Schematic representation of the elastic compression process for a single mesh layer with a sinusoidal weave.

Figure 16 displays the static specific load (*W/A*) versus bearing deflection for a MMFTB having either 2 or 3 layers and with mesh size of 20, 30 and 40 OPI. The graph also shows results for a similarly sized BFTB from Stahl [19]. The MMFTB deflections displayed in Figure 14 are the average displacement of the three eddy current sensors, thus representing the axial translation of the bearing center. In addition, each of the curves is an average of three load cycles, with error bars indicating the standard deviation amongst the three cycles. It is important to note that the MMFTBs are preloaded with 35 N *(W/A* ~7.5 kPa) before the tests begin to avoid an area where a small force causes a large displacement. For reference, this preload establishes a null displacement

(z = 0). The measurements of Stahl [19] also include a slight preload (W/A ~ 3 kPa) due to the weight of the bearing, the bearing holder and the loading block.

The test data in Figure 16 shows that the three MMFTBs have similar load/deflection behavior to that of the BFTB, all showing a typical hardening nonlinearity common to foil bearings. A mesh layer in its undeformed state is not entirely flat but has some inherent waviness. When a static load applies to the structure, the mesh flattens. Combining multiple mesh layers together exacerbates the initial bulging.

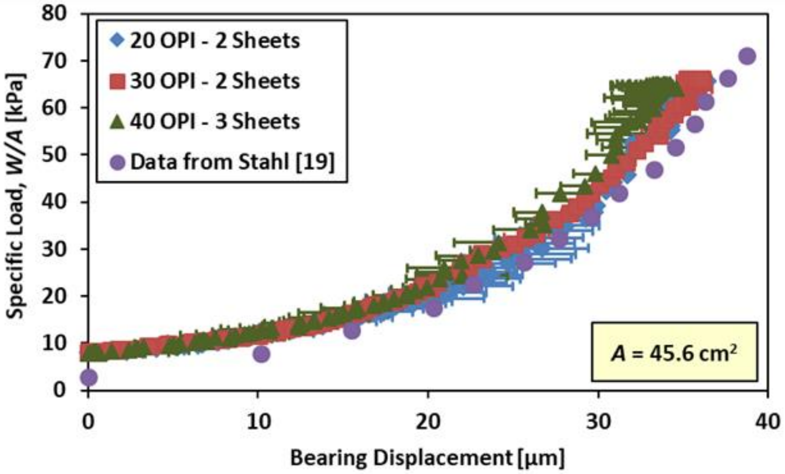

Figure 16. Specific load versus bearing displacement for three MMFTBs (# sheets and OPI vary) and a BFTB from Ref. [19].

An odd order polynomial models the pad reaction force $W(z)$ as a function of the mesh deflection (z). Presently,

$$W(z) = W_0 + K_1 z + K_3 z^3 \tag{2}$$

is quite adequate to fit the test data with a good correlation coefficient (R^2>=0.99). Table 6 lists the coefficients for the polynomials.

Table 6. Coefficients of polynomials fitting recorded deflection and load data.

	Load W (N) vs displacement z (μm)			
	$W\left(x\right)=W_0+K_1z+K_3z^3$			
Bearing	W_0 [N]	K_1 [N/μm]	K_3 [N/μm^3]	R^2
20 OPI – 2 Sheets	35	0.529	5.14E9	0.99
30 OPI – 2 Sheets		0.633	5.07E9	0.99
40 OPI – 3 Sheets		1.047	5.70E9	0.99
Stahl [19]	13	1.683	4.14E9	0.99

The bearing structural stiffness K_s is derived from

$$K_s=\frac{dW}{dz}=K_1+3K_3z^2 \tag{3}$$

and its uncertainty propagates from the precision uncertainty (repeatability error) in the mesh deflection z.

Figure 17 displays the stiffness (K_s) versus deflection for the four bearings in Figure 14. All the bearings start with a relatively constant stiffness (K_s < 2 MN/m), that then increases rapidly after z ~ 10 μm approaching 20 MN/m. Note that the MMFTBs are softer than the BFTB over the 0-10 μm range, and then exceed the structural stiffness of the BFTB above z ~ 20 μm.

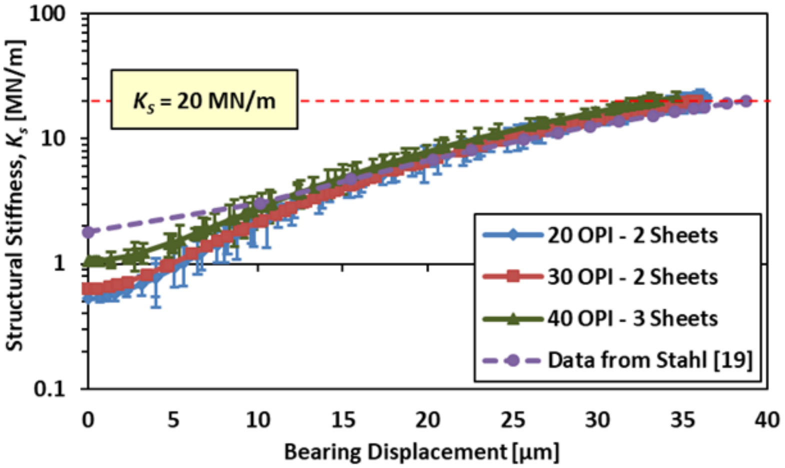

Figure 17. Estimated structural stiffness (K_s) versus bearing deflection for several MMFTBs and a BFTB from Ref. [19].

During operation with a foil bearing, the structural stiffness and material damping of the underspring (metal mesh or bump foils) act in series with the stiffness and damping of the air film. Hence, characterization of the dynamic performance of the underspring structure is necessary.

Balducchi *et al.* [11] perform experiments to determine the stiffness and equivalent viscous damping for a BFTB with dimensions identical to those of the current MMTFB. Thus, Ref. [11] provides data against which to benchmark the current MMFTB structure dynamic performance (*K*, *C*).

Figure 18 displays a photograph of the test rig set up for dynamic load measurements. An electromagnetic shaker connects to the back of the static load shaft and imposes a dynamic load on the test bearing. The aerostatic guide bushings (3.8 μm radial gap) allow for friction free motion, and as such, contribute negligible stiffness and damping (in the axial direction) to the test system. A high precision (1 V/g) single axis accelerometer, mounted on the backside of the loading flange, records the absolute acceleration of the test bearing while the three eddy current sensors record the relative displacements between the test bearing and the thrust collar.

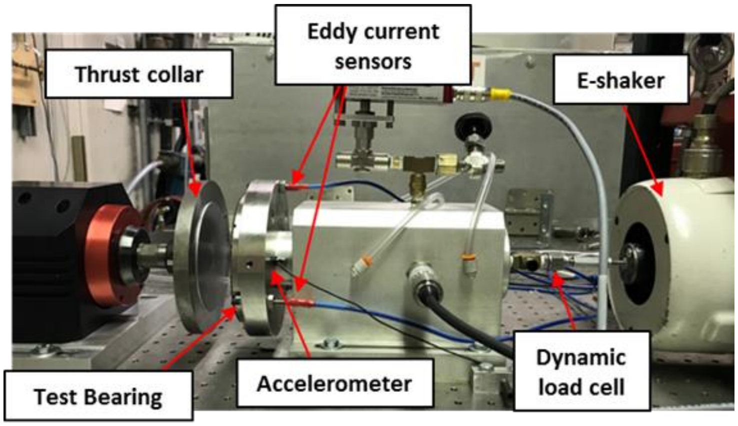

Figure 18. A photograph of the thrust foil bearing test rig set up for dynamic analysis.

Figure 19 displays a lumped parameter model of the test system undergoing axial motions (z). In the figure, m_1 = 4.22 kg (measured on a digital scale and confirmed with low a frequency excitation test) refers to the mass of the load shaft and test bearing assembly, while m_2 is the mass of the thrust collar and the router motor armature (unknown total mass). The aerostatic plenum applies a static load ($W_0 = \Delta P A_{SL}$) to the test bearing while the shaker imposes a periodic dynamic load ($\overline{F}$) to the back of the load shaft, where a dynamic load cell resides.

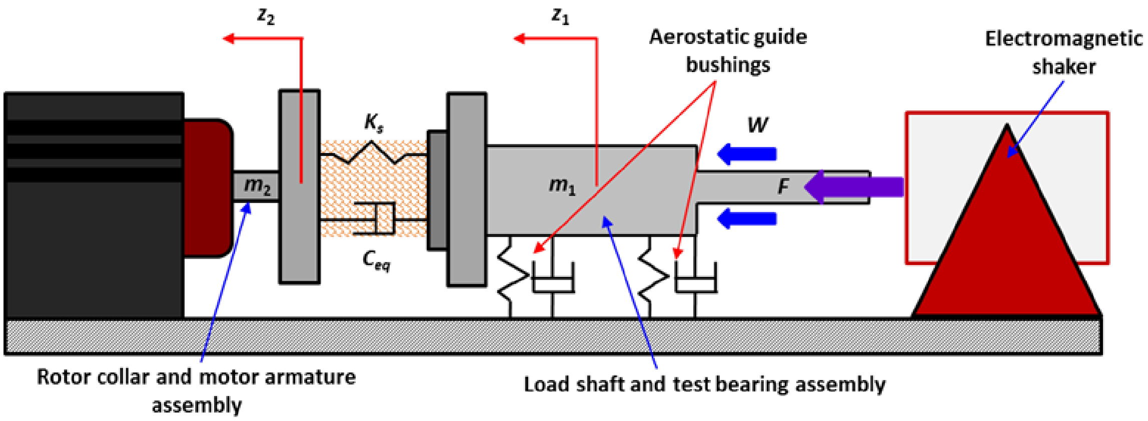

Figure 19. Axial dynamics model for test foil thrust bearing and load shaft.

The equation of motion (EOM) for the assembled load shaft-MMFTB and rotor collar in Figure 19 is

$$m_1 \ddot{z}_1 = F\left(t\right) - F_{MMFTB} \tag{4}$$

where $\ddot{z}_1$ is the (absolute) acceleration of the assembly (m_1).

Consider a periodic excitation force of amplitude $\bar{F}$ and applied to the end of the load shaft with frequency ω superimposed on an aerostatic load (W_0). The ensuing displacement has the same frequency, i.e.

$$F\left(t\right) = \bar{F}\,\mathrm{e}^{i\omega t} + W_0 \rightarrow z_{12}\left(t\right) = z_1\left(t\right) - z_2\left(t\right) = \bar{Z}_{12}\,\mathrm{e}^{i\omega t} \tag{5}$$

where $\bar{Z}_{12}$ is the (complex) magnitude of the (averaged) relative displacement between the collar and shaft.

The resulting EOM for the test bearing and load shaft assembly (m_1) in the frequency domain is

$$\left(\bar{F} - m_1 \bar{A}_1\right) = \bar{F}_{MMFTB} \tag{6}$$

where $\bar{A}_1$ is the absolute acceleration and $\bar{F}_{MMFTB}$ is the dynamic reaction force of the MMFTB structure. A complex dynamic stiffness (*H*) for the MMFTB is

$$H = \frac{\left(\bar{F} - m_1 \bar{A}_1\right)}{\bar{Z}_{12}} = \left(K_{MMFTB} + i\omega C_{eq}\right) \qquad (7)$$

whose real and imaginary parts make up the bearing dynamic stiffness and equivalent viscous damping, respectively.

As mentioned, the goal of the current analysis is to compare the performance of the MMTFB to that of a similar BFTB, thus, it is desirable to reproduce both the dynamic displacement amplitude (5 μm) and frequency range of excitations (150 Hz -750 Hz) for the same applied loads 30-150 N (in 30 N increments), as in Ref. [11]. However, the shaker can only deliver ~100 N dynamic loads. Due to the limited power from the shaker, the frequency range for the current tests limits to excitations with frequency ranging from 40 Hz to 300 Hz and with a dynamic displacement amplitude $\bar{Z}_{12} = 5\ \mu\text{m}$.

The following plots present dynamic stiffnesses for three MMFTBs (bearing with 3 sheets of 20, 30, or 40 OPI mesh) and for three applied static loads (*W/A* =7.7, 19.7, and 32.9 kPa). The shaker applies a single frequency periodic load to the test bearing, in 20 Hz increments, while the DAQ records the dynamic load, acceleration, and relative displacements between the eddy current sensors and the thrust collar. The sampling rate is 10,240 samples/s. Each data point in the following plots is an average of 5s of elapsed data (i.e. 51,200 samples). In addition, error bars for each of the following data sets represent the total bias (instrumentation) and precision (repeatability) uncertainty in the measurements, determined at a 95% confidence interval.

Figure 20 displays the real part of the MMFTB complex stiffness (*H*) for three applied static loads *W/A* = 7.7, 19.7 and 32.9 kPa. The average dynamic displacement amplitude is 5 μm. The results in Figure 20 show that the real part of H (Re(H) → K) is constant over the whole frequency range, maintaining a constant value for each tested load and mesh density (20, 30, or 40 OPI). K magnitude increases with an increase in applied static load and also with the mass ratio of the mesh. The imaginary part of H (not displayed) increases with both the applied load and mesh mass ratio, and also with the excitation frequency.

Note that while each data set does have associated error bars, as mentioned earlier, the total uncertainty is typically small enough to fall inside of the data marker.

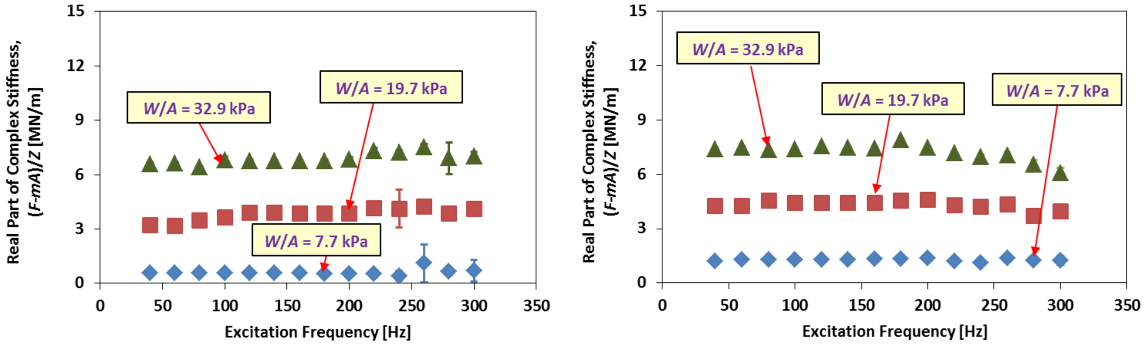

(a) 3 Sheets of 20 OPI Metal Mesh

(b) 3 Sheets of 30 OPI Metal Mesh

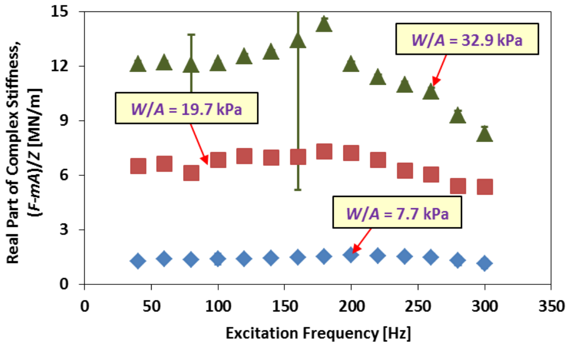

(c) 3 Sheets of 40 OPI Metal Mesh

Figure 20. MMFTB dynamic stiffness (*K*) versus excitation frequency. Applied specific load *W*/*A* = 7.7, 19.7 and 32.9 kPa and three distinct mesh types. $\bar{Z}_{12}$ = 5 μm

Damping in metal mesh structures is best quantified by a combination of viscous, hysteretic and dry-friction behaviors [49]. However, Alkhateeb [49] and Chirathadam and San Andrés [52] show that modeling energy dissipation in a mesh structure as purely material damping is adequate. For a system characterized by mainly hysteretic damping,

$$\omega C_{eq} = K\gamma \tag{8}$$

where γ is a material loss factor derived from the complex stiffness (*H)* as

$$\gamma = \frac{\mathrm{Im}\left\{H_{(\omega)}\right\}}{\mathrm{Re}\left\{H_{(\omega)}\right\}} \tag{9}$$

The propagation of uncertainty to the material loss factor is calculated via a standard Kline-Mcklintok approach [61]. Figure 21 displays the bearing material loss factor (γ) for three MMFTBs subjected to static load *W/A* = 7.7, 19.7 and 32.9 kPa. For the bearing with 20 and 30 OPI mesh sheets, γ~0.18 is largely unaffected by either the applied load or the excitation frequency, 40 Hz - 300 Hz. For the MMFTB with 40 OPI mesh sheets, the average γ decreases slightly with applied load (from γ = 0.35 for *W/A* = 7.7 kPa to γ = 0.21 for *W/A* = 32.9 kPa). Note that large uncertainties occur for low loads (*W/A* = 7.7 kPa) due to the very flexible metal mesh.

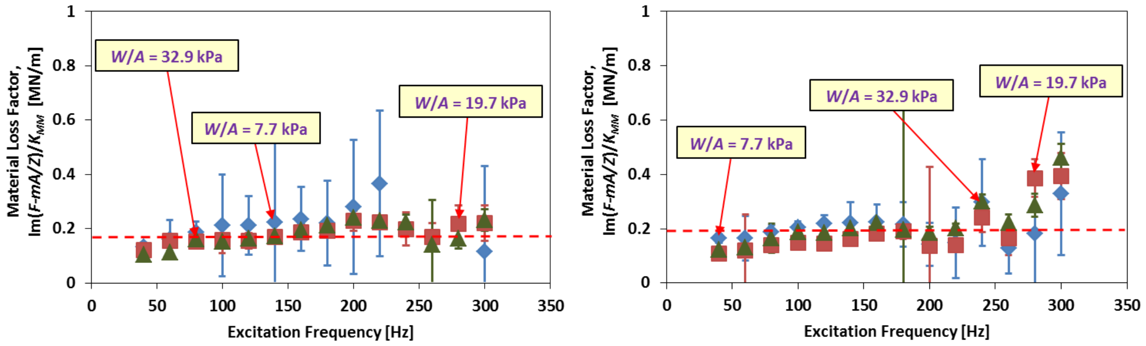

(a) 3 Sheets of 20 OPI Metal Mesh

(b) 3 Sheets of 30 OPI Metal Mesh

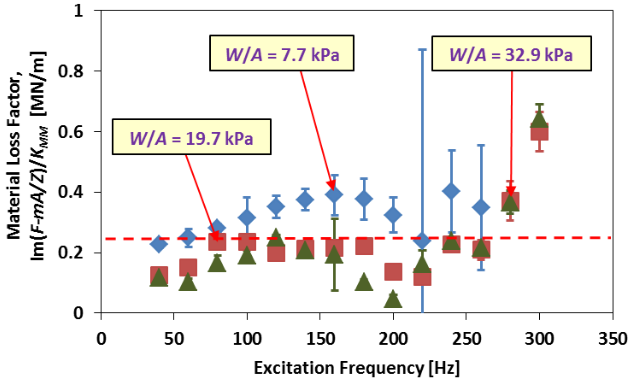

(c) 3 Sheets of 40 OPI Metal Mesh

Figure 21. MMFTB material loss factor (γ) versus excitation frequency for three applied specific loads of *W*/*A* = 7.7, 19.7 and 32.9 kPa and three different mesh types. $\bar{Z}_{12}$ = 5 μm.

Figure 22 summarizes the MMFTB stiffness and loss factor for the three distinct mesh types and versus an increasing specific load. Simple numeric averages (excluding data points with large uncertainty) of the data displayed in Figures 20 & 21 determine an average dynamic stiffness (*K*) and material loss factor (γ) for each applied load over the excitation frequency range 40 Hz - 300 Hz.

Figure 22 also includes data for an average loss factor and average stiffness coefficient for a BFTB for excitations ranging from 150 Hz -300 Hz [11]. The data reproduced from Ref. [11] in Figure 19 is a best representation, as the authors don't list average magnitudes for bearing stiffness or loss factor. The graphical representations in Figure 22 show that the MMFTB has a similar dynamic structural performance as that for the similarly sized BFTB.

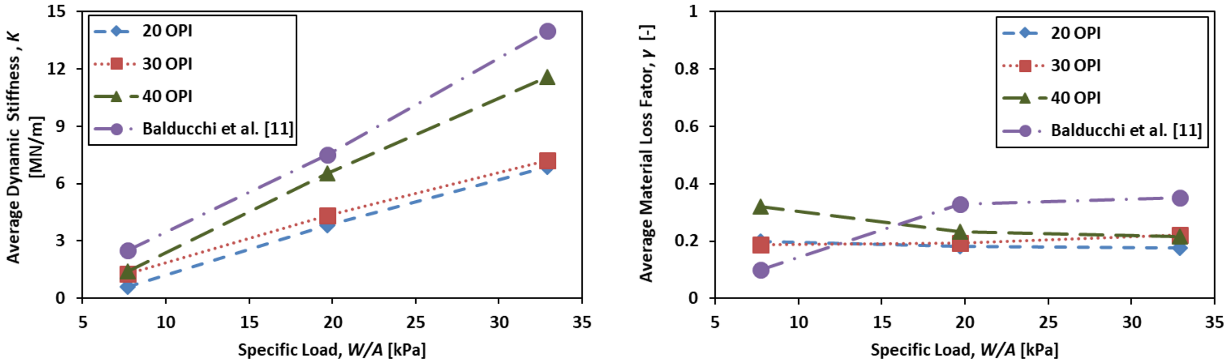

(a) Stiffness versus applied load

(b) Loss factor (γ) versus applied load

Figure 22. Average foil bearing stiffness and material loss factor versus applied specific load (*W*/*A*) for four thrust foil bearings. Results valid for 40 Hz ≤ *f* ≤ 300 Hz.

4.2 TESTS WITH ROTOR SPEED

Before conducting tests with rotor speed, a profilometer measures the step heights on all six pads of three top foils as well as the rotor collar surface. The rotor collar has an average roughness (RMS) of ~1.5 μm. In addition to roughness measurements on the collar surface, a precise (± 2 μm) dial gauge determines the mechanical runout on the collar surface to be less than (or equal to) 12 μm when installed on the router motor.

Figure 23 (a) displays a magnified image of a single pad installed in a profilometer as well as the scan direction (from left to right in the figure) and scan length (1,000 μm). Figure 23 (b) shows the corresponding profile along the scan length. Tape secures the pads four edges to the profilometer surface before the start of each scan. In addition, each pad is scanned three times at its mid radius, the average magnitude representing the step height. The scans show very uniform step heights, $h_S \sim 20\ (\pm 2)$ μm for all the top foils.

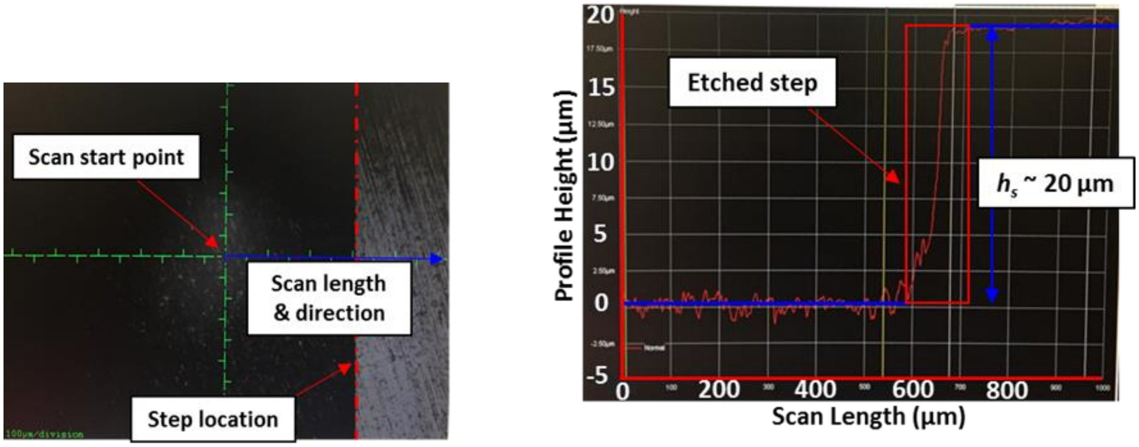

(a) Magnified image of a single pad (b) Corresponding profile along scan

Figure 23. Magnified image of a single pad and corresponding profile produced with an industrial profilometer.

When applying an industrial spray lubricant ($\mu = 0.02$ Pa.s) to the pads a maiden test of the MMFTB (without recording data) at a rotor speed $\Omega = 15$ krpm ($\omega R_{PO} \sim 80$ m/s) proved the bearing concept. Figure 24 displays the post-test condition of the top foil, showing clear wear marks along the pads leading edges as well as (uneven) wear near the pads centers, starting at the step locations. This first test revealed that the Parylene® coating is not robust enough to withstand intermittent solid contact between the rotor collar and top foil. In addition, the wear at each pad leading edge is attributed to windage, lifting the thin top foil pads and pushing them into contact with the thrust collar. To ensure the pads lay flat for future tests, a heat resistant adhesive bonds the test top foil to the top mesh layer.

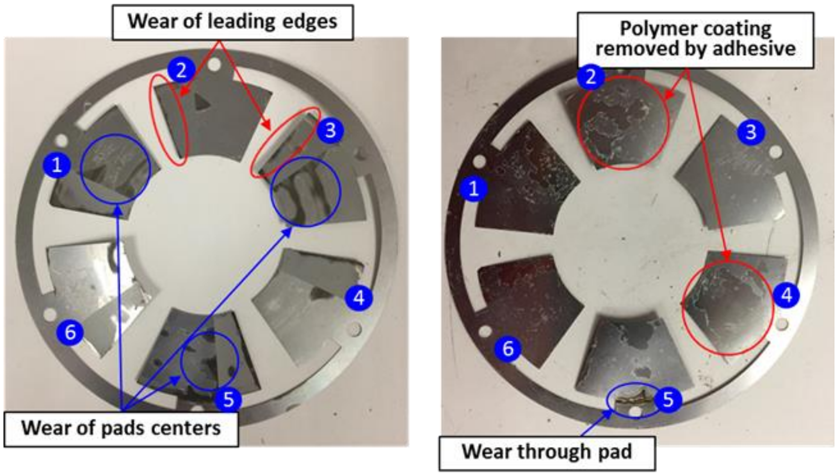

(a) Front side of top foil (b) Back side of top foil

Figure 24. Post-test condition of a Rayleigh-step top foil with steps located 15° from the pads leading edges. Wear marks visible at leading edges and pads centers.

Following the test to prove the concept, six thermocouples install around the bearing circumference to monitor the health of the test bearings, while a torque measurement system determines the bearing drag torque. Figure 25 (a) displays a prototype MMFTB with two sheets of 20 OPI mesh and a 22.5° Rayleigh-step top foil installed in the test rig (see Figure 7). In the figure, note that the shaft rotation direction is counterclockwise. Six small (40 gauge wire) thermocouples locate at the top foil fixture locations, touching the underside of the thin metal.

Figure 25 (b) pictures the back side of the thrust load shaft where a lever arm (l ~ 40.6 mm) pushes on a strain-gauge type load cell to render the bearing drag torque.

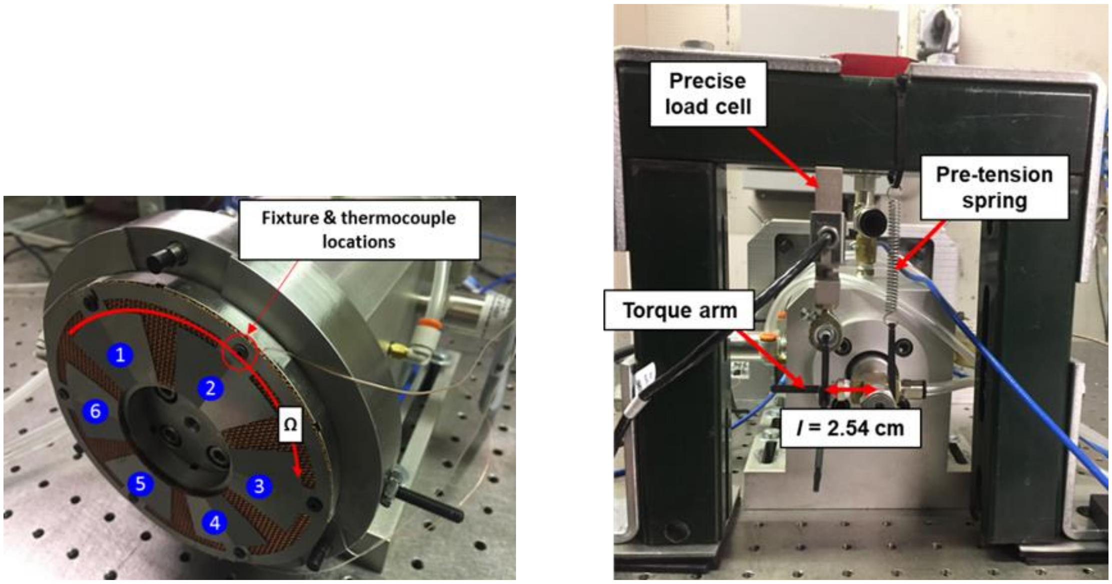

(a) Test-bearing installed on load shaft (b) Torque measurement system on load shaft

Figure 25. Photographs of (a) test bearing installed on load shaft and (b) a torque measurement system for the test bearing.

Without rotor speed, a small thrust load (W/A ~ 7.5 kPa) applies to the test bearing, pushing it into the collar and establishing a contact point where there is no clearance between the test bearing and rotor. During operation with rotor speed, the distance between the eddy current sensors and this zero gives a metric of the bearing clearance (for the given load).

To maintain the integrity of the bearings, the router motor accelerates the rotor collar to Ω = 40 krpm without the test bearing engaged. Once the collar comes up to speed, the test bearing slowly approaches the collar until it supports a small thrust load (W/A ~ 7.5 kPa or 1 psi). During the tests, the rotor speed holds constant and cooling flow applies to the bearing at a rate of 200 SLPM. For a test MMFTB with 2 sheets of 20 OPI mesh and a Rayleigh-step with $\Theta_L = 15°$, Figure 26 displays graphs of the bearing center clearance (described above) and drag torque versus time as well as top foil temperature versus time.

As soon as a small load applies to the test bearing the drag torque rises, increasing nearly linearly with time. Note that the bearing stays ~300 μm from the pre-established zero, indicating either a 300 μm film thickness or pad distortion. In addition to the bearing torque, the pad fixture temperatures increase rapidly after application of the small load, with the fixture location of Pad 3 rising from ~ 27 °C to just under 60 °C in ~ 10 s.

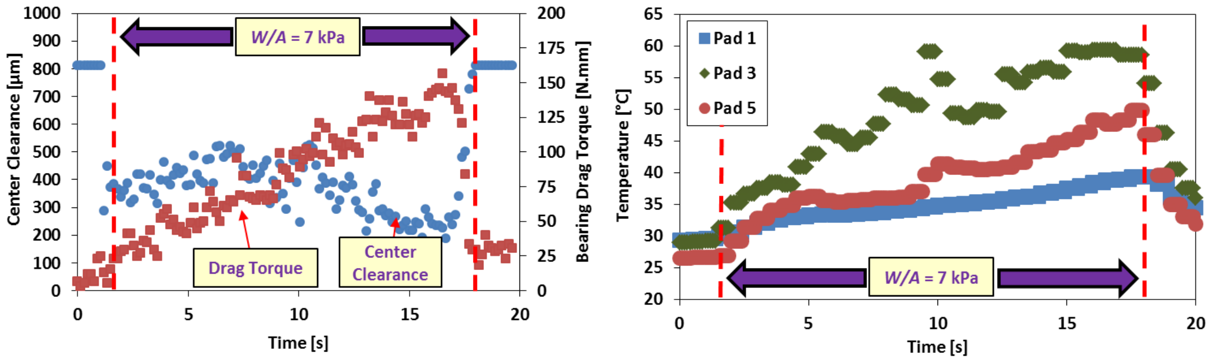

(a) Bearing drag torque and center clearance (b) Top foil temperatures

Figure 26. Bearing clearance (from loaded position), drag torque, and top foil temperature versus time. Rayleigh- step bearing with Θ_L = 15°, Ω = 40 krpm (212 m/s at bearing OD).

The same behavior was apparent for the Rayleigh-step bearing with steps located at 22.5°, as well as for the negative slant bearing; each bearing showing dramatic temperature rise for even a small thrust load (*W/A* = 7.5 kPa). However, during operation with the negative slant bearing, metal-to-metal contact between the collar and top foil was evident immediately, producing visible sparks and causing the operator to discontinue the test immediately. Figure 27 displays post-test conditions of the three top foils. Note that the top foils were all fixed in the same manner, as depicted in Figure 25 (a), to maintain uniformity between tests.

The post-test photographs show dramatic and devastating wear to one (or multiple) pads of each top foil. Comparing the photographs in Figure 27 to the post-test condition of the top foil from Figure 24, there is almost no wear along the pads leading edges, showing that the adhesive effectively prevents the pads from lifting due to windage. Considering the photographs in Figure 27, the damaged pads are not in the same locations from one test bearing to the next, as would be expected in the case of test rig misalignment. For the negative slant bearing, Pad 1 is severely damaged; whereas Pads 2, 3 & 4 are damaged for the 22.5° bearing and Pads 3 & 5 for the 15° bearing.

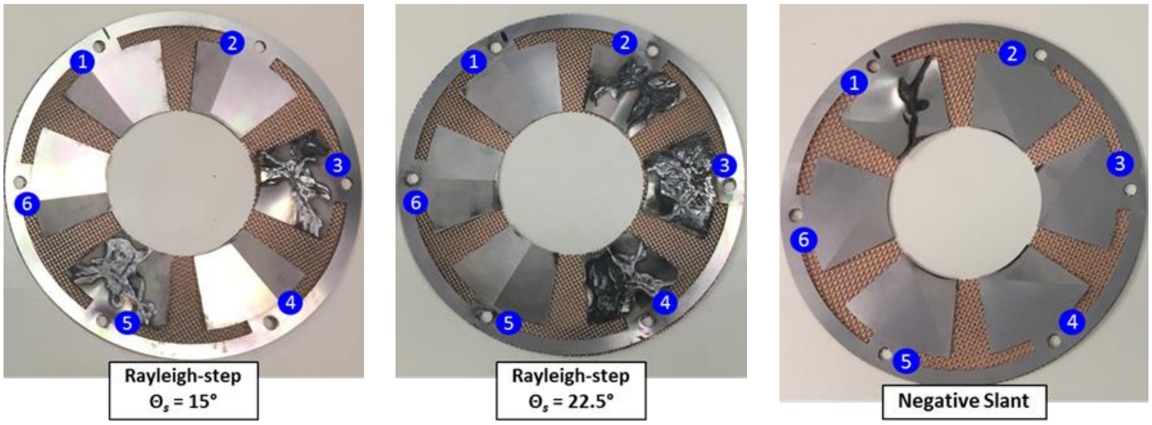
Rayleigh-step $\Theta_s = 15°$

Rayleigh-step $\Theta_s = 22.5°$

Negative Slant

Figure 27. Photographs depicting post-test conditions of three Rayleigh-step top foils implemented on a prototype MMFTB.

The seemingly random damage pattern from one bearing to the next implies that certain pads bulge towards the rotor collar upon assembly, while others do not. Figure 28 displays a photograph of a single layer of 20 OPI mesh, showing it to be uneven and wavy. When multiple layers of mesh stack on-top of each other, this unevenness compounds. In addition, the six fixture holes for the mesh and top foil locate near the structure OD. When assembled, these fixtures compress the mesh at the OD while lifting the mesh ID towards the rotor.

Figure 28. Photograph of a single layer of 20 OPI mesh depicting the inherent waviness in the thin structure.

Experiments with rotor speed, while briefly proving the bearing concept, also reveal that:

1. The inherent waviness of the metal mesh bulges the thin top foil upon installation. As the thrust collar approaches the bearing, the bearing top foil contacts the spinning collar before a hydrodynamic pressure forms on its surface.
2. Windage and a poor anchoring method exacerbates this bulging.
3. The foil bearing necessitates a more robust sacrificial coating to withstand intermittent rubs between the collar and foil.

Combined, these issues show the etched Rayleigh-step concept to be infeasible. A redesign of the MMFTB must address to the issues listed above.

5. EXPERIMENTS WITH A CIRCUMFERENTIALLY TAPERED METAL MESH FOIL THRUST BEARING

5.1 A CIRCUMFERENTIALLY TAPERED METAL MESH FOIL THRUST BEARING

Most foil thrust bearings utilize a circumferential taper, formed either by a bend in the top foil itself, or by a height change between the top foil fixed end and the start of the underspring structure [9,15,21,24]. A redesign of the MMFTB incorporates several sector shaped pads which have circumferential tapers from the pad leading edges to the start the metal mesh pads.

Figure 29 displays two schematics of a foil thrust bearing comprising of six sector-shaped pads (top foils), each supported by a single (or multiple) metal mesh pads. The thin top foils fix to a solid metal bearing support along a milled slot, intended for cooling flow. When fixed to the bearing, the top foils initially do not have a bend, but rely on the height change between the bearing support surface and the top of the mesh pad to form a circumferential taper, i.e. hydrodynamic wedge. As hydrodynamic pressure builds on the top foil surface, the foil deforms elastically to the shape depicted in Figure1.

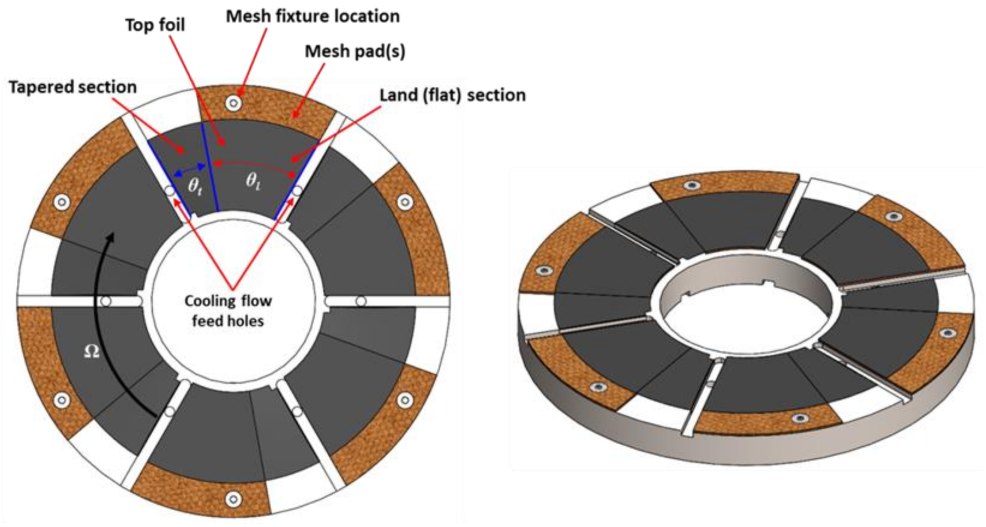

(a) Top down view

(b) Isometric view

Figure 29. Top down and isometric views of a six-pad circumferentially tapered metal mesh foil thrust bearing.

Table 7 contains geometry and operating conditions of a single pad MMFTB, as well as an insert which displays a photograph of the bearing, assembled on the test rig displayed in Figure 7. The top foil is 316 stainless steel (SS), coated with a sacrificial layer of MoS_2[3]. In addition, the bearing support consists of three layers of 40 openings per inch (OPI) copper metal mesh[4]. As displayed in the insert, a single K-type thermocouple affixes to the underside of the SS top foil, locating at the pad midspan in the tapered portion, just before the metal mesh support. It should be noted that this prototype bearing was formed quickly, with components (top foils and mesh pads) cut by hand. In addition, the pad arc extent is 55°, extending from the end of one milled cooling in steel bearing support, to the start of the next.

---

[3] The coating thickness was not measured but was applied to coat the entire pad surface.

[4] See Chapter 3 for details on the mesh.

Table 7. Geometry and operating conditions for the current analysis.

Geometry and Mesh	
Inner Diameter, *Di*	0.0508 [m]
Outer Diameter, D_o	0.1016 [m]
Pad Extent, θ_P	55 [°]
Pad Tapered Extent, θ_t	25 [°]
Operating Conditions	
Ambient Pressure, P_a	101.4 [kPa]
Rotational Speed, Ω	35-40 [rpm]
Specific Load, W/A_{pad}	6.9-34.5 [kPa]
Gas Supply Temperature, T_s	296 [K]

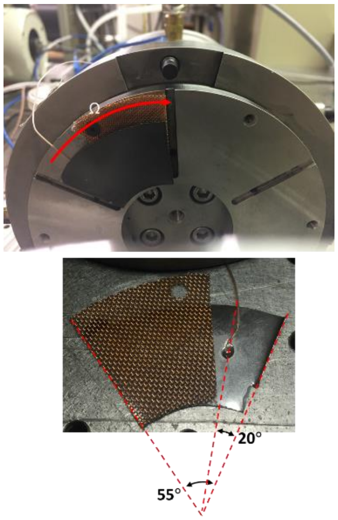

5.2 TESTS WITH A SINGLE-PAD METAL MESH FOIL THRUST BEARING

Chapter 5 details multiple failures of a Rayleigh-step MMFTB with six pads and a SS top foil. Tests with the Rayleigh-step bearing emphasized the need of a sacrificial coating on the top foil as well as showing the influence of windage on the top foil structure. The single-pad bearing displayed in Table 7 represents a second prototype, aimed at overcoming the deficiencies of the Rayleigh-step bearing. Epoxy fixes the thin top foil at the pad leading edge to a cooling channel of the bearing support. During startup, the underside of the top foil is not in contact with the mesh support. When the rotor collar spins, and approaches the top foil, windage flattens the top foil against the mesh support, forming a circumferential taper from the pad leading edge to the start of the mesh structure (as displayed in Figure 29).

For the current experiments, the test rig electric motor spins the solid steel thrust collar at a constant speed Ω, maintained by the VFD and measured with an optical tachometer. Once the rotor collar is at speed, pressurized air enters the aerostatic loading plenum to apply a static thrust load to the test bearing. The pressure in the plenum (measured via a high precision pressure transducer) along with the load shaft surface area determines the thrust load on the bearing. A high precision strain gauge type load cell and lever arm (attached to the thrust load shaft) provide a means of measuring the bearing drag torque (Figure 25).

With the rotor collar at speed (Ω = 35 or 40 krpm), a small load applies to the test bearing to engage the pad, pressing the foil against the mesh support and forming a hydrodynamic wedge which separates the collar and stationary surfaces. Once the bearing engages, a Labview® program operates a control value on the aerostatic loading plenum to increase the bearing specific load by 3.45 kPa (0.5 psi) every 60 seconds. The DAQ records the top foil temperature, rotor speed, and plenum pressure at a slow sampling rate (16 samples/s). The Labview® program samples the static load cell (for bearing drag torque determination) as well as the signals from the three eddy current sensors on the thrust load shaft, however, at 102,400 samples/s with the mean of every 6,400 samples recorded[5].

Figure 30 displays the measured bearing drag torque versus applied specific load for a single pad bearing with rotor collar speed Ω = 40 krpm ($\omega \cdot r_{mid}$ ~160 m/s) and no cooling flow. First and foremost, the data in Figure 30 shows that an air film forms between the rotor collar and the circumferentially tapered MMFTB, proving the concept. Figure 30 (a) shows that the plenum controls the applied specific load well, incrementing the load in a stepwise, uniform manner. The

---

[5] This method is employed to determine a steady state torque and bearing center displacement as well as to match the sampling rates of the rotor speed, plenum pressure and pad temperature.

bearing drag torque, Figure 30 (b), displays a similar trend, increasing with each load step, and leveling out to a steady state value quickly. At higher loads (W/A_{pad} > 30 kPa) the drag torque increases dramatically upon an increase in the static load, evidencing rub between the collar and top foil.

Note that locating the torque measurement system on the backside of the bearing loading shaft (see Figure 25 (b)) isolates the MMFTB drag from any windage on the thrust collar backside or outer diameter. A calibration of the torque measurement system prior to operation of the rig with rotation shows a maximum difference (uncertainty) of ~10% between measurements with a digital screwdriver at the frontside of load shaft (where the bearing locates) to that of the load cell force multiplied by the torque lever arm ($T = F \cdot L$). In addition to benchmarking the uncertainty of the torque measurement system, the calibration reveals that the porous graphite bushings, which float and support the bearing load shaft, contribute negligible torque to the system.

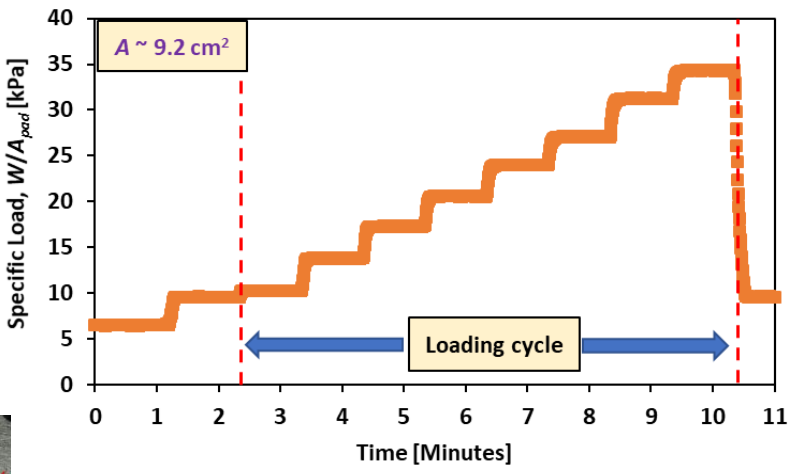

(a) Specific load vs time

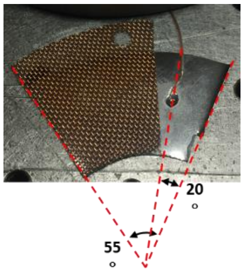

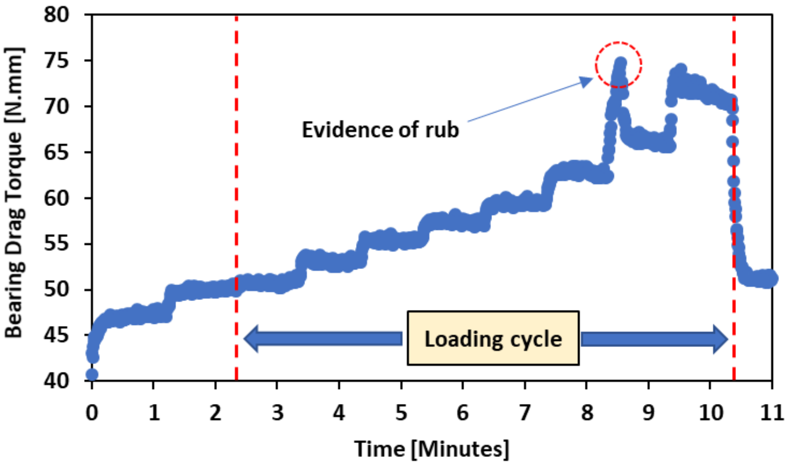

(b) Drag torque vs time

Figure 30. Applied specific load and bearing drag torque for a single pad MMFTB and collar speed Ω = 40 krpm ($\omega \cdot r_o$ ~ 213 krpm).

For the single pad MMFTB with dimensions as displayed in Table 7, 60 seconds at each load was enough time to determine a steady state drag torque. To determine the effect of cooling flow, the test described above repeated for three different flow rates (100, 200 & 300 SLPM) and two rotor collar speeds Ω = 35 and 40 krpm ($\omega \cdot R_o$ = 186 & 213 m/s). The tests utilized the same top foil, simply applying MoS_2 to the pad surface between tests and ensuring the entire pad surface was covered.

Figure 31 displays steady state bearing drag torque versus applied load for the three different flow rates, as well as for a bearing with no cooling flow. Measurements displayed in Figure 31 show that the bearing drag torque increases nearly linearly with applied load, and that for the two collar speeds (Ω = 35, 40 krpm) cooling flow supplied through the bearing center has little to no influence on the drag torque. Comparing the drag torque at the two thrust collar speeds (35 & 40 krpm), at low loads (W/A_{pad} < 20 kPa), the torque is smaller for Ω = 35 krpm by ~ 30%. Note that predictions for the MMFTB (displayed later) show that the bearing drag torque is largely insensitive to cooling flow, due to the low viscosity of air.

Figure 31 (b) also includes bearing drag torque measurements for a bump-type foil thrust bearing with similar dimensions (*ID* = 50.8 mm, *OD* = 101.6 mm) and with six pads [19]. Note that the measurements reproduced from Ref. [19] are for the entire six-pad bearing. Overall, the magnitude of the MMFTB drag torque (displayed in Figure 31) is quite high, with the entire similar BFTB (Stahl [19]) exhibiting a smaller drag torque at Ω = 40 krpm. Since the bearings have similar dimensions (ID, OD, taper height, pad and taper extent) and a similar underspring stiffness (as displayed in Figure 17), the large difference in drag torque measurements is attributed to the test bearing operating in the mixed-lubrication regime, with continuous sliding contact between the runner and top-foil (a simple Couette flow approximation, presented later, corroborates this notion).

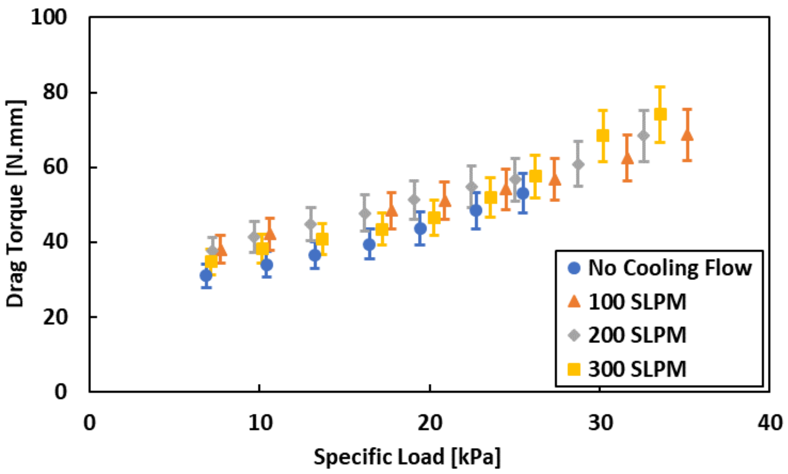

(a) Collar speed Ω = 35 krpm ($\omega \cdot R_o$ = 186 m/s)

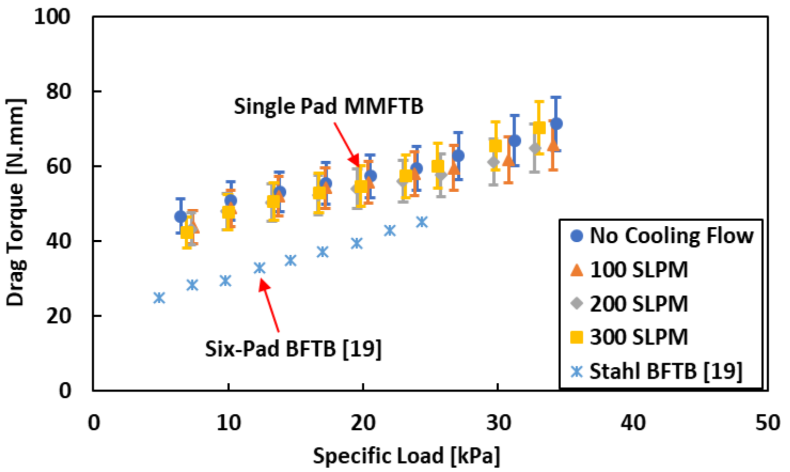

(b) Collar speed Ω = 40 krpm ($\omega \cdot R_o$ = 213 m/s)

Figure 31. Steady state bearing drag torque for a circumferentially tapered single pad MMFTB.

Due to a high sample rate and the length of the test (exceeding 45 minutes for full bearing tests) the LABVIEW® program only recorded the bearing center displacement (average of the three displacement sensor values). A static collar tilt, causing a minute film thickness (and even sliding contact) on some pads could explain the discrepancy displayed in Figure 31 (b); However, without measurements at the individual sensor locations, the actual cause of the discrepancy is currently undetermined.

Figure 32 displays a photograph of the thrust collar after a test with the single pad MMFTB at Ω = 40 krpm and with no applied cooling flow. After extensive testing (with the Rayleigh-step bearing as well as the taper-land bearing), intermittent contacts between the collar and the bearing pads, during startup and operation, had worn down the layer of thin-dense chrome on the collar surface, originally 25.4 μm thick. In addition to the unevenness to of chrome coating (not measured), the surface of the collar has depositions of MoS_2 from intermittent contact with the prototype taper-land bearing. When operating with a small film thickness (sometimes less than 5 μm, as shown later in predictions), these particles presumably create continuous sliding contacts between the rotor and the pad surface, and while note definitive, likely increase the bearing drag torque.

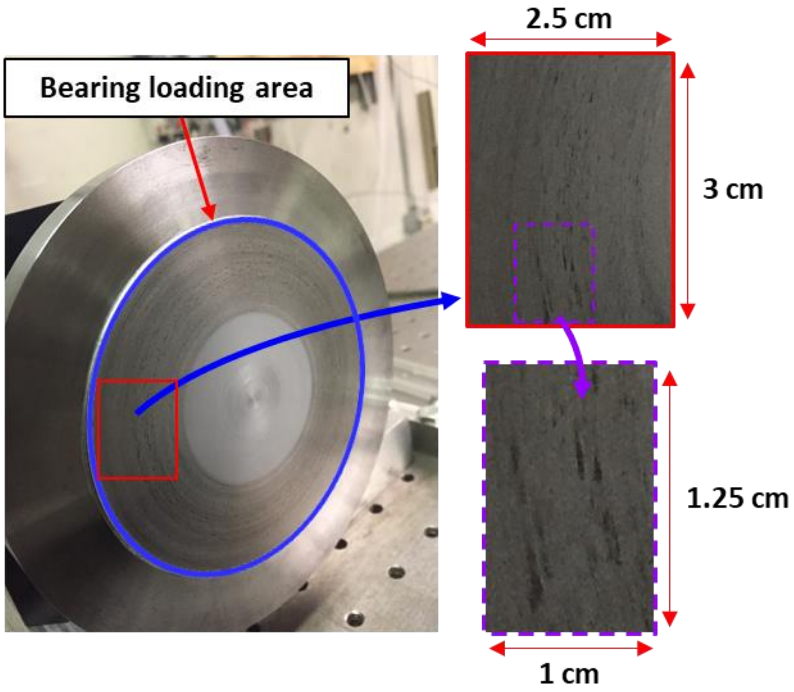

Figure 32. Post-test condition of the thrust collar surface, showing deposits of MoS_2 on its surface.

In addition to bearing drag torque, tests with the single-pad bearing also record relative displacement between the test bearing and steel thrust collar at three eddy current sensors located around the bearing circumference (120° apart). After the test bearing engages the spinning collar and supports a 6.7 kPa (1 psi) specific load, the LabVIEW® program establishes a zero (null displacement). Figure 33 displays the recorded bearing center displacement from this null position versus time while Figure 34 displays the temperature rise versus time obtained from four different tests under operation with $\Omega = 40$ krpm and varying amounts of cooling flow. Note that the actual distance between the collar and the bearing support is unknown at this null position, thus, a clearance cannot be determined with the following data.

Like the bearing drag torque and applied load traces displayed in Figure 30, the data in Figure 33 shows that the bearing displacement responds to the stepwise increase in the applied load, also moving in steps. For all tests, the bearing displaces ~ 40 μm from the established zero. This behavior shows the repeatability of the measurements, but also shows that the applied cooling flow does not have a significant effect on the film thickness (and drag torque) over the single pad.

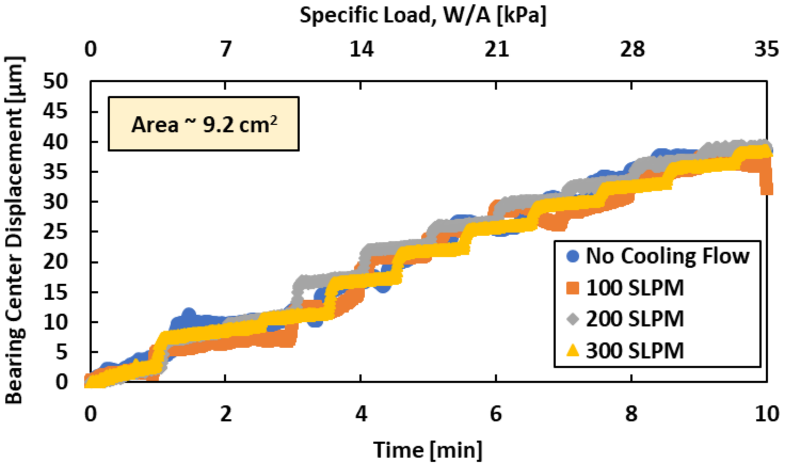

Figure 33. Bearing center displacement for four different tests with a single pad circumferentially tapered MMFTB and Ω = 40 krpm.

Figure 34 shows the pad temperature rises ~25 °C as the load increases from *W/A* = 6.7 – 35 kPa for the three tests with applied cooling flow. Without cooling flow, the bearing experiences a clear rub and has a total temperature rise of ~40 °C. In addition, increases the ambient temperature (T_∞) by ~5 °C over the length of the test (~11 minutes). Results in Figure 34 show that cooling flow has some effect on the pad (and likely the film) temperature; however, as shown in Figure 31 (b), the slight difference in temperature is not enough to significantly change the bearing drag torque. In addition to the bearing pad temperature rise, note that the ambient temperature surrounding the bearing is relatively constant, increasing by only 5 °C over the entire load cycle (W/A = 6.7 – 35 kPa)[6] due to mixing of hot air expelled from the bearing OD and heat generation at the collar OD (i.e. windage).

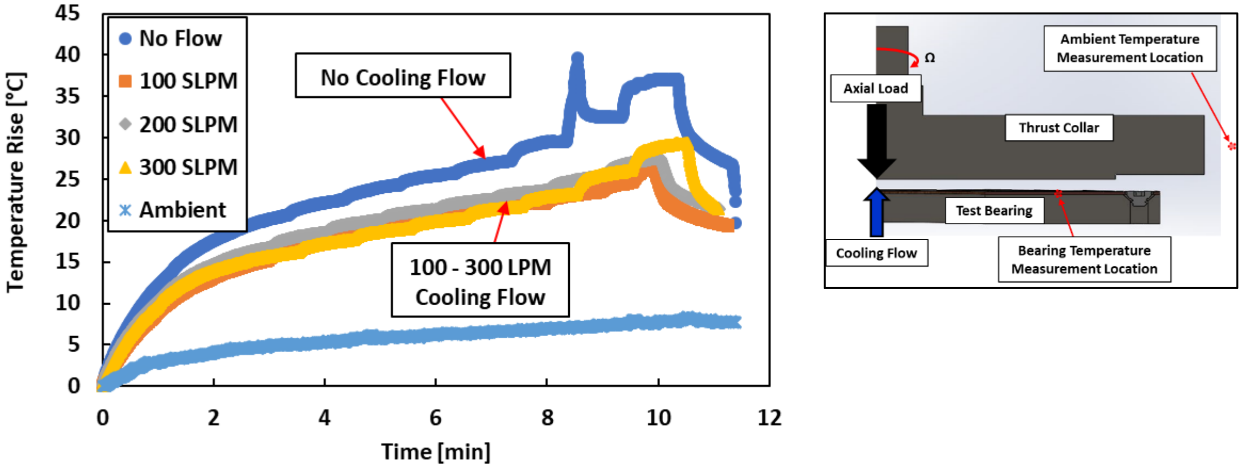

Figure 34. Top foil temperature rise for four different tests with a single pad circumferentially tapered MMFTB and Ω = 40 krpm.

Figure 35 (a) displays specific load vs. measured bearing center displacement while Figure 35 (b) shows a MMFTB bearing stiffness (film + underspring in series) versus applied specific load derived from this steady-state data for a single pad MMFTB with no cooling flow and operation with $\Omega = 40$ krpm ($\omega \cdot R_o = 213$ m/s). The single point (steady state) values represent an average of the displacement and load data over the duration of a load step (90 s). Third-order polynomials fit

---

[6] The ambient temperature at the end of the test was $T_\infty \sim 38$ °C.

the load versus displacement data ($R^2 > 0.99$), with derivative ($K_{MMFTB} = dF / dZ$) representing the total bearing stiffness in series (film + top foil & underspring). A static (Ω = 40 krpm) stiffness, determined by pushing the collar into the single-pad test bearing when no rotor speed applies, allows for determination of a fluid film stiffness when the bearing operates with a rotor speed.

$$\frac{1}{K_{MMFTB}} = \frac{1}{K_{Film}} + \frac{1}{K_{MM}} \quad \rightarrow \quad K_{Film} = \left(\frac{1}{K_{MMFTB}} - \frac{1}{K_{MM}} \right)^{-1} \tag{10}$$

Uncertainty in the film stiffness propagates from uncertainty of the metal mesh stiffness (K_{MM}) as well as that of the bearing (K_{MMFTB}) [61]

$$U_{K_{Film}} = \left[\left(\frac{\partial K_{Film}}{\partial K_{MMFTB}} U_{K_{MMFTB}} \right) + \left(\frac{\partial K_{Film}}{\partial K_{MM}} U_{K_{MM}} \right) \right]^{1/2} \tag{11}$$

where $U_{K_{MMFTB}}$ & $U_{K_{MM}}$ are determined from the least squares fitting errors of the load versus displacement data with and without rotation, respectively. Note that the current error estimation does not include bias (repeatability) uncertainty, as the data in Figure 35 is extracted from a single test. A more rigorous, development would include multiple runs of the bearing to assess the repeatability of the data. However, before more tests were conducted, the test rig experienced a failure (described later) which prevented further testing with the prototype MMFTB.

Results in Figure 35 give a **rough** estimate of bearing stiffness for Ω = 40 krpm ($\omega \cdot R_o = 213$ m/s) loads $17 \leq W/A \leq 35$ kPa for a single pad MMFTB. At loads below 17 kPa, the stiffnesses of the structure alone (K_{MM}) as well as that of the full bearing (K_{MMFTB}) are too similar to extract a meaningful film stiffness. The bearing stiffness $K_{MMFTB} = 0.5 – 1.2$ MN/m for specific loads $W/A = 17 – 35$ kPa while the approximated fluid film stiffness $K_{Film} = 1.75 – 3. 5$ MN/m over the applied load range.

The total bearing stiffness (K_{MMFTB}) and metal mesh stiffness (K_{MM}) have little associated uncertainty, as they are determined from the measured load and displacement behavior (with a precise pressure transducer and three eddy current sensors) with and without rotation, respectively. While the data in Figure 35 gives a first estimate for the air film stiffness in a MMFTB, the analysis disregards any misalignment (tilting) of the collar and determines the axial stiffness coefficients from a single set of data, neglecting to ascertain if the data is repeatable.

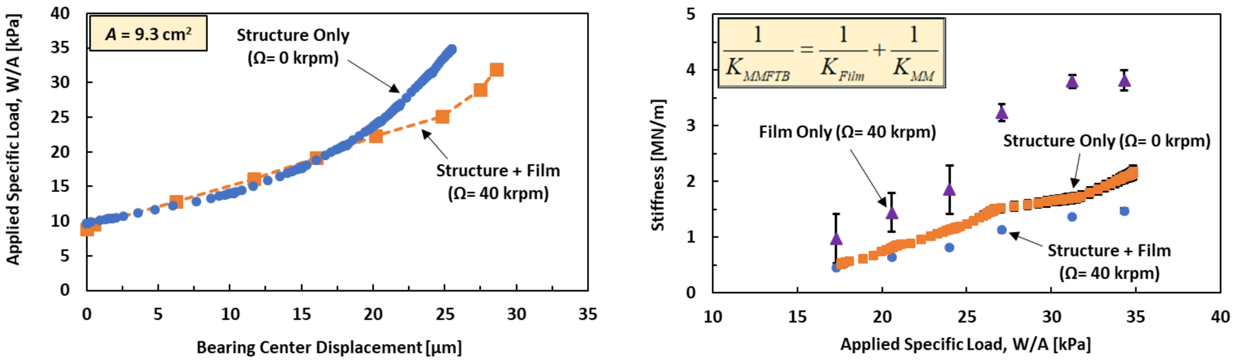

(a) Specific load vs center displacement

(b) Derived bearing stiffnesses

Figure 35. (a) Load vs displacement and (b) Approximate bearing and air film stiffnesses for a single pad circumferentially tapered MMFTB and Ω = 40 krpm.

Figure 36 displays four photographs of the single pad bearing, taken in between subsequent tests at Ω = 40 krpm. Figure 30 (b) shows a large torque spike during operation, indicating solid contact between the rotating collar and the stationary pad as confirmed by the images in Figure 36. The photographs show that the wear locates mostly at the transition between the taper and land regions as well as at the pad outer diameter, with more wear occurring when less cooling flow applies to the bearing. This behavior indicates that the bearing with no cooling flow (or a smaller amount of) operates with a slightly smaller film thickness under the same applied load.

During intermittent contact, the sacrificial coating (MoS_2) maintained the integrity of the top foil, but did deposit onto the thrust collar surface, presumably adding to the bearing drag torque. After each test the operator cleaned the thrust collar surface and applied additional MoS_2 to the pad to cover the worn areas.

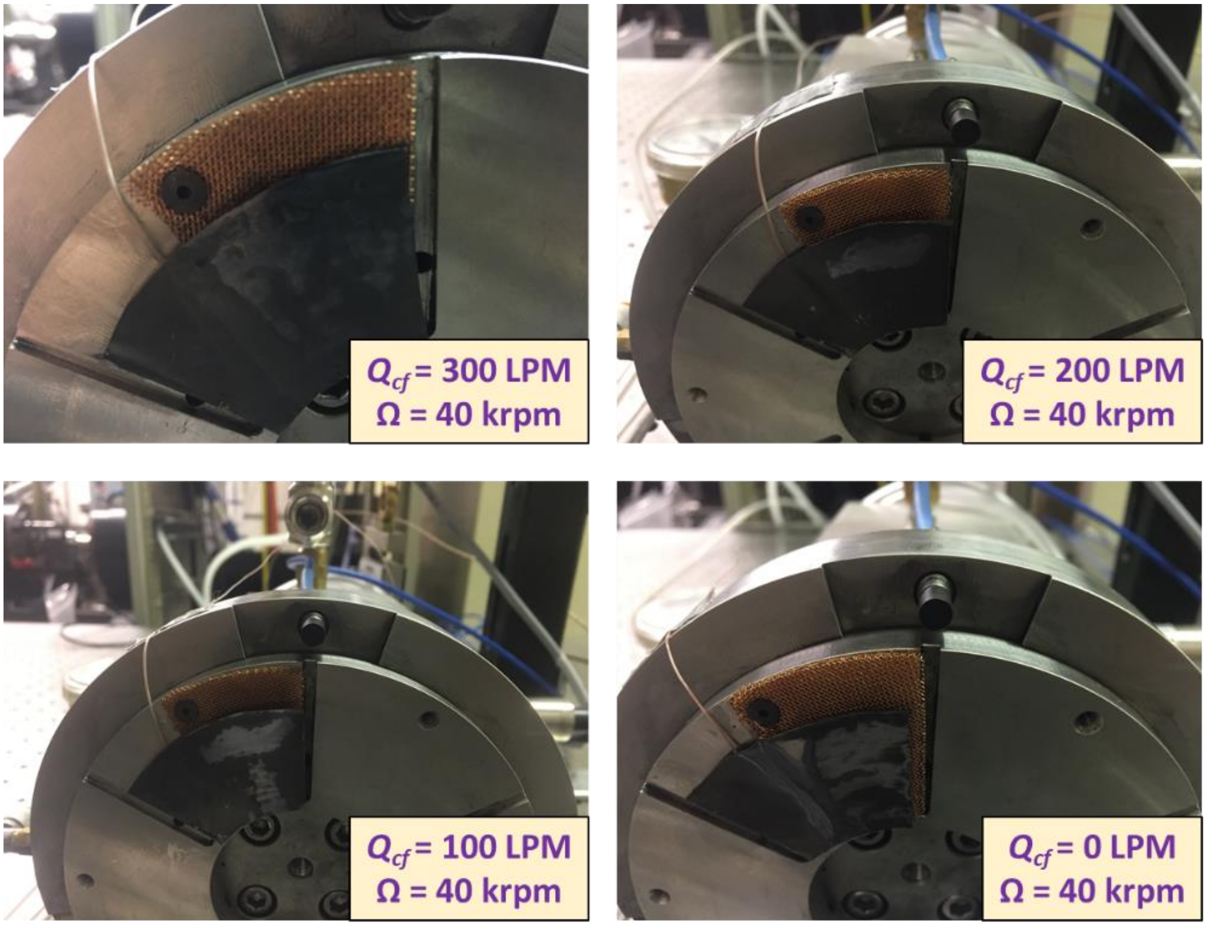

Figure 36. Post-test photographs of a single pad bearing with visible wear.

5.3 TESTS WITH A SIX-PAD METAL MESH THRUST FOIL BEARING

After proving the bearing concept with a single pad, tests moved to a six-pad bearing, again with SS top foils and 3 sheets of 40 OPI mesh beneath each pad. Labview® controls the static loading of the test bearing, increasing in 1.72 kPa (0.25 psi) steps every 180 s. Figure 37 displays two photographs of a six-pad MMFTB assembled on the test rig load shaft. As with the single-pad bearing, each pad top foil affixes to a machined slot in the bearing base via epoxy while three thermocouples monitor the bearing health (at the locations depicted in the figure).

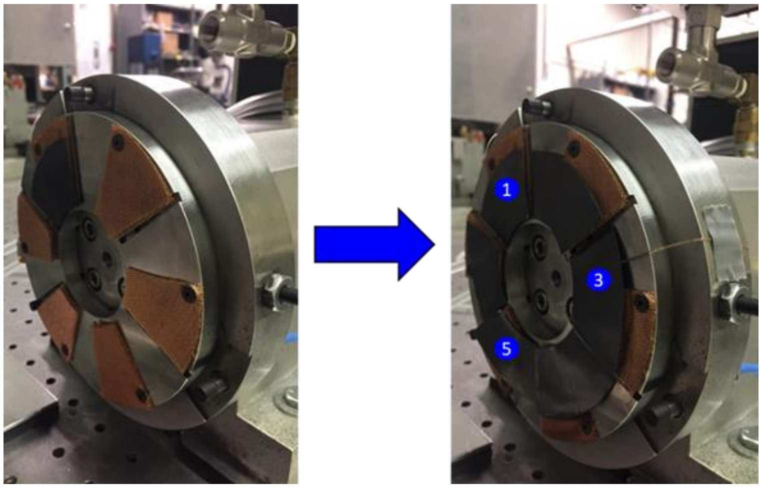

Figure 37. Photographs of a six-pad circumferentially tapered MMFTB indicating pads with thermocouples to measure pad temperature.

Although thrust foil bearings do not typically support large loads (due to the low viscosity of gas), a successful MMFTB should be able to support at least, *W*/*A* = 35 kPa (5 psi) for commercial applications such as automotive turbochargers [5]. The six pad MMFTB, displayed in Figure 37, underwent several tests, attempting to reach a thrust load of 35 kPa with the collar spinning at

Ω = 40 krpm. Unfortunately, at best, the bearing reached W/A = 25 kPa before incurring large (uncontrollable) temperature or torque increases.

Figure 38 displays a break-in process for the six-pad MMFTB operating with 300 SLPM of cooling flow and at Ω = 40 krpm. As described in Ref. [19], the load capacity of a foil thrust bearing increases (to a point) as the rotating collar essentially laps the pads, and the surfaces begin to mate, more uniformly distributing the thrust load amongst the pads. During the initial break-in runs (1-3), at the beginning of a new load step, the drag torque increases dramatically, then decreases and levels off to a steady state value. This process evidences, again, intermittent contact between the rotating collar and the bearing pads, touching for a brief time before the surfaces mate and a full film forms to separate the surfaces.

During each run, a torque spike eventually occurs, indicating a sustained rub and that the bearing load capacity is reached. In Ref. [19], the operator continued operation, but decreased the load by 20%, allowing the bearing to reach steady state before increasing the load once again. For the experiments herein, after a sustained rub, the operator discontinued the test and allowed the bearing and rotor collar to return to ambient temperature before conducting another test. After the fourth run and reaching a bearing load of W/A ~ 25 kPa, subsequent runs no longer increase the bearing load capacity.

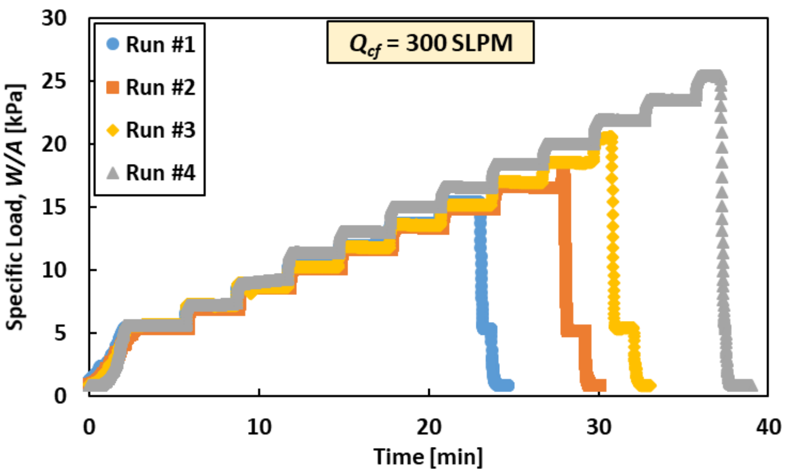

(a) Applied specific load vs. elapsed time

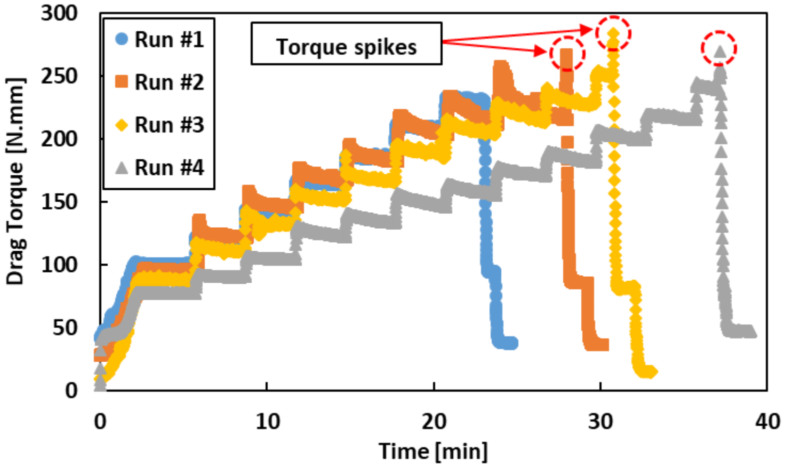

(b) Bearing drag torque vs. elapsed time

Figure 38. Break-in process for a six-pad circumferentially tapered MMFTB operating with 300 LPM of cooling flow and Ω = 40 krpm.

Figure 39 displays applied specific load, bearing drag torque and pad temperature versus time for the broken-in six-pad MMFTB operating at Ω = 40 krpm and with 300 SLPM of cooling flow. Even for the broken-in bearing, the temperature of pads 1 & 3 is similar, while pad 5 is approximately 20 °C cooler for the entire loading cycle. This discrepancy in pad temperatures shows that the load carrying is not evenly distributed amongst the six pads. After the run, test rig alignment was verified, which revealed an inherent issue with the test bearing. Despite purchasing uniform mesh, and even having pads with similar measured heights, stacking layers of the mesh continued to produce pads with varying taper heights during operation.

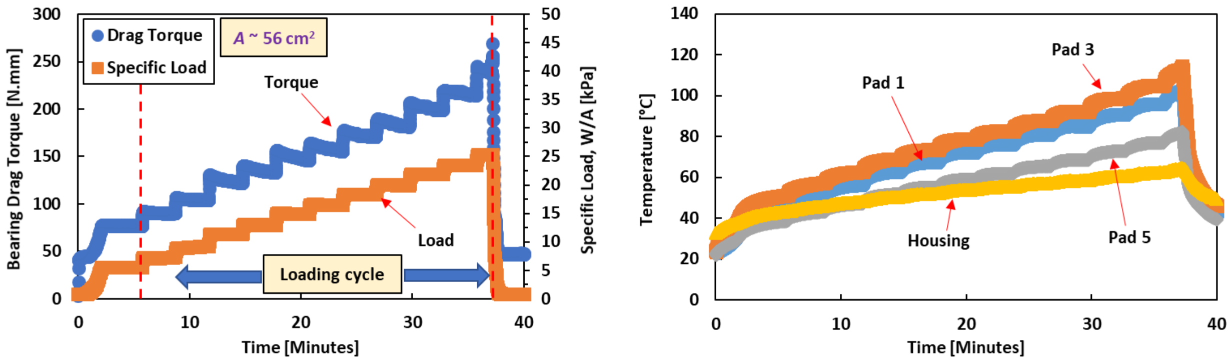

(a) Specific load and drag torque vs time

(b) Pad temperature vs time

Figure 39. Specific load, bearing drag torque, and pads' temperatures versus time for a broken-in six-pad circumferentially tapered MMFTB operating with 300 SLPM cooling flow and at a rotor speed Ω = 40 krpm.

As with the single pad bearing, three eddy current sensors on the test bearing load shaft measure the test bearing center displacement during operation. Again, tests take a zero position (null displacement) when the test bearing supports a load of W/A = 6.7 kPa (1 psi). Figure 40 (a) displays applied specific load (W/A_{MMFTB}) versus test bearing center displacement from the established zero for Ω = 0 & 40 krpm, as before. At the beginning of the loading cycle, the bearing displacement is linear. As is typical of foil bearings, as the load increases more of the underspring structure engages, and the displacement becomes nonlinear (stiffening effect). Uncertainty in the derived stiffness follows the same method as described above (see Eq. (10)).

Figure 40 (b) displays a MMFTB bearing stiffness (film + underspring in series) versus applied specific load derived from the steady-state load versus bearing displacement data (see Figure 40 (a)) for the six-pad bearing. As with the single-pad bearing, each steady state value (load and displacement) represents an average over an entire load step (i.e. 180 s). Do note that the single-pad bearing was able to hold a specific load W/A = 35 kPa, whereas the run-in six-pad MMFTB had a maximum load capacity of 25 kPa. As such, Figure 40 (b) shows the six-pad bearing stiffness ($1 \leq K_{MMFTB} \leq 2.5$ MN/m) for loads comprised between $6.7 \leq K_{MMFTB} \leq 20$ kPa, one load step before the bearing load capacity. The derived film stiffness ($3 \leq K_{Film} \leq 8$ MN/m), most uncertain at low loads where the bearing and mesh stiffness are similar, is larger than that of the underspring for the entire loading cycle. This behavior indicates that the structural characteristics of the mesh dictate the performance of the bearing. As with the results for the single-pad bearing, the current analysis considers only a single trial with the run-in prototype MMFTB, and therefore neglects to ascertain if the data is repeatable.

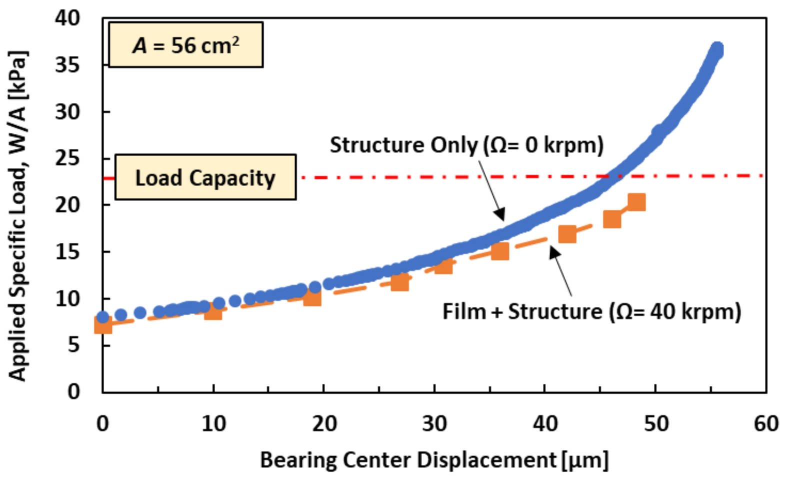

(a) Applied specific load versus bearing center displacement

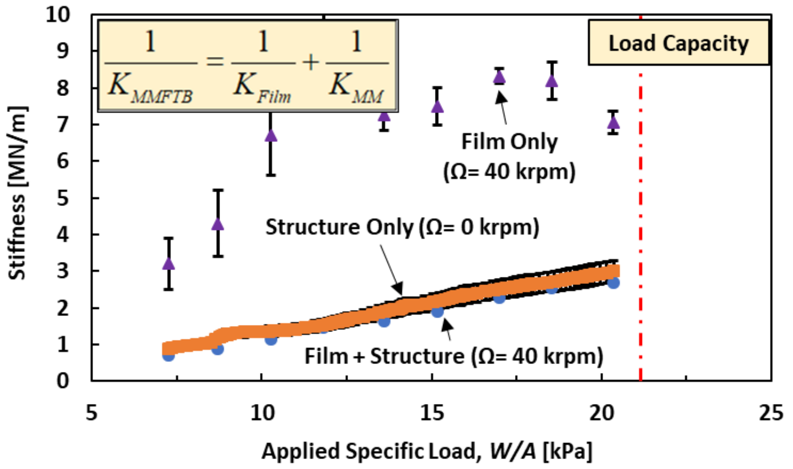

(b) Derived film, mesh structural, and full bearing stiffnesses

Figure 40. (a) Applied specific load versus bearing displacement and (b) Approximated stiffnesses versus specific load. Ω = 40 krpm.

Figure 41 (a) & (b) compare mesh underspring stiffness (K_{MM}) as well as bearing stiffness (K_{MMFTB}) versus applied load (W/A) for the single-pad and six-pad MMFTB operating at Ω = 40 krpm. Note that the Figure displays K_{MM} and K_{MMFTB} for load comprised between $7.5 \leq W/A \leq 22.5$ kPa, the largest load being just under the measured load capacity of the six-pad MMFTB ($W/A = 25$ kPa). In addition, and for comparative purposes, both plots contain the single pad data (either K_{MM} or K_{MMFTB}) multiplied by six. Results in Figure 41 (a) show the mesh undersprings for the two bearings to be similar at low loads ($W/A < 15$ kPa), yet as the load continues to increase, the single pad bearing (multiplied by 6) is noticeably stiffer. Figure 41 (b) shows that the full bearing stiffness (K_{MMFTB}) follows the same trend.

Conventional wisdom indicates that the bearing stiffness increases linearly with the number of bearing pads; however, manufacturing and assembly differences between the six undersprings can cause a non-uniform stiffness (and hence loading) distribution along the bearing. As indicated by non-uniform pad temperatures (Figure 39), the results in Figure 41 show that not all six pads are identical, and some may only mildly contribute to the bearing load capacity (and stiffness).

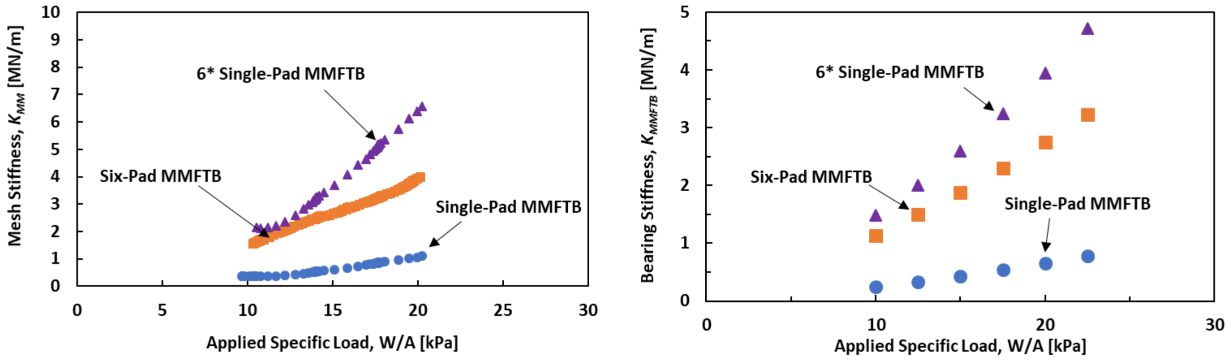

(a) K_{MM} versus applied specific load

(b) K_{MMFTB} versus applied specific load

Figure 41. (a) Metal mesh and (b) assembled bearing stiffness versus applied specific load for a single-pad and a six-pad circumferentially tapered MMFTB. Ω = 40 krpm.

Figure 42 displays the steady-state bearing drag torque and a friction factor, $f = T/(F \cdot R_{mid})$, versus applied specific load for the broken-in six-pad MMFTB as well as for a similar size BFTB (Stahl [19]), both operating with Ω = 40 krpm. Despite applying cooling flow (300 SLPM) to the MMFTB, the drag torque for the MMFTB is approximately 3-4 times larger than that of the similarly sized BFTB [19]. The BFTB does have $A = 46$ cm^2, while the MMFTB has $A = 56$ cm^2; however, this change in bearing area is not likely to cause a more than 300% increase in drag torque from one bearing type to the next. To illustrate the point further, comparing the friction coefficient for the two bearings shows the BFTB has a friction coefficient similar to other gas bearings in the literature [4,19], while the friction factor for the MMFTB is approximately 2-4 times larger than other gas bearings.

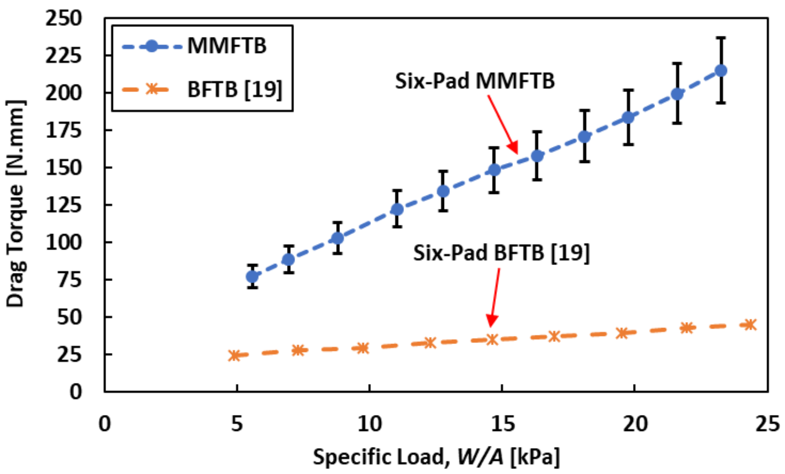

(a) Drag torque versus specific load

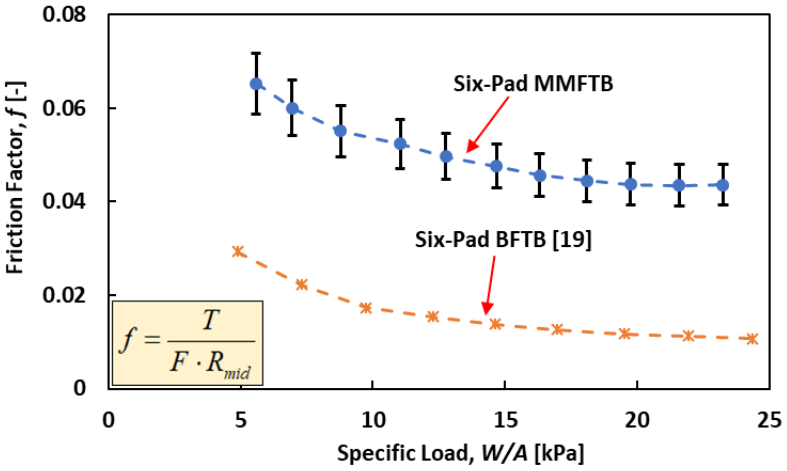

(b) Friction factor versus specific load

Figure 42. Bearing drag torque versus specific load for a broken-in six-pad MMFTB and a similar sized BFTB from Stahl [19]. Ω = 40 krpm.

As with the single-pad MMFTB, post-test condition of the rotor collar confirmed the presence of MoS_2 deposits on its surface. Presumably, this debris along with an uneven load distribution on the MMFTB pads (as indicated by the temperature profiles in the previous figures) increased the MMFTB drag torque and friction factor beyond what is typical for gas lubricated bearings.

During subsequent testing with the six-pad MMFTB, the test rig experienced a failure, where the rotating thrust collar decoupled from the router motor collet. The motor and collar assembly operated above its first natural frequency during testing, having a first (observed) critical speed at ~15 krpm. Traversing this critical speed with a heavy and overhung collar assembly eventually shook the thrust collar free during testing and damaged the motor shaft (and bearings).

The rotation guard (displayed in Figure 8) contained the spinning collar and prevented serious damage to the test MMFTB and instrumentation; however, the collar itself was severally gouged on its outer diameter out of round (runout on the OD of more than 0.005”). In addition to the collar, a post-failure inspection of the electric motor found the motor armature and ceramic angular contact bearings to damaged. Remedial action included chrome-plating and rebalancing the armature and outfitting the refurbished motor with new ceramic angular contact ball bearings (with a higher dynamic load rating). This failure highlights a poor initial design of the rig, coupling the heavy steel collar directly to the router motor via a simple collet and collet nut. Appendix A provides a design of an intermediate housing between the electric motor and thrust collar.

Despite difficulties encountered with the prototype circumferentially tapered MMFTB, do recall that the bearing is a prototype, hand-constructed and not precision machined or assembled. The data in this chapter is a first step, which shows that a compliant surface gas foil thrust bearing with wire screen as the support structure does support a load, albeit small. While not refined, nor fully searched out, the concept is established and available for others to build upon.

6. A THERMO-ELASTOHYDRODYNAMIC MODEL FOR A CIRCUMFERENTIALLY TAPERED METAL MESH FOIL THRUST BEARING

Despite difficulties with the prototype bearings (described in the previous sections), metal mesh screen as an alternative to bump foils in compliant surface thrust bearings should be analyzed at a theoretical level to asses any potential gains for a well-built bearing. The following section presents a model[7] aimed at elucidating (and somewhat simplifying) the physics for a MMFTB operating with ambient air as the lubricant. A steady-state compressible Reynolds equation with first-order slip boundary conditions and a two-dimensional thermal energy transport equation determine both the film pressure and the temperature fields, respectively. The model couples the elastic deformations of the top foil and mesh structure to the hydrodynamic pressure in the thin film and handles thermal energy transport with the surrounding environment via conduction through the bounding solids and convection with atmosphere and cooling flows. Refs. [42-46] show that thermally induced bending of the thrust collar significantly affects the bearing film thickness and load capacity for surface speeds in excess of $R_{mid}\cdot\omega > 200$ m/s. As the current experimental setup has a thrust collar with a fairly constant temperature throughout its thickness (cooling flow applied to the front face, with the back surface open to atmosphere) and $R_{mid}\cdot\omega = 160$ m/s (maximum), the current model does not include thermal deformations the of thrust collar[8].

---

[7] The current model extends an isothermal model for bump-type foil thrust bearings [4] for MMFTBs while also including thermal effects in the thin film and bounding solids.

[8] Predicted rotor collar temperatures (displayed later) for the current experiments show a too small temperature gradient from the rotor center to the OD to induce thermal bending.

6.1 HYDRODYNAMIC PRESSURE

Figure 43 displays a two-dimensional schematic of a single bearing pad circumferentially tapered MMFTB, including parameters and a coordinate system for the following analysis. Once a gas film separates the thrust collar from the thin top foil, the film thickness is piecewise and equals to

$$h(r,\theta)=\begin{cases} h_e+\left(1-\dfrac{\theta}{\theta_t}\right)t_{MM}+w_{(r,\theta)} & , \quad 0\le\theta\le\theta_t \\ h_e+w_{(r,\theta)} & , \theta_t<\theta\le\theta_p \end{cases} \tag{12}$$

where $w_{(r,\theta)}$ refers to the local elastic deformations of the top foil and underspring structure and h_e is the exit film thickness.

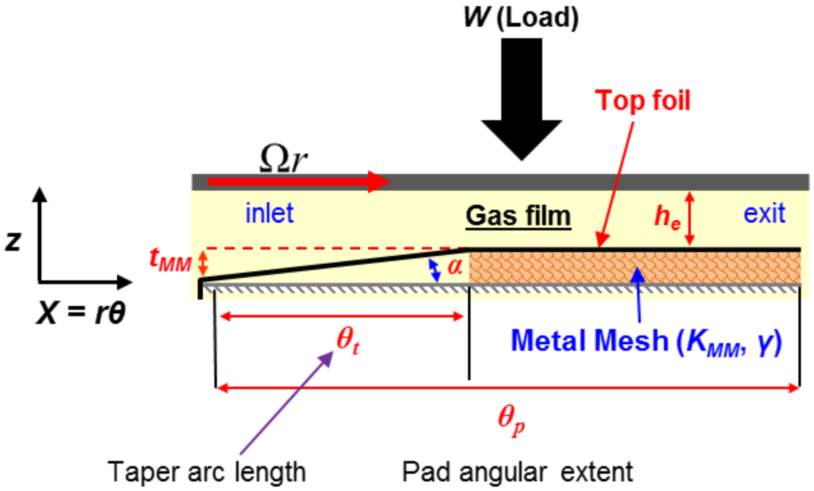

Figure 43. Schematic of a single metal mesh pad and coordinates for analysis.

The vector form of the momentum equation (neglecting body forces) for the laminar[9] flow of a compressible, Newtonian fluid with an averaged cross-film viscosity (μ_f)[10] is

$$\frac{D}{Dt}\left(\rho\vec{U}\right) = -\vec{\nabla}P + \mu_f \Delta\vec{U} + \frac{1}{3}\mu_f \vec{\nabla}\left(\vec{\nabla}\cdot\vec{U}\right) \tag{13}$$

In thin film lubrication, the length scales ($R_o\theta >> h$, R_o-$R_i >> h$) dictate that only the first order velocity gradients across the film thickness ($\partial U_{r,\theta,z} / \partial z$) are of importance. With the lubrication assumption, the momentum equations reduce to

$$\begin{gathered}\frac{\partial P}{\partial r} = \mu_f \frac{\partial^2 U_r}{\partial z^2} \\ \frac{1}{r}\frac{\partial P}{\partial \theta} = \mu_f \frac{\partial^2 U_\theta}{\partial z^2} \\ \frac{\partial P}{\partial z} = 0\end{gathered} \tag{14}$$

Integration of the momentum equations across the film thickness, and application of first-order slip boundary conditions (BCs) at the foil and thrust collar surfaces [16],

$$\begin{gathered}U_{r(r,\theta,z=0)} = \lambda\left[\frac{\partial U_r}{\partial z}\right]_{z=0},\ U_{r(r,\theta,z=h)} = -\lambda\left[\frac{\partial U_r}{\partial z}\right]_{z=h} \\ U_{\theta(r,\theta,z=0)} = \lambda\left[\frac{\partial U_\theta}{\partial z}\right]_{z=0},\ U_{\theta(r,\theta,z=h)} = r\Omega - \lambda\left[\frac{\partial U_\theta}{\partial z}\right]_{z=h}\end{gathered} \tag{15}$$

gives the fluid film velocity profiles

$$U_r = \frac{1}{2\mu_T}\frac{\partial P}{\partial r}\left(z^2 - zh - \lambda h\right),\ U_\theta = \frac{1}{2\mu_T}\frac{1}{r}\frac{\partial P}{\partial \theta}\left(z^2 - zh - \lambda h\right) + r\Omega\left(\frac{z+\lambda}{h+2\lambda}\right) \tag{16}$$

where the molecular mean free path and Knudsen number are[11] [16]

---

[9] A MMFTB operating with air at ambient conditions (ρ = 1.225 kg/m^3, μ = 18.22·10^{-6} Pa.s) and having a maximum film thickness of ~35 μm and a surface speed (ωR_o = 4,189 m/s · 0.0508 m) of 212 m/s has a shear flow Reynolds number $\mathrm{Re} = \left\{\rho\left(\Omega R_o\right)h\right\}/\mu \sim 500$, denoting operation well within the laminar flow regime (Re ≤ 2,300).

[10] Note that in the following analysis the subscript "*f*" denotes a parameter evaluated at the cross-film averaged temperature.

[11] m_{gas} ~ 0.029 kg/mol for dry air at standard conditions.

$$\lambda = \frac{\mu}{P}\sqrt{\frac{\pi k_B T}{2m_{gas}}} \quad \rightarrow \quad \mathrm{Kn} = \frac{\lambda}{h} \tag{17}$$

Also note that the axial velocity of the fluid attached to the foil and thrust collar surfaces is

$$\begin{aligned} U_{z(r,\theta,z=0)} &= 0 \\ U_{z(r,\theta,z=h)} &= \frac{\partial h}{\partial t} + \left(U_r\right)_h \frac{\partial h}{\partial r} + \left(U_\theta\right)_h \frac{\partial h}{r\partial\theta} \end{aligned} \tag{18}$$

where the radial and circumferential velocities at the runner surface ($U_{r,h}$ and $U_{\theta,h}$) are as defined in Eq. (15) above.

In Eq. (17), m_{gas} is the molecular mass of the gas, k_B is Boltzmann's constant, and μ, P, T are the gas dynamic viscosity, pressure and temperature, respectively. Flows with very low Knudsen numbers (Kn < 0.01) can be considered as continuums, with appropriate non-slip boundary conditions at fluid-solid interfaces. As the mean free path approaches the magnitude of the flow domain characteristic length (0.01 ≤ Kn ≤ 15), collisions between molecules become less frequent and the fluid molecules themselves begin to slip at a fluid-solid interface. For large Knudsen numbers (Kn > 15) the flow can no longer be considered a continuum, since collisions between particles rarely occur.

Integration of Eqs. (16) across the film thickness (0→h) yields the mass flow rates flow rates (per unit length) [16]

$$\begin{aligned} \dot{m}_r &= \rho_f \int_0^h U_r dz = \rho_f h \bar{U}_r = -\frac{\rho_f h^3}{12\mu_f}\frac{\partial P}{\partial r}\left\{1+6\ \mathrm{Kn}\right\} \\ \dot{m}_\theta &= \rho_f \int_0^h U_\theta dz = \rho_f h \bar{U}_\theta = -\frac{\rho_f h^3}{12\mu_f}\frac{1}{r}\frac{\partial P}{\partial \theta}\left\{1+6\ \mathrm{Kn}\right\} + \left(r\Omega\right)\frac{\rho_f h}{2} \end{aligned} \tag{19}$$

Substituting the mass flow rates into the continuity equation (also integrated across the film thickness) renders a Reynolds equation for the MMFTB as

$$\frac{1}{r}\frac{\partial}{\partial r}\left[r\frac{\rho_f h^3}{12\mu_f}\{1+6\ \mathrm{Kn}\}\frac{\partial P}{\partial r}\right]+\frac{1}{r}\frac{\partial}{\partial \theta}\left\{\frac{\rho_f h^3}{12\mu_f}\{1+6\ \mathrm{Kn}\}\frac{\partial P}{r\partial \theta}\right\}=\frac{\partial}{\partial t}\left\{\rho_f h\right\}+\frac{1}{r}\frac{\partial}{\partial \theta}\left\{r\Omega\rho_f\left(\frac{h}{2}\right)\right\} \tag{20}$$

where *h* is the film thickness, and ρ_f and μ_f are the lubricant density and viscosity (evaluated at the average cross-film temperature), respectively. For an ideal gas, such as air, the lubricant density relates to the gas pressure and temperature as

$$\rho_f = \frac{P}{R_g Z_g T_f} \tag{21}$$

and for steady state conditions, the laminar flow Reynolds equation for an ideal gas with first-order slip BCs simplifies to

$$\frac{\partial}{\partial r}\left[r\frac{\rho_f h^3}{\mu_T}\frac{\partial P}{\partial r}\left\{1+6\ \mathrm{Kn}_f\right\}\right]+\frac{\partial}{\partial \theta}\left\{\frac{\rho_f h^3}{\mu_T}\frac{\partial P}{r\partial \theta}\left\{1+6\ \mathrm{Kn}_f\right\}\right\}=6r\Omega\frac{\partial}{\partial \theta}\left\{\frac{Ph}{T_f}\right\} \tag{22}$$

In Eq. (22), the lubricant density (ρ_f) remains in the left-hand side to avoid a nonlinear algebraic equation (in *P*) once discretized. As the MMFTB utilizes ambient air as the working lubricant, second order polynomial fits of tabulated data in Ref. [62] determine the temperature dependent dynamic viscosity, thermal conductivity and specific heat at constant pressure as

$$\begin{aligned}
\mu_f\left(T_f\right) &= -1.48\cdot 10^{-11}T_f^2+5.20\cdot 10^{-8}T_f+4.33\cdot 10^{-6}\quad [\mathrm{Pa.s}]\\
\kappa_f\left(T_f\right) &= -2.03\cdot 10^{-8}T_f^2+8.54\cdot 10^{-5}T_f+1.86\cdot 10^{-3}\quad \left[\mathrm{W/}\left(\mathrm{m}\cdot\mathrm{K}\right)\right]\\
c_p\left(T_f\right) &= 1.18\cdot 10^{-4}T_f^2+5.07\cdot 10^{-2}T_f+978\quad \left[\mathrm{kJ/}\left(\mathrm{kg}\cdot\mathrm{K}\right)\right]
\end{aligned} \tag{23}$$

where T_f is the absolute [K] air film temperature.

6.2 TOP FOIL ELASTIC DEFORMATION

Figure 44 displays a schematic of a single top foil supported by a flexible mesh substructure. The figure includes a discretization of the top foil as well as an enlarged view of a single finite element (FE) in the domain, indicating pressure and reaction forces on its surfaces. The top foil fixes to the bearing support at the leading edge and is free to rotate at the three other edges.

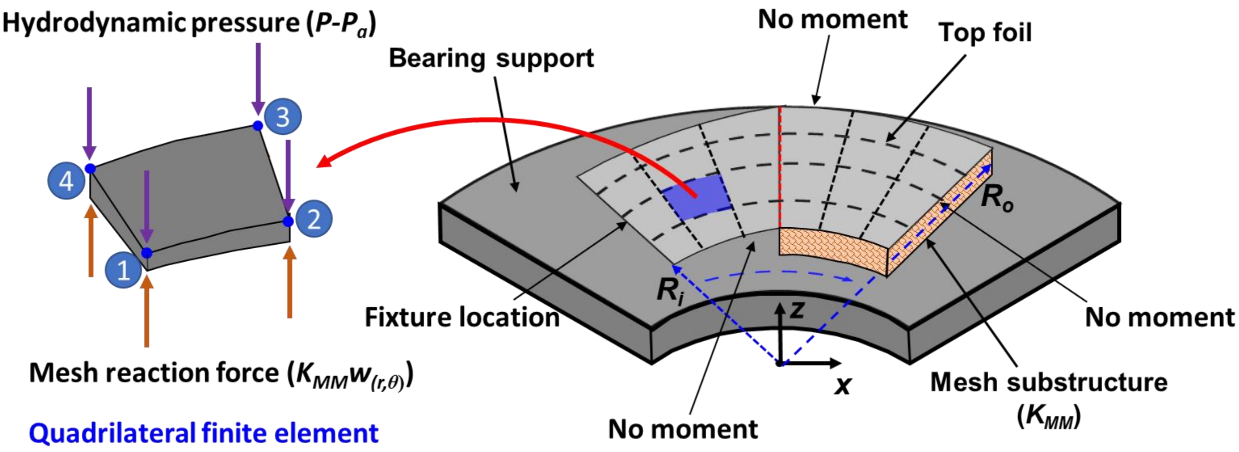

Figure 44. Schematic view of a single top foil supported by a flexible mesh structure and a finite element indicating pressure and mesh reaction forces at its nodes.

As in Ref. [62], the top foil is modeled as a two-dimensional shell supported by a flexible substructure having a uniform stiffness per unit area (K_{MM}). The elastic deformation of the thin top foil ($w_{(r,\theta)}$) is governed by first-order shear deformable plate theory (FSDT) while the deformation of the mesh substructure depends on an empirically determined K_{MM}. For steady state conditions ($\partial / \partial t = 0$), the differential equations of FSDT are [61]

$$\begin{gathered}\frac{\partial Q_X}{\partial X}+\frac{\partial Q_Y}{\partial Y}-\left(P-P_a\right)+K_{MM}\,w=0\\ \frac{\partial M_X}{\partial X}+\frac{\partial M_{YX}}{\partial Y}-Q_X=0\\ \frac{\partial M_{YX}}{\partial X}+\frac{\partial M_Y}{\partial Y}-Q_Y=0\end{gathered} \tag{24}$$

where $Q_{X,Y}$ are shear forces and $M_{X,Y}$ are bending moments, defined as

$$Q_X = A_{55}\left(\varphi_X + \frac{\partial w}{\partial x}\right); Q_Y = A_{44}\left(\varphi_Y + \frac{\partial w}{\partial Y}\right)$$
$$M_X = D_{11}\frac{\partial \varphi_X}{\partial X} + D_{12}\frac{\partial \varphi_Y}{\partial Y}; M_Y = D_{12}\frac{\partial \varphi_X}{\partial X} + D_{22}\frac{\partial \varphi_Y}{\partial Y}; M_{XY} = D_{66}\left(\frac{\partial \varphi_X}{\partial Y} + \frac{\partial \varphi_Y}{\partial X}\right) \tag{25}$$

In Eq. (25), the plate rigidities D_{ij} and transverse shear strains A_{ij} follow from the plate's material properties (E, ν) and thickness (t_{tf}), i.e.

$$A_{44} = k_t \frac{E_{23} t_{tf}}{2(1-\nu_{23})}\ ; A_{55} = k_t \frac{E_1 t_{tf}}{2(1-\nu_{13})}$$
$$D_{11} = \frac{E_1 t_{tf}^3}{12(1-\nu_{12}\nu_{21})}; D_{12} = \frac{\nu_{12} E_2 t_{tf}^3}{12(1-\nu_{12}\nu_{21})}; D_{22} = \frac{E_2 t_{tf}^3}{12(1-\nu_{12}\nu_{21})}; D_{66} = \frac{E_{12} t_{tf}^3}{24(1-\nu_{12}\nu_{21})} \tag{26}$$

Do note that in-plane (i.e. membrane) forces are neglected in the current model.

6.3 THERMAL ENERGY TRANSPORT IN THE THIN FILM

As noted in Chapter 2, Refs. [41-46] consider a full three-dimensional thermal energy transport equation in the fluid film; however, a more complex model adds computational time. In the case of Ref. [45], utilizing commercial software to solve the coupled fluid, structural and thermal governing equations for a complaint surface foil thrust bearing, the computation time exceeded 10 days. While Refs. [41,42] do not specify the computational times required for the authors' schemes, they are no doubt, extensive. The current model serves as a quick engineering analysis of the current situation, including the physics necessary for an accurate solution, while still being expedient.

Figure 45 displays a two-dimensional (2D) schematic view of the heat transfer in a MMFTB. During operation, lubricant shear and pressure extrusion generate heat (represented as the heat source in the air film). A portion of this heat conducts through the collar ($\dot{q}_{TC}$) and top foil ($\dot{q}_{tf}$).

The model assumes that the heat flux from the bottom side of the top foil conducts through the metal mesh or is carried away by a cooling flow stream (with temperature T_{cf}). Heat is expelled to ambient through its outer diameter and the back side of the collar. Table 8 summarizes the various heat transfer mechanisms in the domain. It is important to note that Appendix B gives details on the various heat transfer coefficients ($\overline{h}$, κ) listed in the following sections.

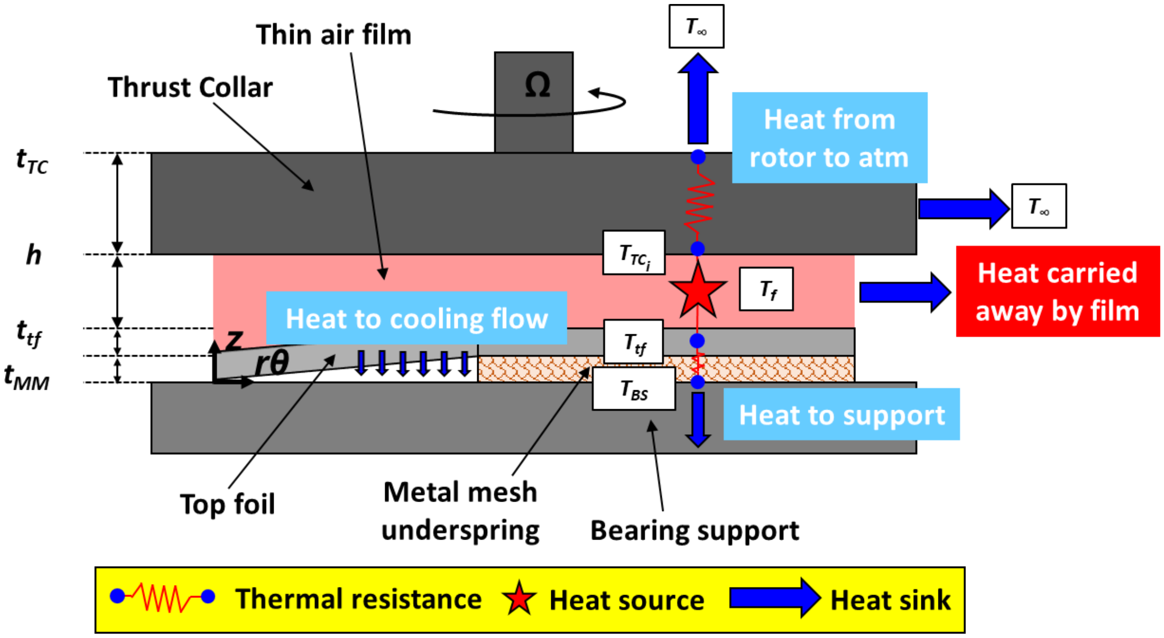

Figure 45. Schematic of the heat transfer in a MMFTB.

Table 8. Summary of heat fluxes as in San Andrés *et al.* [36].

Heat flux [W/(m^2.K)]	Description
$\dot{q}_{F\_TC} = \bar{h}_{F\_TC}\left(T_f - T_{TC}\right)$	Heat convected from film to thrust collar
$\dot{q}_{OD\_atm} = \bar{h}_{OD\_atm}\left(T_\infty - T_{TC}\right)$	Heat convected from thrust collar OD to atmosphere
$\dot{q}_{TC\_back} = \bar{h}_{TC}\left(T_\infty - T_{TC}\right)$	Heat convected from thrust collar surface to atmosphere or the internal cavity
$\dot{q}_{F\_tf} = \bar{h}_{F\_tf}\left(T_f - T_{tf}\right)$	Heat convected from film to top foil
$\dot{q}_{tf\_BS} = \dfrac{1}{R_{MM}}\left(T_{tf} - T_{BS}\right)$	Heat conducted through metal mesh and bearing support
$\dot{q}_{tf\_atm} = \bar{h}_{tf\_atm}\left(T_{cf} - T_{tf}\right)$	Heat convected from back side of top foil to air (either cooling or stagnant) in tapered portion

The energy equation governs the temperature of the thin film between the thrust collar and top foil [30], and in a conservation form is

$$\frac{\partial}{\partial t}\left(\rho c_p T\right) + \vec{\nabla}\cdot\left(\rho c_p T\vec{U}\right) = -P\vec{\nabla}\cdot\vec{U} + \vec{\nabla}\left(\kappa\vec{\nabla}T\right) + \mu\Phi \tag{27}$$

where κ is the lubricant thermal conductivity, c_p is the specific heat at constant pressure and Φ is the viscous dissipation function. For steady state conditions ($\partial/\partial t = 0$),

$$\begin{gathered}\left\{\frac{1}{r}\frac{\partial}{\partial r}\left(r\rho c_p T U_r\right) + \frac{1}{r}\frac{\partial}{\partial \theta}\left(\rho c_p T U_\theta\right) + \frac{\partial}{\partial z}\left(\rho c_p T U_z\right)\right\} = \\ \kappa\left\{\frac{1}{r}\frac{\partial}{\partial r}\left(r\frac{\partial T}{\partial r}\right) + \frac{1}{r^2}\frac{\partial^2 T}{\partial \theta^2} + \frac{\partial^2 T}{\partial z^2}\right\} + \beta_t T\left\{U_r\frac{\partial P}{\partial r} + \frac{U_\theta}{r}\frac{\partial P}{\partial \theta} + U_z\frac{\partial P}{\partial z}\right\} + \mu\Phi\end{gathered} \tag{28}$$

In Eq. (28), β_t is the fluid's volumetric expansion coefficient and the viscous dissipation function (Φ) in cylindrical coordinates is [30]

$$\begin{aligned}\Phi = 2&\left[\left(\frac{\partial U_r}{\partial r}\right)^2 + \left\{\frac{1}{r}\left(\frac{\partial U_\theta}{\partial \theta}+U_r\right)\right\}^2 + \left(\frac{\partial U_z}{\partial z}\right)^2\right] + \left(\frac{\partial U_\theta}{\partial z}+\frac{1}{r}\frac{\partial U_z}{\partial \theta}\right)^2 + \left(\frac{\partial U_z}{\partial r}+\frac{\partial U_r}{\partial z}\right)^2 \\ &+\left(\frac{1}{r}\frac{\partial U_r}{\partial \theta}+r\frac{\partial}{\partial r}\left(\frac{U_\theta}{r}\right)\right)^2 - \frac{2}{3}\left[\frac{1}{r}\frac{\partial}{\partial r}\left(rU_r\right)+\frac{1}{r}\frac{\partial}{\partial \theta}\left(U_\theta\right)+\frac{\partial}{\partial z}\left(U_z\right)\right]^2\end{aligned} \tag{29}$$

Ref. [31] states that only first order velocity gradients and second order temperature gradients across the film thickness ($\partial U_{r,\theta,z} / \partial z, \partial^2 T / \partial z^2$) are of importance. In addition, for an ideal gas, the product $\beta_t T = 1$ [31,65]. With these assumptions, Eq. (25) reduces to

$$\begin{aligned}&\left\{\frac{1}{r}\frac{\partial}{\partial r}\left(r\rho c_p T U_r\right)+\frac{1}{r}\frac{\partial}{\partial \theta}\left(\rho c_p T U_\theta\right)+\frac{\partial}{\partial z}\left(\rho c_p T U_z\right)\right\} = \\ &\kappa_F\,\frac{\partial^2 T}{\partial z^2}+\left\{U_r\frac{\partial P}{\partial r}+\frac{U_\theta}{r}\frac{\partial P}{\partial \theta}\right\}+\mu_T\left\{\left(\frac{\partial U_r}{\partial z}\right)^2+\left(\frac{\partial U_\theta}{\partial z}\right)^2\right\}\end{aligned} \tag{30}$$

Integration of Eq. (29) across the film thickness utilizes Leibniz integration formula [31]. Eq. (31) displays the integrals of each term from Eq. (30).

$$\begin{aligned}\int_0^h\left\{\frac{1}{r}\frac{\partial}{\partial r}\left(r\rho c_p T U_r\right)\right\}dz &= \frac{1}{r}\left[\frac{\partial}{\partial r}\left\{\int_0^h\left(r\rho c_p T U_r\right)dz\right\}+\left(r\rho c_p T U_r\right)_h\frac{\partial h}{\partial r}\right] \\ \int_0^h\frac{\partial}{r\partial \theta}\left(\rho c_p T U_\theta\right)dz &= \left[\frac{\partial}{r\partial \theta}\left\{\int_0^h\left(\rho c_p T U_\theta\right)dz\right\}+\left(\rho c_p T U_\theta\right)_h\frac{\partial h}{r\partial \theta}\right] \\ \int_0^h\frac{\partial}{\partial z}\left(\rho c_p T U_z\right)dz &= \left(\rho c_p T U_z\right)_h-\left(\rho c_p T U_z\right)_0 \\ \int_0^h\left(\kappa\frac{\partial^2 T}{\partial z^2}\right)dz &= \left(\kappa\frac{\partial T}{\partial z}\right)_h-\left(\kappa\frac{\partial T}{\partial z}\right)_0 \\ \int_0^h\left(U_r\frac{\partial P}{\partial r}+\frac{U_\theta}{r}\frac{\partial P}{\partial \theta}\right)dz &= \frac{\partial P}{\partial r}\int_0^h\left(U_r\right)dz+\frac{1}{r}\frac{\partial P}{\partial \theta}\int_0^h\left(U_\theta\right)dz \\ \int_0^h\left(\mu_T\left\{\left(\frac{\partial U_r}{\partial z}\right)^2+\left(\frac{\partial U_\theta}{\partial z}\right)^2\right\}\right)dz &= \frac{h^3}{12\mu_t}\left\{\left(\frac{\partial P}{\partial r}\right)^2+\left(\frac{\partial P}{r\partial \theta}\right)^2\right\}+\frac{\mu_T\left(r\Omega\right)^2}{h}\end{aligned} \tag{31}$$

For simplicity, consider an average cross-film temperature (T_f) and properties evaluated at this average temperature (ρ_f, μ_f, c_{p_f} and λ_f), such that the radial and circumferential advection terms take the form

$$\begin{aligned}\int_0^h \left(r\rho c_p T U_r\right) dz &\approx r\rho_f c_{p_f} T_f \int_0^h \left(U_r\right) dz = r c_{p_f} T_f \rho_f h \bar{U}_r = r c_{p_f} T_f \dot{m}_r \\ \int_0^h \left(\rho c_p T U_\theta\right) dz &\approx \rho_f c_{p_f} T_f \int_0^h \left(U_\theta\right) dz = c_{p_f} T_f \rho_f h \bar{U}_\theta = c_{p_f} T_f \dot{m}_\theta\end{aligned} \tag{32}$$

With the simplifications from Eq. (32), and the definitions of the lubricant mass flows (Eq. 19), integrating Eq. (30) across the film thickness yields

$$\begin{gathered}\frac{1}{r}\frac{\partial}{\partial r}\left(r c_p T_f \dot{m}_r\right) - \left(r\rho c_p T U_r\right)_h \frac{\partial h}{\partial r} + \frac{1}{r}\frac{\partial}{\partial \theta}\left(c_p T_f \dot{m}_\theta\right) - \left(\rho c_p T U_\theta\right)_h \frac{\partial h}{r\partial \theta} + \left(\rho c_p T U_z\right)_h - \left(\rho c_p T U_z\right)_0 = \\ \kappa\left[\left(\frac{\partial T}{\partial z}\right)_h - \left(\frac{\partial T}{\partial z}\right)_0\right] + h\left[\bar{U}_r \frac{\partial P}{\partial r} + \frac{\bar{U}_\theta}{r}\frac{\partial P}{\partial \theta}\right] + \frac{h^3}{12\mu}\left[\left(\frac{\partial P}{\partial r}\right)^2 + \left(\frac{\partial P}{r\partial \theta}\right)^2\right] + \mu\frac{\left(r\Omega\right)^2}{h\left(1+2\ \mathrm{Kn}\right)^2}\end{gathered} \tag{33}$$

where again, $\dot{m}_{r,\theta} = \rho h \bar{U}_{r,\theta}$. Application of the boundary conditions from Eq. (15) simplifies Eq. (33) to the form [16]

$$\begin{gathered}\frac{1}{r}\frac{\partial}{\partial r}\left(r c_p T_f \dot{m}_r\right) + \frac{1}{r}\frac{\partial}{\partial \theta}\left(c_p T_f \dot{m}_\theta\right) = Q_s + h\left[\bar{U}_r \frac{\partial P}{\partial r} + \frac{\bar{U}_\theta}{r}\frac{\partial P}{\partial \theta}\right] + \frac{h^3}{12\mu}\left[\left(\frac{\partial P}{\partial r}\right)^2 + \left(\frac{\partial P}{r\partial \theta}\right)^2\right] \\ +\mu\frac{\left(r\Omega\right)^2}{h\left(1+2\ \mathrm{Kn}\right)^2}\end{gathered} \tag{34}$$

where the heat flow between the film and the bounding solids (Q_s) is

$$Q_s = \dot{q}_{f\_TC} + \dot{q}_{f\_tf} = \left[\kappa\frac{\partial T}{\partial z}\right]_0^h \approx \bar{h}_{TC}\left(T_{TC} - T_f\right) + \bar{h}_{tf}\left(T_{tf} - T_f\right) \tag{35}$$

and $\bar{h}_{TC}, \bar{h}_{tf}$ are heat convection coefficients towards the thrust collar and top foil surfaces[12].

In Eq. (34) the Knudsen number appears explicitly only in the shear flow term, however, do recall that the fluid mean flow velocities ($\bar{U}_r, \bar{U}_\theta$) include gas rarefaction through first-order slip flow BCs (Eq. 19). For flows where the molecular mean free path far exceeds the local film

---

[12] Note that the heat transfer coefficients in Eq. (34) consider the fluid near the bounding surfaces as a continuum, and do not consider the effects of gas rarefaction.

thickness (i.e. Kn ~ 0), the shear flow term as well as the mean flow velocities simplify the thermal energy transport equation to a more familiar form.

6.4 THERMAL ENERGY TRANSPORT TO THE BOUNDING SOLIDS

Figure 46 displays a schematic view of the heat transfer between a thin top foil, the lubricating air film, metal mesh substructure and atmosphere. As described in Figure 45 and Table 8, heat convects from the air film to the top foil, passing through its thickness and into the metal mesh underspring or convecting to cooling flow in the tapered portion. Note that conduction through the foil itself as well as convection from the foil edges to atmosphere are neglected due to the length scales ($t_{tf} << R_o - R_i, \Theta_P R_{mid}$).

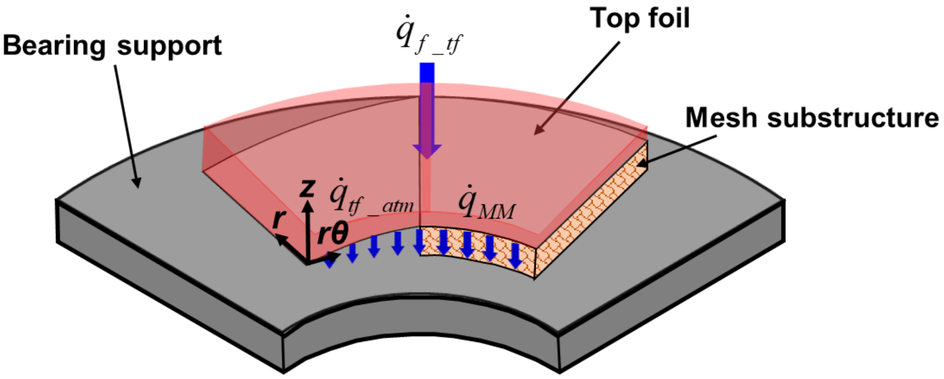

Figure 46. Heat transfer between a thin top foil and its surroundings.

The balance of thermal energy (per unit volume) for the top foil involves radial and circumferential conduction in the foil as well as appropriate heat transfer with the surroundings, i.e.

$$\kappa_{tf}\left[\frac{\partial^2 T_{tf}}{\partial r^2}+\frac{1}{r}\frac{\partial T_{tf}}{\partial r}+\frac{1}{r^2}\frac{\partial^2 T_{tf}}{\partial \theta^2}\right]+\frac{1}{t_{tf}}\left[\dot{q}_{f\_tf}+\dot{q}_{tf\_back}\right]=0 \tag{36}$$

As displayed in Table 8, the heat flux between the air film to the top foil ($\dot{q}_{f\_tf}$) is

$$\dot{q}_{f\_tf}=\bar{h}_{f\_tf}\left(T_f-T_{tf}\right) \tag{37}$$

There is both (one dimensional) conduction through the thickness of the mesh layers and to the back surface of the bearing support (maintained at a constant temperature T_{BS}) as well as convection between the back of the foil and cooling flow supplied at a set temperature (T_{cf}) in the tapered section of the foil. Thus, the heat flux from the back of the top foil is

$$\dot{q}_{tf\_back}=\begin{cases}\dot{q}_{tf\_BS}=\left(\dfrac{t_{MM}}{\kappa_{MM}}+\dfrac{t_{BS}}{\kappa_{BS}}\right)^{-1}\left(T_{BS}-T_{tf}\right) & , \quad 0\le\theta\le\theta_t \\ \dot{q}_{tf\_cf}=\bar{h}_{tf\_cf}\left(T_{cf}-T_{tf}\right) & , \quad \theta_t\le\theta\le\theta_P\end{cases} \tag{38}$$

where the first term in Eq. (38) utilizes an effective thermal conductivity for metal mesh layers and $\bar{h}_{tf\_cf}$ is determined with the Nusselt number for flow through a triangular duct[13]. When no cooling flow is applied to the bearing, heat transfer between the top foil and ambient occurs via natural convection, with a heat transfer coefficient $\bar{h}_{tf\_cf}\approx 10\ \left[\mathrm{W}/\left(\mathrm{m}^2\mathrm{K}\right)\right]$ [36].

Figure 47 depicts the heat transfer from the thin film into the thrust collar, and from the collar to atmosphere. For an axisymmetric collar and bearing, and for steady state operating conditions ($\partial\Omega/\partial t=0$), the collar temperature at a given radius does not vary significantly in the circumferential direction ($\partial T/\partial\theta=0$) [41,45]. In addition, for high rotor speeds and a steady-state analysis, a material point in the thrust collar is stationary when seen from a fixed coordinate system at the thrust collar center.

---

[13] See Appendix B for more details.

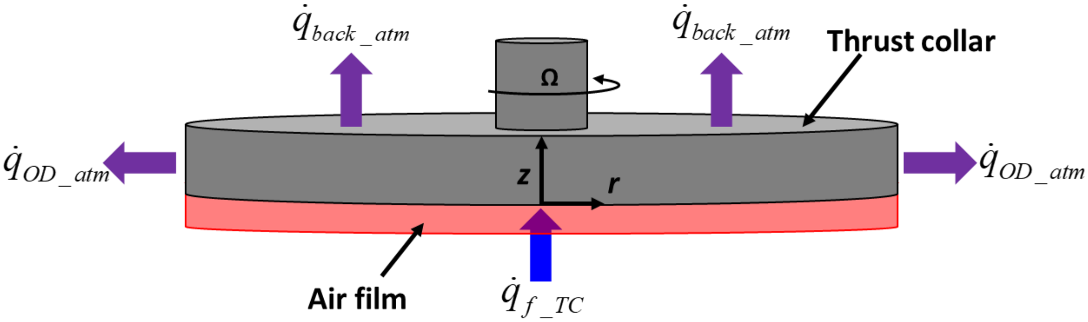

Figure 47. Heat transfer between a rotating thrust collar and its surroundings.

With these assumptions, the thrust collar temperature follows from

$$\kappa_{TC}\left[\frac{\partial^2 T_{TC}}{\partial r^2}+\frac{1}{r}\frac{\partial T_{TC}}{\partial r}+\frac{\partial^2 T_{TC}}{\partial z^2}\right]+\frac{1}{t_{TC}}\left[\dot{q}_{TC\_atm}+\dot{q}_{OD\_atm}+\dot{q}_{f\_TC}\right]=0 \tag{39}$$

The heat input (per unit area) to the thrust collar face from the thin film is determined by

$$\dot{q}_{f\_TC}=\left\{\sum \bar{h}_{TC}\left(T_f-T_{TC}\right)\right\}n_{pad} \tag{40}$$

where T_{TC} is the thrust collar temperature on the surface exposed to the gas film. Note that the summation in Eq. (40) takes into consideration the contribution of every CV on a constant radius, extending from 0 - 2π.

Refs. [41, 45] give heat transfer coefficients for a rotating cylinder in an infinite quiescent medium maintained at temperature T_∞ as

$$\begin{aligned}\dot{q}_{back\_atm}&=\bar{h}_{TC}\left(T_\infty-T_{TC}\right)\\ \dot{q}_{OD\_atm}&=\bar{h}_{OD\_atm}\left(T_\infty-T_{TC}\right)\end{aligned} \tag{41}$$

In Eq. (41) $\bar{h}_{TC}$ is a heat transfer determined with the rotational Reynolds number and Prandtl number of the air at T_∞. Appendix B gives details on the forms of the heat transfer coefficients.

6.5 HANDLING OF COOLING FLOW AND THERMAL MIXING BETWEEN PADS

A MMFTB is a hydrodynamic mechanical device having Dirichlet-type pressure boundary conditions (BCs) at the pad edges

$$P_\Gamma \to P_a \ , \ \Gamma = \left\{ \theta = \theta_{i,e}, R_i \le r \le R_o \ \cup \ \theta_i \le \theta \le \theta_e, r = R_{i,o} \right\} \tag{42}$$

where P_a is ambient pressure and the bearing pad extends from $\theta_i \to \theta_e$ and $R_i \to R_o$. Solution of the Reynolds equation with Dirichlet-type BCs delivers the lubricant mass flows at the pad boundaries. Due to the small film thickness at the pad trailing edge, the mass flow exiting the pad is smaller than that entering the next pad,

Figure 48 displays two schematic views of a circumferentially tapered MMFTB during operation, where a thin gas layer separates the sliding thrust collar from the compliant mesh and thin top foils. In this operating condition, hydrodynamic pressure builds on the pads from their leading to trailing edges. In-between, and under the pads $P = P_a$. In addition, cooling flow supplies through the center of the test bearing loading shaft, impinging on the thrust collar center and then supplying to the bearing from its ID to OD (into the plane of the page as depicted in the Figure 48 (b) below). The internal cavity, enclosed by the pad IDs, the thrust collar front surface and the bearing support, accepts the cooling flow. The hydrodynamic pressure on the pads as well as the compact mesh undersprings (under the pads land sections) resist flow from the ID to the OD, while the areas between pads (A_{mixing}) and the areas under the pads in the tapered sections (A_{UP}) accept most of the flow from the internal cavity.

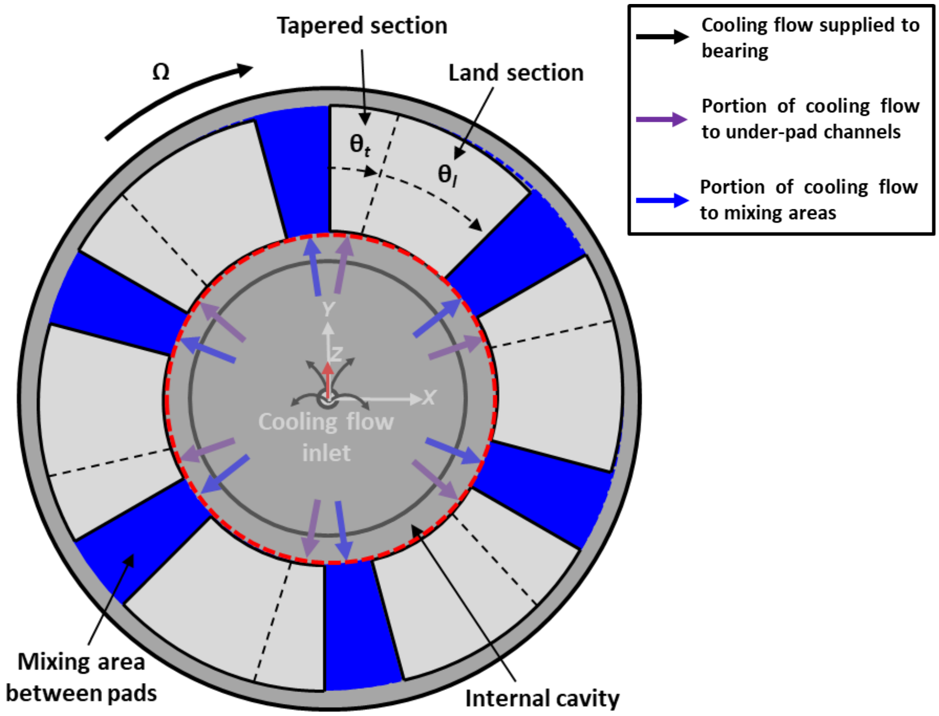

(a) Top-down view

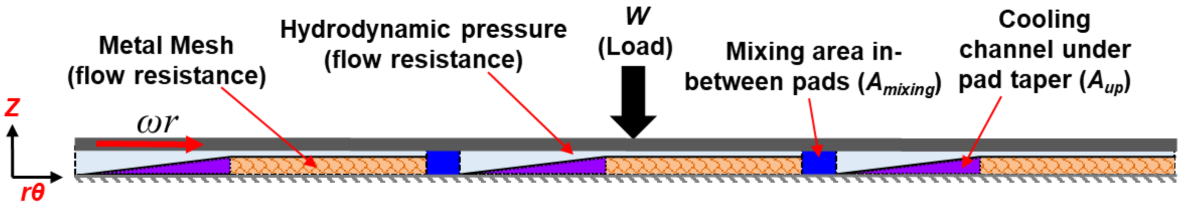

(b) Face-on (planar) view

Figure 48. Schematic representations of a MMFTB indicating areas of cooling flow.

Figure 49 displays a schematic view of a foil thrust bearing, highlighting a single pad and indicating mass flows through the pad boundaries, as well as those entering the internal cavity and exiting through the mixing area between pads and tapered portion beneath the pad. Solution of

Reynolds equation with Direchlet pressure boundary conditions yields the mass flows through the pads leading and trailing edges ($\dot{m}_i$, $\dot{m}_e$) as well as the leakage flow through the pad ID to the internal cavity and through the pad OD to ambient ($\dot{m}_{leak,ID}$, $\dot{m}_{leak,OD}$).

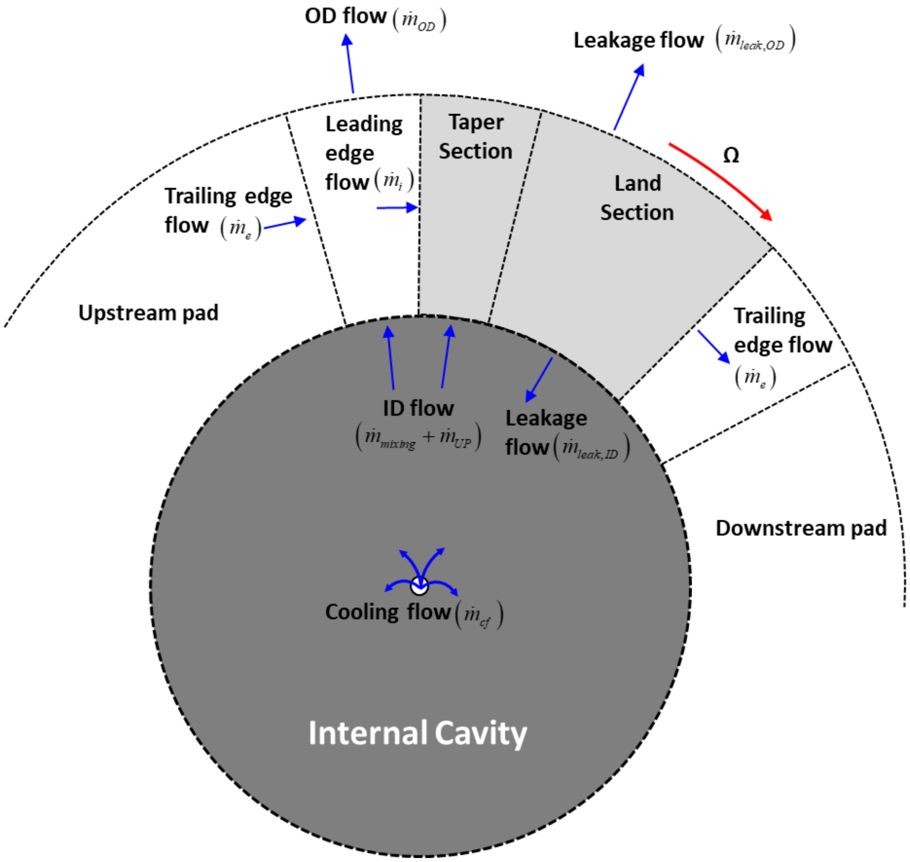

Figure 49. Schematic representation of mass flows for a foil thrust bearing.

The internal cavity remains at a constant pressure ($P = P_a$), and at steady state, a simple mass balance gives

$$N_{pad}\left(\dot{m}_{mixing} + \dot{m}_{UP}\right) = \dot{m}_{cf} + N_{pad} \cdot \dot{m}_{leak,ID} \tag{43}$$

where $\dot{m}_{mixing}$, $\dot{m}_{UP}$ are the mass flows directed to the mixing areas between the pads and areas under the pad tapers where there is no metal mesh. The current analysis assumes that the mass flow to each section is proportional to its cross-sectional area (A_{mixing} or A_{UP} as displayed in Figure 48 (b)), i.e.

$$N_{pad}\left(\dot{m}_{mixing}+\dot{m}_{UP}\right)=\dot{m}_{ID}$$

$$\dot{m}_{mixing}=\left(\frac{A_{mixing}}{\left\{A_{mixing}+A_{UP}\right\}N_{pad}}\right)\dot{m}_{ID}\quad \text{and}\quad \dot{m}_{UP}=\left(\frac{A_{UP}}{\left\{A_{mixing}+A_{UP}\right\}N_{pad}}\right)\dot{m}_{ID} \tag{44}$$

For simplicity, air leaving the internal cavity exits at a uniform temperature, equal to that of the internal cavity (T_{IC}). A simple energy balance for the internal cavity gives

$$T_{IC}=\left[\frac{\left(c_p\dot{m}T\right)_{cf}+\left(c_p\dot{m}T\right)_{leak,ID}+\bar{h}_{TC}\pi R_1^2 T_{TC}+\int_0^{2\pi}\int_0^{R_1}\left(\tau\cdot r\right)drrd\theta}{\left(c_p\dot{m}\right)_{ID}+\bar{h}_{TC}\pi R_1^2}\right] \tag{45}$$

where R_1 is the pad inner radius, $\bar{h}_{TC}$ is a convection coefficient for a rotating disk with an impinging cooling flow stream (see Appendix B), and $\tau \sim \mu\left(r\omega/t_{BS}\right)$ is the wall shear stress in the internal cavity, where the film thickness equals to the bearing support thickness (t_{BS}).

The flow deposited from the internal cavity to the area between pads mixes with flow exiting the upstream pad before entering the downstream pad or moving radially to exit through the mixing area OD. Figure 50 displays a schematic of the volume between pads, discretized with three control volumes. At steady state, a mass balance for the innermost CV in the (groove-like) volume between the pads gives

$$\dot{m}_{OD}=\dot{m}_{mixing}+\dot{m}_e-\dot{m}_i \tag{46}$$

A numerical scheme marches from the innermost CV, determining the flow through the CV OD via Eq. (46). If the OD flow is negative, the bearing draws from ambient air at the pad OD (maintained at T_∞).

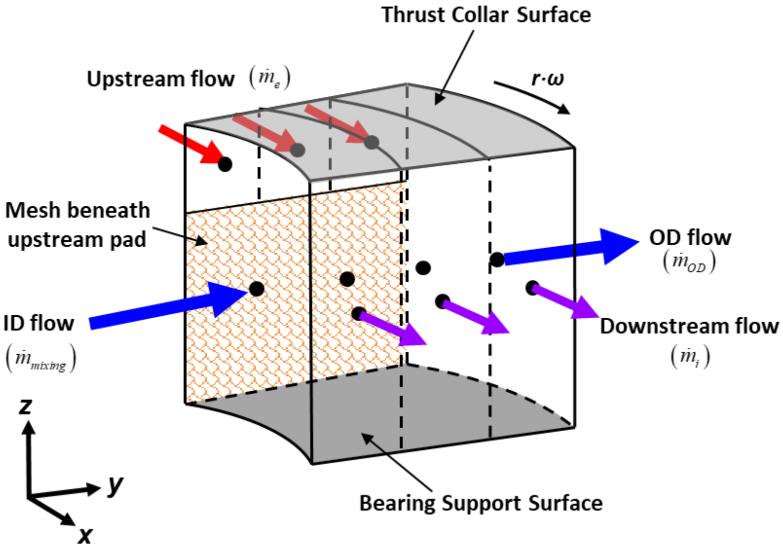

Figure 50. Schematic of the groove-like volume between pads including directions of fluid flows.

A bulk flow 2D energy equation (no vertical advection) in the groove-like volume between pads determines the fluid temperature. Note that the fluid in this volume remains at ambient pressure ($P = P_a$), and for simplicity has no viscous dissipation (large film thickness) and transfers no heat to the collar or bearing support, such that the energy equation reads

$$c_p \left[\frac{1}{r} \frac{\partial}{\partial r} \left(r T_i \dot{m}_r \right) + \frac{1}{r} \frac{\partial}{\partial \theta} \left(T_i \dot{m}_\theta \right) \right] = 0 \tag{47}$$

6.6 NUMERICAL METHOD OF SOLUTION

A control volume method, utilizing the exact shape functions of Faria and San Andrés [65], solves the compressible fluid Reynolds equation while the finite element method is employed to solve for the top foil elastic deformations. A control volume method with full upwinding is applied to determine the heat transfer in the thin film and groove-like volume between pads, while an energy balance determines the temperature in the internal cavity. Heat transfer through the bounding solids is also handled via control volume approaches. An iterative method utilizing successive under-relaxation solves the CV equations, satisfying convergence criteria defined for the fluid film pressure (P) and temperature (T) as well as the temperature of the bounding solids (T_{TC} and T_{tf}). An integral of the pressure difference ($P - P_a$) over the pad area renders the bearing axial reaction force. A simple Newton-Raphson approach updates the film thickness profile until and the resultant axial load (F) is within a specified tolerance of the user supplied applied load (W).

$$\varepsilon_P = \sum_{i=1}^{n}\left(\left|\frac{P_i^{j+1} - P_i^j}{P_i^j}\right|\right)\cdot 100 \ , \ \varepsilon_T = \max\left(\left|\frac{T_i^{j+1} - T_i^j}{T_i^j}\right|\right)\cdot 100 \ , \ \varepsilon_F = \left(\frac{W - F^j}{W}\right)\cdot 100 \qquad (48)$$

In Eq. (48), i, j represent the node and iteration numbers, respectively. Figure 51 summarizes the process described above, presenting a flow diagram for solution of the flow fields in a MMFTB.

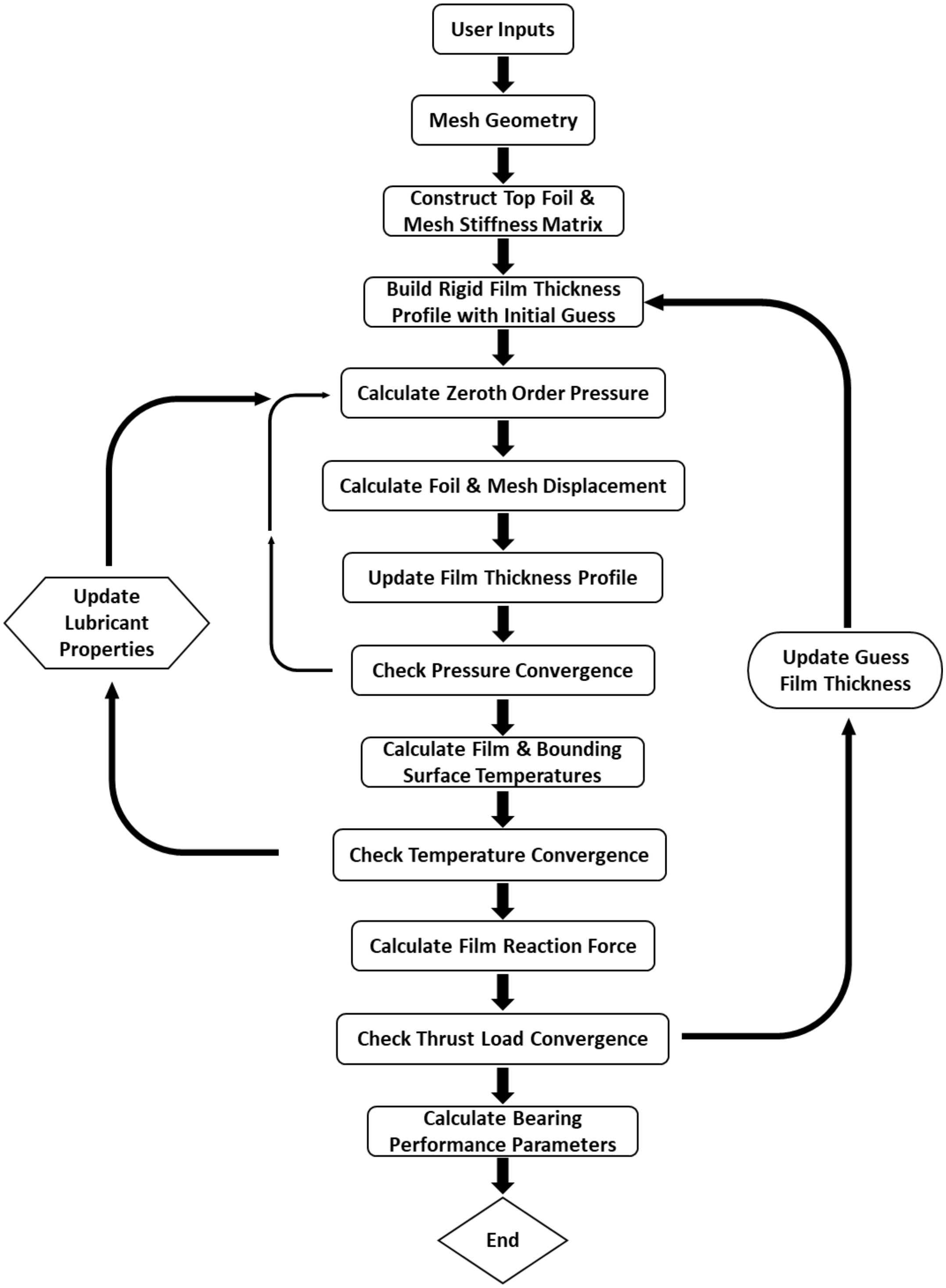

Figure 51. Flow chart for determining the operating film thickness and performance parameters of a metal mesh foil thrust bearing.

7. PREDICTIONS FOR A CIRCUMFERENTIALLY TAPERED METAL MESH THRUST FOIL BEARING

7.1 VERIFICATION AND VALIDATION OF THE CURRENT MODEL

7.1.1 COMPARISON OF PREDICTIONS FOR A RIGID SURFACE THRUST BEARING WITH ADIABATIC BOUNDARIES

Lehn [43] presents predictions for a rigid surface thrust bearing (with a Cartesian taper function) considering adiabatic boundary conditions as well as a fixed inlet temperature (T_i = 373 K). The model couples the compressible Reynolds equations (with non-slip boundary conditions) and a 3D energy equation to determine the pressure and temperature in the thin film. Table 10 gives the bearing geometry and operating conditions for the current analysis.

Table 10. Materials and geometry for analysis of a six-pad bump-type foil thrust bearing [43].

Thrust Collar, Bearing Support, Top Foil & Bump Foil Geometry	
Pad Inner and Outer Diameters, $D_{i,o}$ [mm]	30, 60
Top Foil Extent, θ_P [°]	40
Width of Land Region, x_{land} [mm]	6
Inclination of Taper Region, m [μm/mm]	2.9
Number of Pads, N_{pads} [-]	1

Table 10 Continued. Materials and geometry for analysis of a six-pad bump-type foil thrust bearing [43].

Operating Conditions	
Ambient Pressure, P_a [kPa]	100
Rotational Speed, ω [rad/s]	50-350
Fluid Inlet Temperature, T_{inlet} [K]	373.15
Film Thickness in Land Region, h_0 [μm]	10

Figure 52 displays the pad geometry and film thickness profile for a rigid surface bearing with dimensions and operating conditions as displayed in Table 10. The film thickness function for the Cartesian taper-land bearing is

$$h(x,y)=h_0+m(x-x_{land}) \tag{49}$$

where the pad is oriented such that $x = 0$ occurs at the trailing edge. Note that the film thickness is a maximum at pad leading edge and outer radius while being constant ($h = 10$ μm) in the land section.

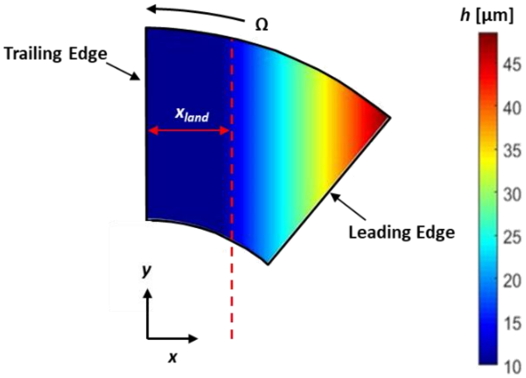

Figure 52. Pad geometry and film thickness for a rigid surface Cartesian taper-land bearing. Dimensions and operating conditions as displayed in Table 10.

Figure 53 displays film pressure and temperature predicted by Lehn [43] as well as that predicted with the current model for a minimum film thickness h_0 = 10 μm and a surface speed $\omega \cdot R_{mid}$ = 22.5 m/s. The contour plots in Figure 53 are nearly identical, showing good agreement between the predictions of Lehn and from the model herein. The maximum film pressure occurs at the transition between the taper and land sections, and closer to the pad outer diameter while the maximum temperature occurs at the pad trailing edge and at the outer radius. Despite a relatively slow surface speed (22.5 m/s), and a moderate film thickness in the land portion (h_0 = 10 μm), the film temperature rise is very large $\Delta T_{max} \sim 220$ K.

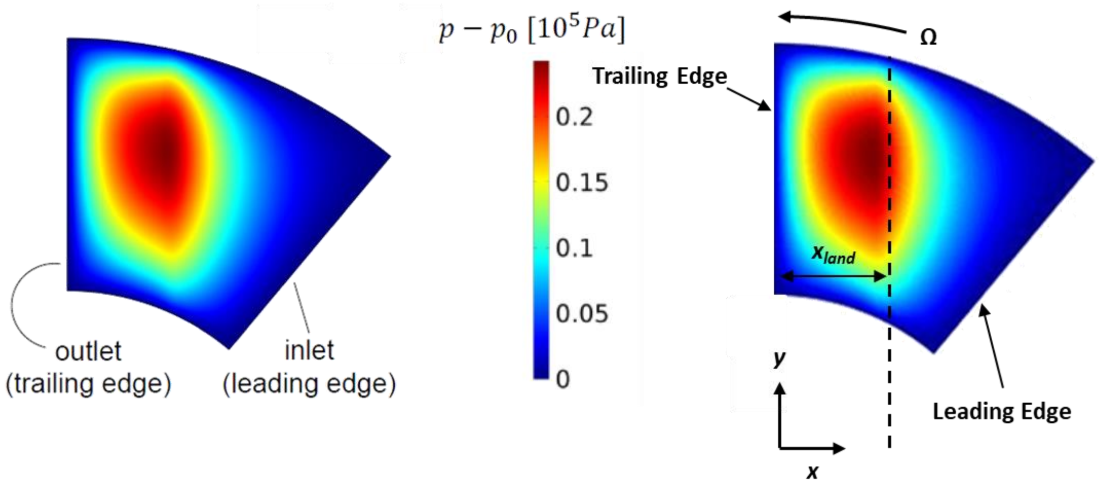

(a) Lehn [43] film pressure

(b) Film pressure

Figure 53. Film pressure and temperature for a single-pad rigid surface thrust bearing with adiabatic boundary conditions [43].

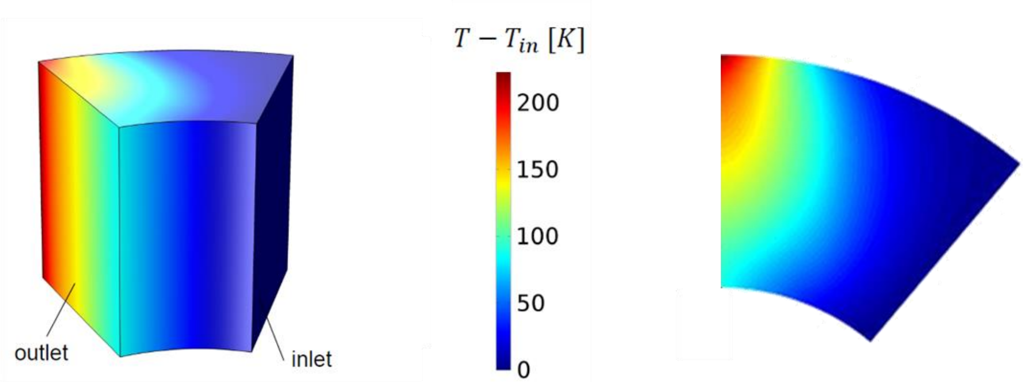

(c) Lehn [43] film temperature

(d) Film temperature

Figure 53 Continued. Film pressure and temperature for a single-pad rigid surface thrust bearing with adiabatic boundary conditions [43].

Figure 54 displays maximum film temperature rise and pad reaction force versus surface speed predicted by Lehn [43] as well as those predicted with the current model for a minimum film thickness $h_0 = 10$ μm. With adiabatic boundaries (no heat transfer to pad or thrust collar surfaces), the film temperature rise is excessive. An analysis by Lehn [43] reveals that planar advection is one-to-two orders of magnitude less than vertical (cross-film) diffusion for air bearings, because of the low density of air. The dissertation [43] shows that the opposite is true for oil bearings, where the planar advection dominates, and the film flow in the direction of rotation can carry away most of the generated heat. Despite the excessive temperature rise, predictions from both models agree well for both the max temperature rise and the pad reaction force, showing that the bulk-flow model presented herein captures well the physics in an air lubricated thrust bearing.

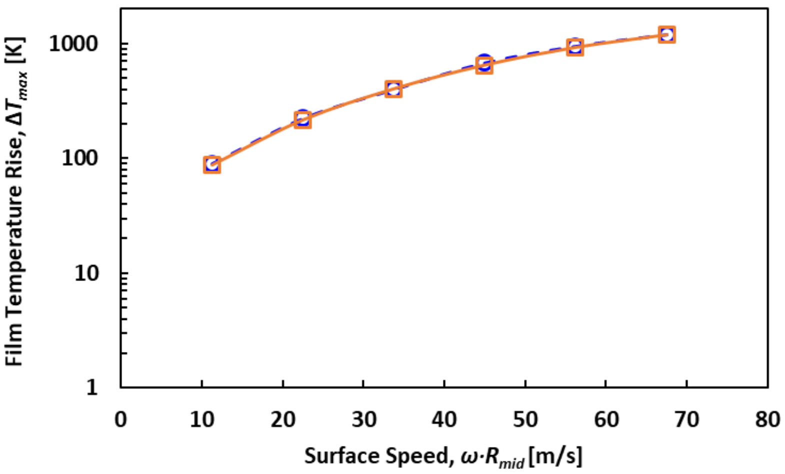

(a) Maximum film temperature rise

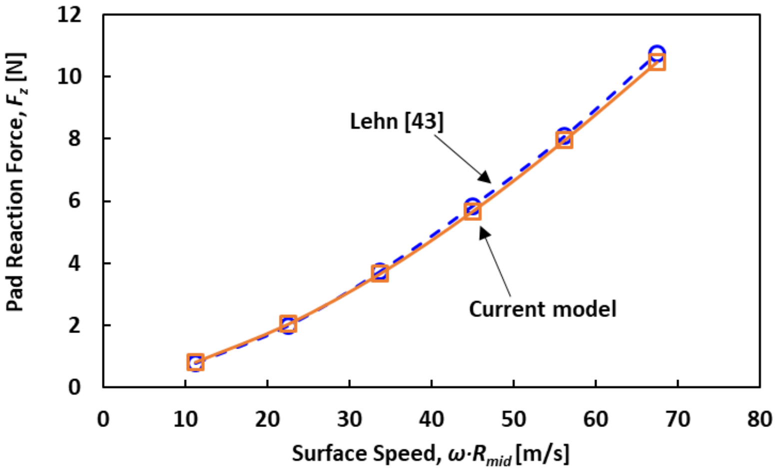

(b) Pad reaction forces

Figure 54. (a) Maximum film temperature rise and (b) pad reaction force for a rigid, adiabatic surface thrust bearing

7.1.2 COMPARISON OF PREDICTIONS FOR A GEN I BUMP-TYPE FOIL THRUST BEARING

Works at NASA and Case Western [16-19] provide the most complete open source data set for simple foil thrust bearings, thus becoming the de facto standard for comparison and validation of compliant surface thrust bearing models. Qin *et al*. [45] provide a detailed analysis of a single compliant surface pad using commercial software (see Chapter 2 for a more thorough description of their work). Tables 11 & 12 display the geometry, material properties and operating conditions utilized in their analysis while Figure 55 displays a schematic of a single bearing pad with a bump-foil undersrping structure.

Table 11. Materials and geometry for analysis of a six-pad bump-type foil thrust bearing [44].

Thrust Collar, Bearing Support, Top Foil & Bump Foil Geometry	
Material (thrust collar, bump/top foils & bearing support)	Stainless Steel
Thermal Conductivity, $\kappa_{TC,BF,tf,BS}$ [W/(m.K)]	15.4
Elastic Modulus, $E_{TC,BF,tf}$ [GPa]	200
Thrust Collar & Bearing Support Thicknesses, $t_{TC,BS}$ [mm]	16, 20
Bump Foil & Top Foil Thicknesses, $t_{bf,tf}$ [mm]	0.1, 0.15
Thrust Collar Inner & Outer Diameters, ID_{TC}, OD_{TC} [mm]	46, 101.6
Top Foil Inner and Outer Diameters, $D_{i,o}$ [mm]	50.8, 101.6
Top Foil Extent, θ_P [°]	45
Top Foil Tapered Extent, θ_t [°]	15
Taper Height, h_t [µm]	50

Table 11 Continued. Materials and geometry for analysis of a six-pad bump-type foil thrust bearing [44].

Thrust Collar, Bearing Support, Top Foil & Bump Foil Geometry	
Number of Pads, N_{pads} [-]	6
Number of Bump Strips, n_{strips} [-]	5
Strip Width, w_b [mm]	5.08
Bump Strip Mean Radii, R_{mid} [mm]	28, 33, 38, 43, 48
Bump Pitches (ID to OD), b_p [mm]	5.36, 5.19, 4.65, 3.77, 5.90
Number of Bumps/Strip (ID to OD), n_{bump} [-]	3, 4, 5, 6, 5
Bump Height, h_b [μm]	508
Bump Radius, R_b [mm]	1.6

Table 12. Operating conditions for analysis of a six-pad bump-type foil thrust bearing [45].

Operating Conditions	
Ambient Pressure, P_a [kPa]	100
Rotational Speed, Ω [krpm]	21
Specific Load (per pad), W/A [kPa]	24
Bearing Support & Ambient Temperatures, $T_{BS,\infty}$ [K]	300

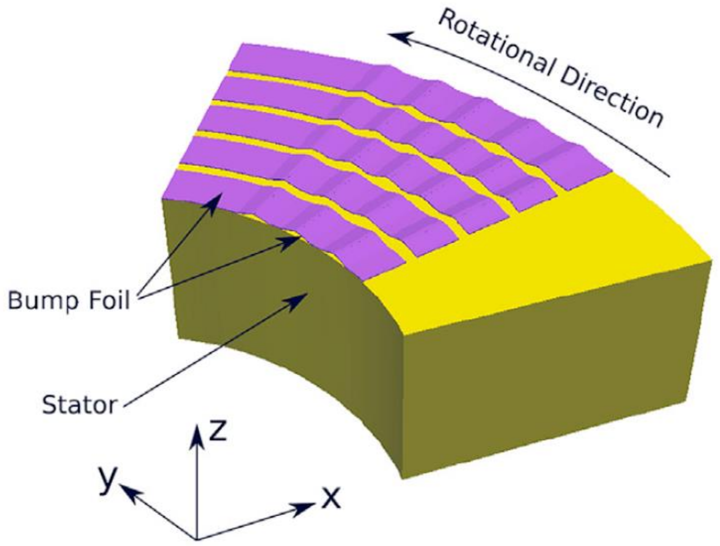

Figure 55. Schematics of a single-pad bump-type foil thrust bearing in Ref. [44].

Modeling the structural behavior of a bump-foil strip (like that depicted schematically in Figure 55) is complex, and as such, has been the topic of several works in the literature [12,15,68-71]. Early models from Heshmat [12] and Iordanoff [15] consider the deflection of a single (isolated) bump, not taking into account its interactions with adjacent bumps. Over the years, researchers developed more complex (multi-degree-of-freedom (MDOF)) models which more closely capture the foil behavior [68-71].

Qin *et al.* [45] utilize the bump-foil structural model of Gad and Kaneko [69] to determine the elastic deflections of the bump-foil structure. Integrating a complex (matrix based) MDOF bump-foil model into the existing model (Chapter 6) for comparative purposes is beyond the scope of this work. However, predictions herein (displayed in Appendix C) show that the current structural model and implementing Iordanoff's closed form solution for bump stiffness predicts well the behavior a bump-foil with geometry as displayed in Table 11.

To include thermal effects in the foil, Qin *et al*. [45] utilize an empirically determined bump contact resistance which varies with contact pressure [41]. The current analysis utilizes a closed-form thermal resistance developed by Lehn *et al.* [42], shown to be similar to that determined experimentally in [40]. As in Ref. [45], 48 x 96 (radial by circumferential) CVs mesh the computational domain. Ref. [42] doesn't discuss the error criteria for convergence, thus, a common error criteria ($\varepsilon_{P,T} \leq 10^{-6}$) from the literature [41] is adopted for the pressure and temperature equations.

Figure 56 displays temperature boundary conditions and heat flows in the domain under consideration. Heat due to fluid shear and pressure extrusion in the thin film convects to the thrust collar and the thin top foil. In the thrust collar, the heat conducts through its thickness, traveling to the inner shaft maintained at T_S = 300K and convecting from its back surface and outer diameter to ambient (maintained at T_∞ = 300 K). The heat flowing to the top foil conducts through its thickness, through the bump foil crests in contact with its backside, and finally to the stator backside of the stator (maintained at T_{BS} = 300 K). In addition, natural convection occurs between the backside of the foil and ambient (T_∞ = 300 K).

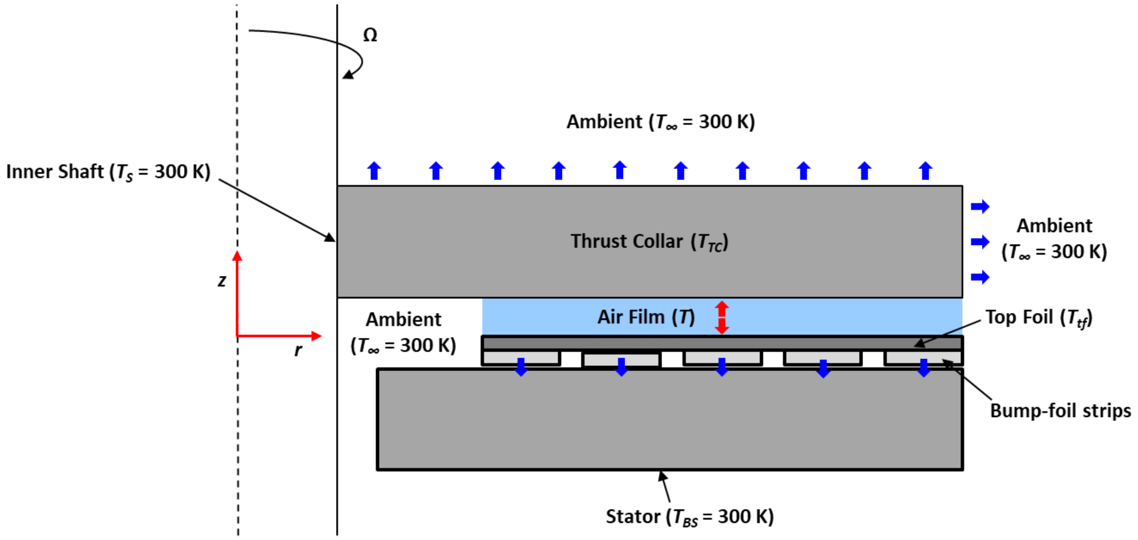

Figure 56. Schematic of heat flows and temperature boundary conditions utilized in the analysis of Qin *et al*. [45].

Figure 57 displays surface plots of hydrodynamic pressure, top-foil deflection and film thickness over the pad for a rotational speed Ω = 21 krpm ($\omega \cdot R_{mid}$ ~ 84 m/s) and a specific load *W/A* ~ 24 kPa. Qin *et al.* [45] solve the flow equations on the pad and in the mixing groove (extending a total of 60°), while the current model solves the flow equations over the pad only (extending a total of 45°). In addition, to present the best comparison, care is taken to align the magnitudes and colors of the legends between the two pressure plots. Do note that **no** sub-ambient pressure occurs over the pad, although the legends in the contour plots may be deceiving.

Results in Figure 57 show similar pressure distributions for the tapered regions while the pressures predicted in the land regions are quite dissimilar (albeit with similar magnitudes). The predictions of Qin *et al.* [45], typical for a high rotor speed and small film, show a relatively uniform film pressure in the land section, with the peak pressure locating the pad trailing edge and at the pad mid-radius. Appendix C presents and analysis showing that the bearing pad (top foil + underspring) is stiffest over the fourth bump-strip (R_{mid} = 43 mm), where the bump pitch is the smallest and the number of bumps the greatest. The pressure field over the pad predicted with the current model (Figure 52 (b)) aligns with this finding, showing a peak pressure located over the fourth bump-strip. The top-foil deflection is largest near the pad outer radius, with a correspondingly large film thickness in the same location. Nearly the entire land region operates with h ~ 11 μm, showing local high spots in-between bump crests.

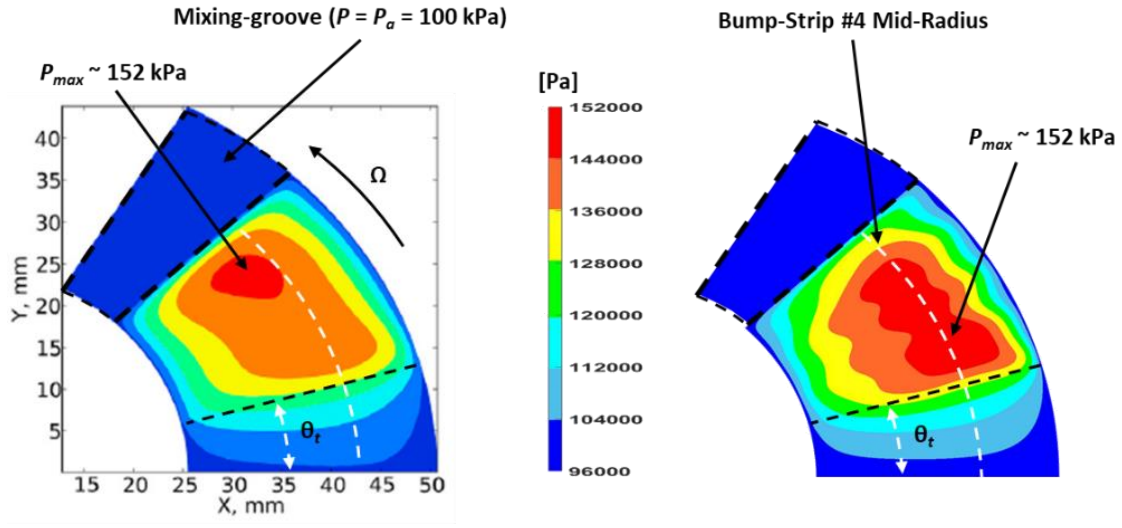

(a) Qin *et al.* Film Pressure [Pa]

(b) Film Pressure [Pa]

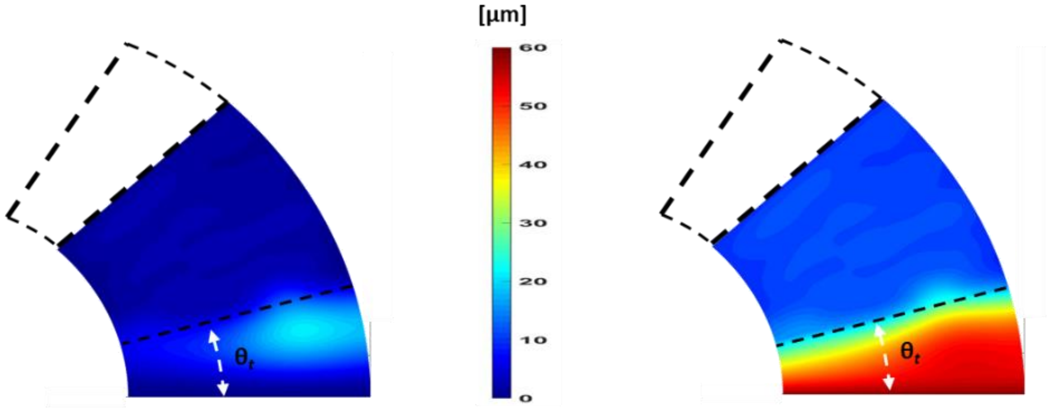

(c) Deflection [µm]

(d) Film Thickness [µm]

Figure 57. Hydrodynamic pressure, top-foil deflection and film thickness over the pad surface for a bump-type foil thrust bearing operating with air. W = 110 N, Ω = 21 krpm, T_∞ = 300 K.

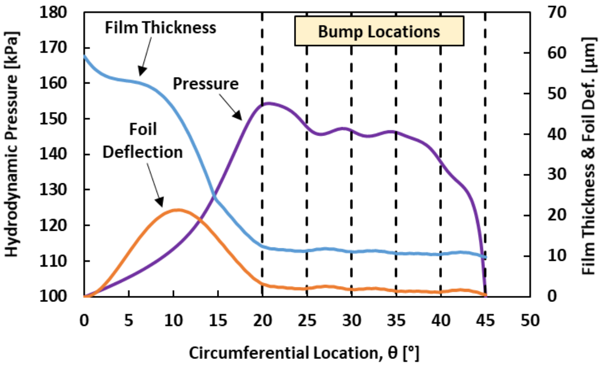

(e) Field Variables at Bump-Strip #4 Mid-Radius (herein)

Figure 57 Continued. Hydrodynamic pressure, top-foil deflection and film thickness over the pad surface for a bump-type foil thrust bearing operating with air. W = 110 N, Ω = 21 krpm, T_∞ = 300 K.

In addition to the steady-state pressure distribution over the pad, Ref. [45] provides surface plots of the rotor collar and top foil temperatures at the surfaces exposed to the thin fluid film as well as the bearing power loss, and a mapping of heat flows throughout the computational domain. For a rotor speed of Ω = 21 krpm ($\omega \cdot R_{mid}$ ~ 84 m/s) and a specific load W/A ~ 24 kPa Qin *et al.* [45] predict the bearing power loss to be PL ~ 48 W and with a minimum film thickness of h_{min} = 10.1 μm. The current model herein predicts PL ~ 48.5 W and with a minimum film thickness of h_{min} = 9.8 μm. The differences in the pressure distributions, causing a smaller film thickness and smaller drag torque in the current model predictions, are attributed to the differences in bump-foil structural models between the two approaches.

Despite the slight differences in steady state power loss, the predicted temperature of the bounding solids are quite similar. Figure 58 displays top foil and rotor collar temperatures for the same foil thrust bearing operating with Ω = 21 krpm ($\omega \cdot R_{mid}$ ~ 84 m/s) and a specific load

W/A ~ 24 kPa. Comparing first the qualitative information from the two figures in Figure 58, the highest temperatures occur in the tapered region of the pad, where heat transfer from the pad backside is limited to natural convection, and a small heat transfer coefficient $\bar{h}_{tf} \approx 5\ \mathrm{W}/\left(\mathrm{m}^2 \cdot \mathrm{K}\right)$. In the land section, the temperature dissipates slightly towards the trailing edge of the pad as heat conducts through the bump foils, creating local "cool" spots just above the locations where the bumps contact the top foil. Quantitatively, the top foil temperature in the current predictions is slightly lower than that predicted by Qin *et al.* [45] (318 K compared to 322 K).

The temperature of the thrust collar surface in direct contact with the thin fluid film increases from the inner to the outer diameter. Recall that the collar inner radius is set at a fixed temperature T_{TC} = 300 K. Comparing the two sets of predictions, both show a max thrust collar temperature of T_{TC} ~ 312 K.

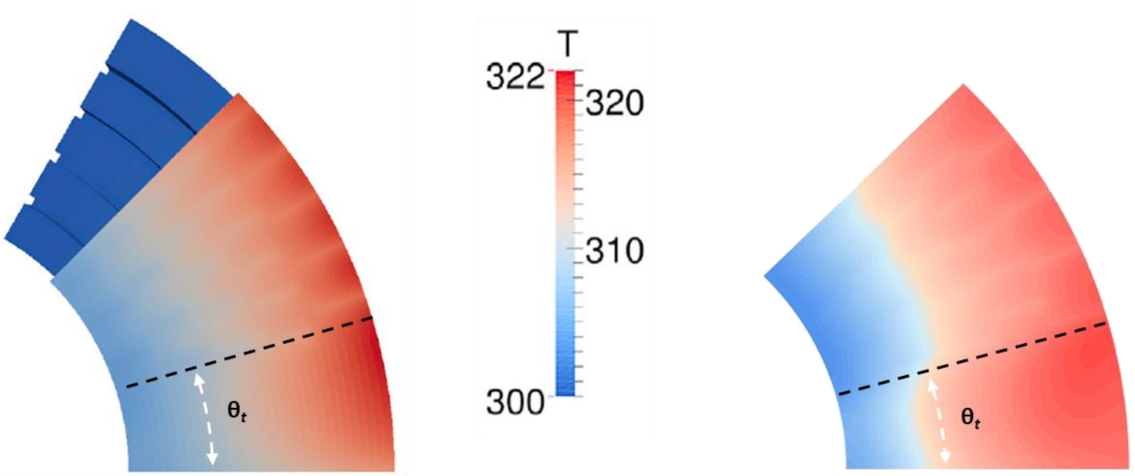

(a) Top-foil Temperature Ref. [44]

(b) Top-foil Temperature (model herein)

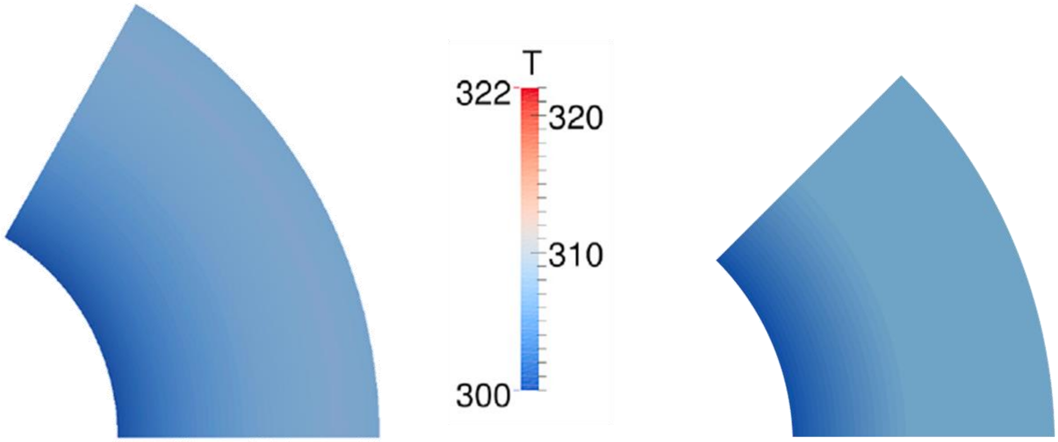

(c) Collar Surface Temperature Ref. [44]

(d) Collar Surface Temperature (model herein)

Figure 58. Top-foil and thrust collar temperatures for a bump-type foil thrust bearing operating with air. W = 110 N, Ω = 21 krpm, T_∞ = 300 K.

Figure 59 provides a schematic comparison (Qin *et al*. vs current model) of the predicted heat flows to the bounding solids and that carried away by the moving film. The two sets of predictions show that the majority of the heat flows into the thrust collar and passes from its periphery to ambient, while only a small fraction (less than 10% in both cases), passes to through the top foil and to the bearing support or to ambient air beneath the pad taper. In addition, both models agree on the tiny fraction of heat carried away by the air film (less than 5%), due to the low density of the working medium [45]. The results in Figure 59 are in line with predictions from other thermo-elastohydrodynamic models [42,45]. Note that an isothermal analysis (with T = 300 K) predicts nearly the same power loss (47.68 W) as the TEHD model since both the surface speed ($\omega \cdot R_{mid}$ ~ 87 m/s) and thrust load (W/A~ 25 kPa) are small. Despite the TEHD and isothermal models predicting similar static bearing performance, a proper thermal model is necessary for foil bearing designers to ensure peak film and foil temperatures remain moderate so as to avoid thermal runaway events [16-20].

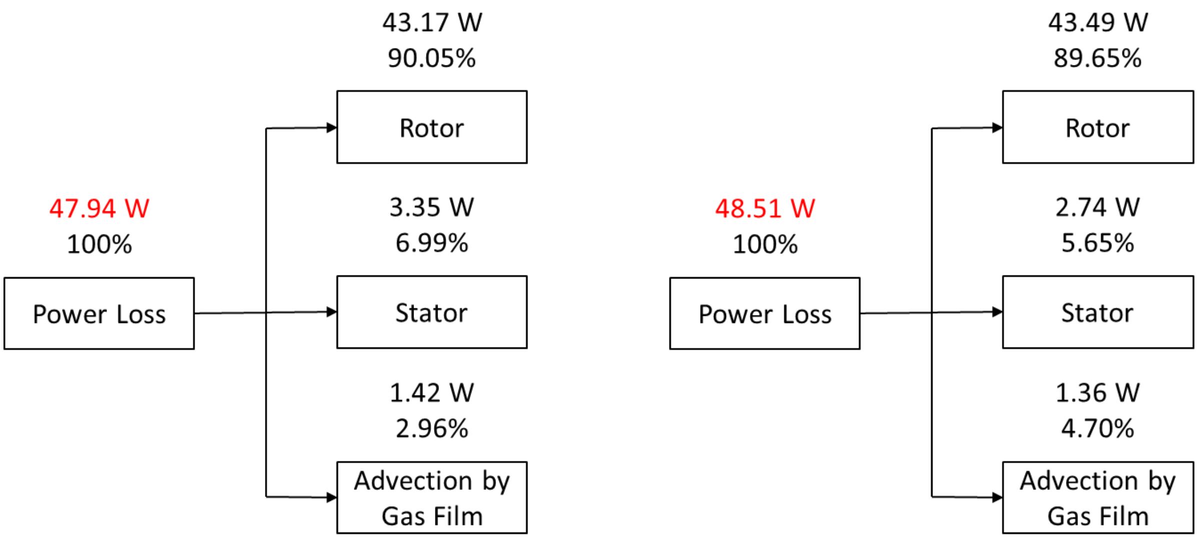

(a) Qin *et al* [42]

(b) Model herein

Figure 59. Summary of heat flows for a bump-type foil thrust bearing operating with air. W = 110 N, Ω = 21 krpm, T_∞ = 300 K.

7.1.3 COMPARISON OF PREDICTIONS FROM THE CURRENT MODEL TO MEASUREMENTS FOR A GEN I BUMP-TYPE FOIL THRUST BEARING

Figure 60 displays a photograph of a six-pad bump-type foil thrust bearing tested by Dickman *et al*. [9] while Table 13 contains its geometry and materials. Note that the taper height utilized in the previous section by Qin *et al*. [44], h_t = 50 μm. Referring to Figure 60 (b) (and considering the parameters listed in Table 13), the theoretical taper height for the foil thrust bearing equals to the bump foil thickness plus the bump height, i.e.

$$h_t = h_b + t_{bf} \tag{50}$$

Table 13. Bearing Geometry for analysis of a six-pad bump-type foil thrust bearing [18].

Thrust Collar, Bearing Support, Top Foil & Bump Foil Geometry	
Thrust Collar & Bearing Support Materials	Inconel 718
Thermal Conductivity, $\kappa_{TC,bf,tf,BS}$ [W/(m.K)]	11.4
Thrust Collar & Bearing Support Thicknesses, $t_{TC,BS}$ [mm]	12.7, 6.35
Bump & Top-Foil Materials	Inconel X-750
Elastic Moduli, $E_{bf,tf}$ [GPa]	213
Thermal Conductivity [W/(m.K)]	16.4
Thrust Collar Inner & Outer Diameters, ID_{TC}, OD_{TC} [mm]	43, 101.6
Bump Foil & Top Foil Thicknesses, $t_{BF,tf}$ [mm]	0.1, 0.15
Top Foil Inner and Outer Diameters, $D_{i,o}$ [m]	50.8, 101.6
Top Foil Extent, θ_P [°]	45
Top Foil Tapered Extent, θ_t [°]	17
Taper Height, h_t [μm]	610

Table 13 Continued. Bearing Geometry for analysis of a six-pad bump-type foil thrust bearing [18].

Thrust Collar, Bearing Support, Top Foil & Bump Foil Geometry	
Number of Pads, N_{pads} [-]	6
Number of Bump Strips, n_{strips} [-]	5
Strip Width, w_b [mm]	5.08
Bump Strip Mean Radii, R_{mid} [mm]	28, 33, 38, 43, 48
Bump Pitches (ID to OD), b_p [mm]	5.36, 5.77, 5.31, 4.52, 5.89
Number of Bumps/Strip (ID to OD), n_{bump} [-]	3, 3, 4, 6, 5
Bump Height, h_b [μm]	508
Bump Radius, R_b [mm]	1.588

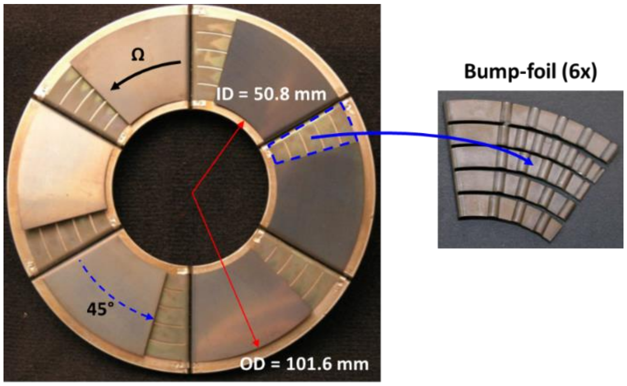

(a) Photographs of bump-foil thrust bearing [9]

Figure 60. (a) Photograph of a six-pad BFTB [9] and (b) a schematic of the bump-foil underspring.

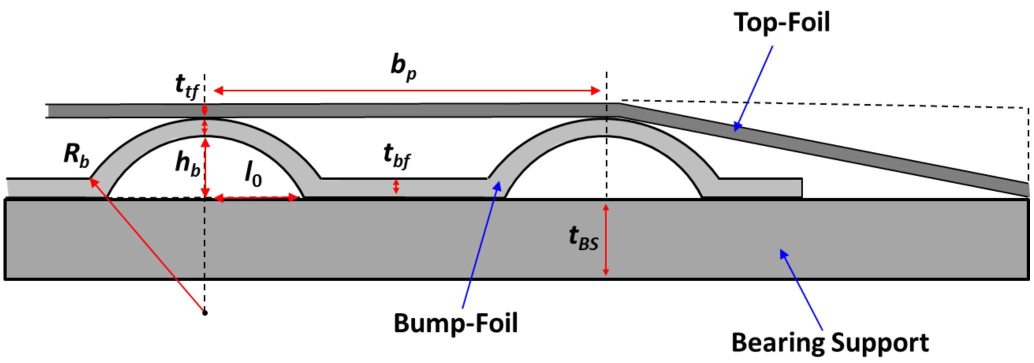

(b) Schematic of a bump-foil pad including geometric parameters

Figure 60 Continued. (a) Photograph of a six-pad BFTB [9] and (b) a schematic of the bump-foil underspring.

Several researchers [4,45,69] have presented predictions for the thrust foil bearings of Dykas, Dickman and Stahl [9,18,19]; however, there is confusion in the literature as to the respective bearing geometries (taper heights and bump-foil configurations). Table 14 summarizes the pad and bump-foil geometry utilized by each researcher, as well as the correct bump-foil and thrust bearing geometry from Dykas, Dickman and Stahl gleaned from several different references [9, 18-20].

Table 14. Pad and bump-foil geometries from the literature [4,9,18-20,45,69].

	Bump Strips [-]	Bumps Per Strip [-]	Bump Spacing [°]	Taper & Pad Extents [°]	Taper Height [μm]
Dykas *et al*. [9]	5	3, 4, 5, 6, 5	11, 9, 7, 5, 7	17, 45	610
Dickman “BNB” [18]	5	3, 3, 4, 5, 5	11, 10, 8, 6, 7	17, 45	610
Stahl “TEE” [19]	5	3, 3, 4, 5, 4	10, 11, 9, 7, 8	17, 45	610
San Andrés *et al.* [4]	1	9	3.75	15, 45	50
Qin *et al.* [45]	5	3, 4, 5, 6, 5	11, 9, 7, 5, 7	15, 45	50
Gad & Kaneko [69]	5	3, 3, 4, 6, 5	11, 9, 7, 5, 7	17, 45	500

As displayed in Table 14 and Figure 60, the bearing from Ref. [9] has a theoretical taper height h_t = 610 μm and five bump strips with 3, 4, 5, 6, & 5 bumps per strip (strips arranged ID to OD). The predictions from Gad & Kaneko [69], meant to mimic the bearing of Dykas *et al.* [9], utilize h_t = 500 μm and a bump foil with 5 strips, having: 3, 3, 4, 6 & 5 bumps per strip. The apparent difference between the analysis of Gad & Kaneko [69] and the geometry displayed in Figure 60 may be explained by the number of “complete” bumps in each strip. While the bump foil strip pictured in Figure 55 appears to have 3, 4, 5, 6, & 5 bumps per strip, the final bumps in strips 2, 3, & 5 are not full, and may not contribute to the bump-foil structural stiffness. Note that the structural model utilized in Ref. [69] neglects the top foil, modeling only the deflection of the bumps and assuming the thin top foil follows exactly the bump deformation. Despite these differences, the analysis by Gad and Kaneko [69] utilizes a bearing with dimensions and material properties most similar to that tested in Ref. [9].

Figures 61 & 62 display test results from Dykas *et al.* [9] along with several sets of predictions for bearing drag torque, minimum film thickness and maximum film temperature rise versus specific load for a collar operating at Ω =23 krpm ($\omega \cdot R_{mid}$ ~ 92 m/s). Note that the predictions utilize a bump foil with 5 strips, having: 3, 3, 4, 6 & 5 bumps per strip and h_t = 500 μm, as in Ref. [69]. Figure 61 shows measured bearing drag torque [9] increasing linearly until W/A~ 18 kPa, after which the film thickness (predicted) drops below 5 μm. Predictions from the model herein as well as those from Ref. [69] slightly overpredict the bearing drag torque at low speeds, and underpredict the drag torque as the bearing approaches its load capacity (W/A ~ 27.5 kPa). Due to the low viscosity of air, and the relatively slow surface speed ($\omega \cdot R_{mid}$ ~ 92 m/s), the isothermal model produces nearly the same results.

As described in Refs. [4,69] the method in which the top and bump foils affix to the bearing back does not guarantee the theoretical taper height is achieved, and the bearing may have a smaller taper height in practice. Without a measured taper height, correlating bearing test data and predictions relies on the researcher’s experience and practical knowledge of foil bearings. Ultimately, the predictions presented in Figure 61show that the current model holds up well to other (complex) models presented in the literature [69], and with the correct bump geometry, predicts well the static behavior of a bump-type foil thrust bearing.

Like the predictions of Qin *et al.* [45], the thermo-elastohydrodynamic model predicts similar steady-state performance to that predicted by the isothermal model. Do bear in mind that a proper thermal model is necessary for the design of cooling flow channels which maintain a moderate (~ 100 °C) foil temperature rise and lessen the possibility of thermal runaway [43].

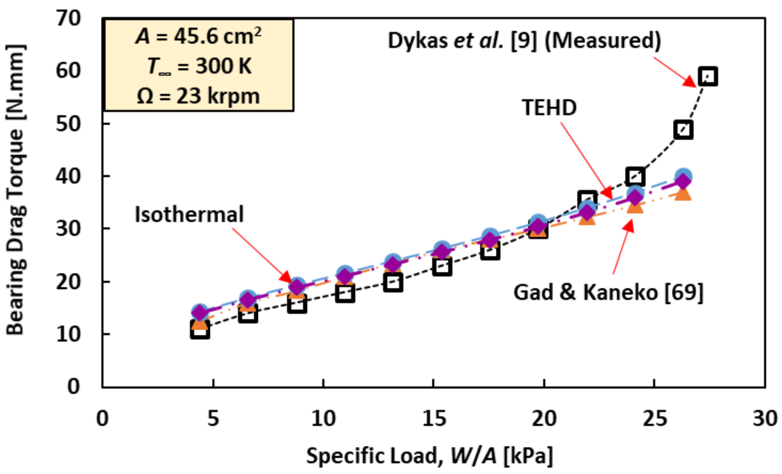

Figure 61. Bearing drag torque versus applied specific load for a six-pad bum-type foil thrust bearing tested in Ref. [9].

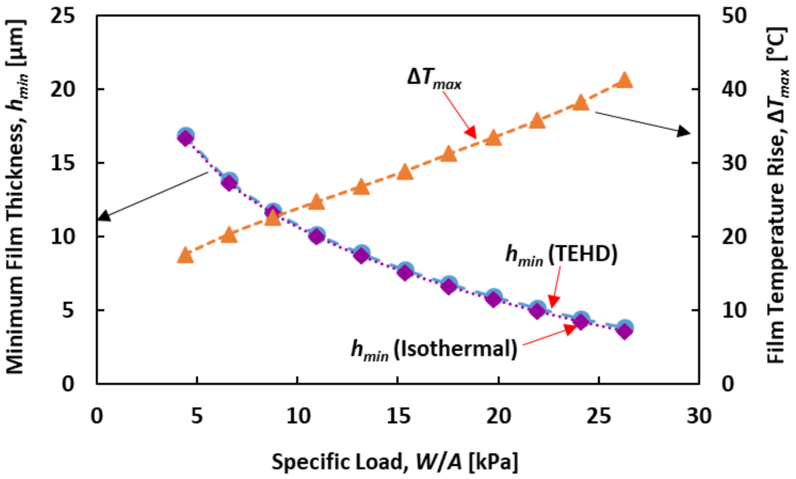

Figure 62. Minimum film thickness and film maximum temperature rise versus applied specific load for a six-pad bum-type foil thrust bearing tested in Ref. [9].

7.2 A COMPARISON OF PREDICTED AND MEASURED BEARING DRAG TORQUE FOR A SIX-PAD CIRCUMFERENTIALLY TAPERED MMFTB

Table 15 displays bearing geometry and material parameters utilized in the testing of a six-pad MMFTB. Figure 17 (static load vs displacement) shows that when a MMFTB with 3 sheets of 40 OPI mesh is fully loaded, the pad stiffness approaches $K_{MM} \sim 3.5$ MN/m. The current analysis assumes this fully loaded stiffness distributes uniformly to the land section of the pad $K_{MM}/A_{land} = 8.76$ GN/m^3. In addition, a closed form expression [77] determines the mesh equivalent thermal conductivity per sheet (see Appendix B for more details).

Table 15. Bearing Geometry for analysis of a six-pad metal mesh foil thrust bearing.

Thrust Collar, Bearing Support, Top Foil & Bump Foil Geometry	
Thrust Collar Material	4140 Stainless Steel
Thermal Conductivity, κ_{TC}	42.6 [W/(m.K)]
Thrust Collar & Bearing Support Thicknesses, $t_{TC,BS}$	13.7, 9.53 [mm]
Thrust Collar Outer Diameter, OD_{TC}	142 [mm]
Top-Foil & Bearing Support Materials	316 Stainless Steel
Elastic Moduli, E_{tf}	200 [GPa]
Thermal Conductivity, $\kappa_{tf, BS}$	16.3 [W/(m.K)]
Top Foil Thicknesses, t_{tf}	0.1016 [mm]
Top Foil Inner and Outer Diameters, $D_{i,o}$	50.8, 101.6 [mm]
Top Foil Extent, θ_P	55 [°]
Top Foil Tapered Extent, θ_t	25 [°]

Table 15 Continued. Bearing Geometry for analysis of a six-pad metal mesh foil thrust bearing.

Thrust Collar, Bearing Support, Top Foil & Bump Foil Geometry	
Taper Height, h_t	570 [μm]
Number of Pads, N_{pads}	6 [-]
Underspring Mesh Material	Copper
Mesh Size	40 [OPI]
Wire Diameter, w_d	0.254 [mm]
Number of Mesh Sheets, n_{MM}	3 [-]
Mesh Effective Thermal Conductivity, κ_{MM}	0.20 [W/m.K]
Mesh Stiffness per Unit Area, K_{MM}/A_{land}	8.76 [GN/m^3]

Figure 63 (a) & (b) display minimum film thickness and a friction factor $f = T/(F \cdot R_{mid})$ versus applied specific load for a six-pad MMFTB with 3 sheets of 40 OPI mesh and operating with Ω = 40 krpm and Q_{cf} = 300 LPM. Note that the predicted minimum film thickness $3 \leq h_{min} \leq 20$ μm for the loads comprised between $5 \leq W/A \leq 25$ kPa. For all loads, the experimentally determined f is approximately three times larger than predictions, while the predicted f is similar to that of other gas foil thrust bearings in the literature [4,19].

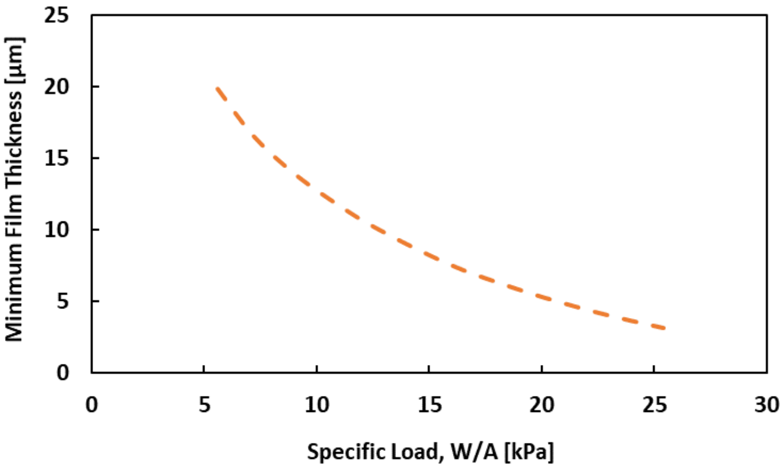

(a) Minimum film thickness vs specific load

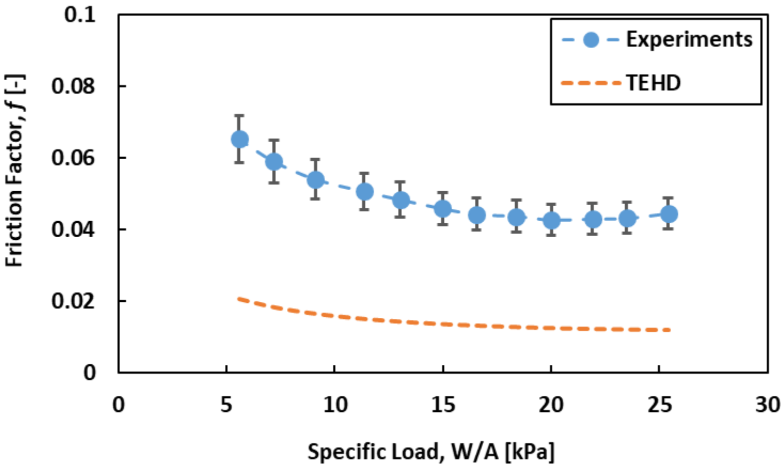

(b) Bearing friction factor vs specific load

Figure 63. Bearing (a) minimum film thickness and (b) friction factor versus applied specific load for a six-pad MMFTB. Ω = 40 krpm, T_∞ = 330 K, Q_{cf} = 300 LPM.

Figure 64 displays measured and predicted steady-state pad temperature versus specific load for the six-pad test MMFTB operating with Ω = 40 krpm and Q_{cf} = 300 LPM. Note that thermally conductive epoxy bonds thermocouples to the backsides of three of the six bearing pads. An insert in Figure D2 shows the thermocouple fixture location on a single pad, in the tapered portion 20° from the leading edge and at the pad mid-radius. The three pads have dissimilar temperatures, with pad #1 operating the hottest. At low loads, and despite largely different measured and predicted bearing drag torques, the predicted foil temperature at the fixture location is similar to that displayed by the three thermocouples. After *W/A* > 15 kPa, the three pad temperature measurements exceed the predictions.

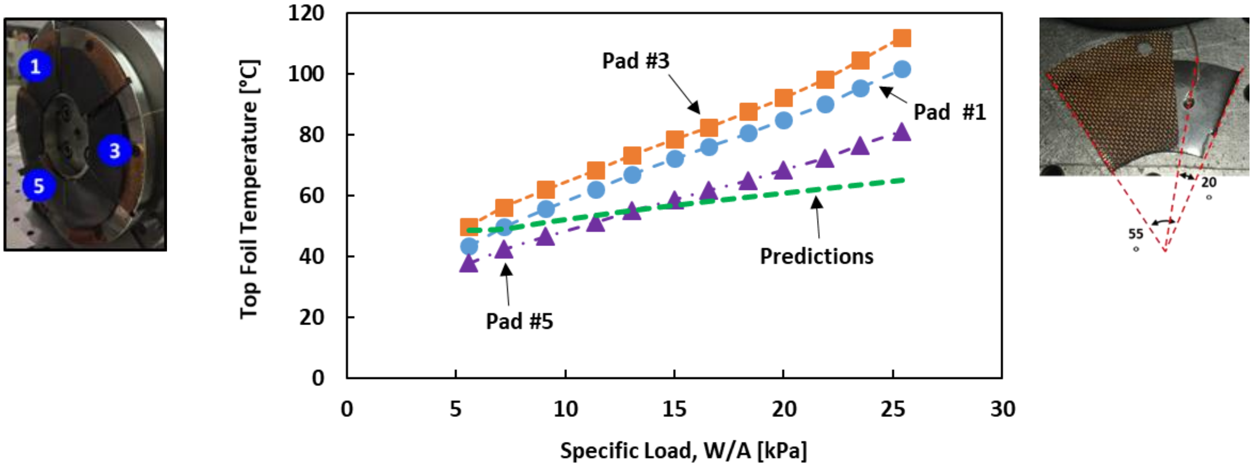

Figure 64. Pads temperatures versus applied specific load for a six-pad MMFTB. Ω = 40 krpm, T_∞ = 330 K, Q_{cf} = 300 LPM.

As the experimental bearing geometry is known (see Table 15) and the rotor collar speed and the applied load are measured, Figure 65 examines how other factors (metal mesh stiffnesss and pad taper height) affect bearing drag torque and minimum film thickness. The analysis presented in Figure 65 considers Ω = 40 krpm, and *W/A* ~ 20 kPa, the last load step before the bearing experimental load capacity (*W/A* ~ 22 kPa). The predictions show that the bearing drag torque decreases as the pad taper decreases. For a smaller taper height, more hydrodynamic pressure builds in the tapered section of the pad, and the land section operates with a larger film thickness. For each taper height, increasing the mesh stiffness increases the bearing drag torque, to a point. As most mesh bearings in the literature show $K_{MM} \leq 10$ GN/m^3 [3,53,55], a mesh stiffness above 25 GN/m^3 renders an essentially rigid underspring. Note that a bearing with a taper height $h_t > 570$ μm likely does not support a load of $W/A > 20$ kPa, as its minimum film thickness (regardless of mesh stiffness) falls below 5 μm.

Results in Figure 65 (a) provide upper and lower bounds for the bearing drag torque for a bearing with dimensions as in Table 15, and this set of operating conditions ($\Omega = 40$ krpm, and $W/A \sim 20$ kPa). Increasing the fluid and ambient temperatures (by 100 °C or less) has little effect on the analysis (not shown), as the viscosity of air is very small. Even for a rigid bearing ($K_{MM} > 25$ GN/m^3), the experimental drag torque is still greater than the predictions by a factor of two ($T_{exp} \sim 180$ N.mm versus $T_{pred} \sim 80$ N.mm).

A Couette flow approximation for the bearing drag torque over the bearing lands (assuming a uniform film thickness and non-slip BCs) gives

$$T_{Couette} \approx N_{pad} \cdot \left[\int_0^{\theta_l} \int_{R_i}^{R_o} \left\{ \left(\mu \frac{\partial U}{\partial z} \right) \cdot r \right\} dr r d\theta \right] \approx N_{pad} \cdot \left[\left(\frac{\mu \theta_{pad} \Omega}{4 h_{const}} \right) \left\{ R_o^4 - R_i^4 \right\} \right] \tag{51}$$

where the fluid viscosity is evaluated at $T_f = 330$ K according to Eq. (23) and the rest of the geometrical parameters are as defined in Table 15. Rearranging Eq. (51) determines a constant film thickness in the land section which produces the experimentally determined bearing drag torque, i.e.

$$h_{const} = N_{pad} \cdot \left[\left(\frac{\mu \theta_{pad} \Omega}{4 \cdot 0.18} \right) \left\{ R_o^4 - R_i^4 \right\} \right] = 2.27 \ \mu\text{m} \tag{52}$$

Eq. (52) predicts a constant film thickness on the order of the bearing combined (rotor plus pad) roughness [43] and is likely too small for actual operation. In addition, this analysis assumes that the entire land section operates with $h = h_{const}$ whereas predictions reveal a small film thickness at the pad edges with a (comparatively) large film at the pad center where the hydrodynamic pressure deforms the pad and mesh substructure.

Section 7.1 shows the current numerical model predicts well the static behavior (film thickness and bearing drag torque) of a foil thrust bearing. The differences between measurements and predictions, therefore, are attributed to a subtle difference between the prototype bearing (or testing) and the current analysis. As discussed in Chapter 5, the prototype bearing pads were likely all slightly different, creating an uneven load distribution over the bearing surface. This, coupled with depositions of MoS^2 on the surface of the thrust collar, could explain the increased drag torque in the experiments, as compared to the current predictions. However, the differences between the two sets of data is, as of yet, unascertained.

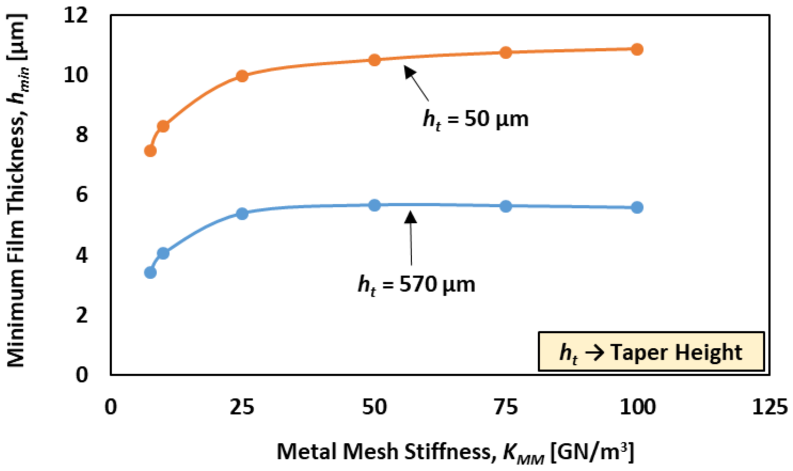

(a) Minimum film thickness

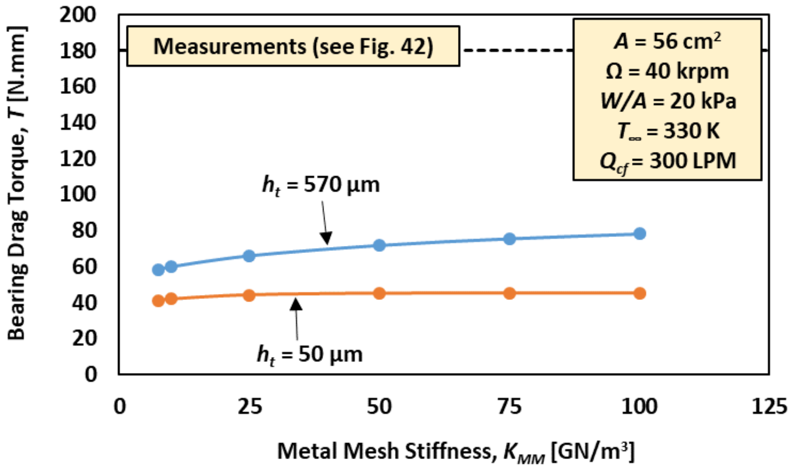

(b) Bearing drag torque

Figure 65. (a) Minimum film thickness and (b) bearing drag torque versus metal mesh stiffness per unit area (K_{MM}). Predictions for a six-pad MMFTB operating with Ω = 40 krpm, T_∞ = 330 K, W/A ~ 20 kPa, & Q_{cf} = 300 LPM.

7.3 STEADY-STATE PERFORMANCE PREDICTIONS FOR TWO DIFFERENT CIRCUMFERENTIALLY TAPERED FOIL THRUST BEARINGS

The following analysis compares the steady-state performance of a metal mesh foil thrust bearing (MMFTB) to that of a bump-type foil thrust bearing (BFTB) operating with a fast surface speed ($\omega \cdot R_{mid} \sim 279$ m/s), increasing load ($10 \leq W/A \leq 50$ kPa) and increasing amounts of cooling flow ($0 \leq Q_{cf} \leq 900$ LPM). Figure 66 displays schematics of a MMFTB pad and a BFTB pad incorporating “spacer blocks” at the pads leading edges. As described in Chapter 6, and displayed schematically in Figures 48 & 49, cooling flow supplies to the bearing through a feed hole at the bearing support center and flows radially outwards through the mixing areas between pads as well as under the pads. Figure 67 (displayed later) describes more the computational domain and thermal boundary conditions.

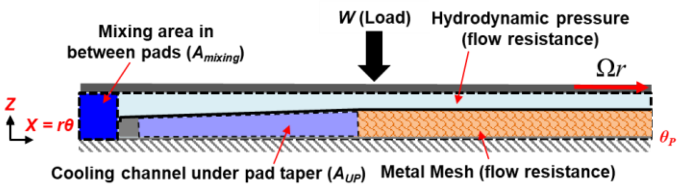

(a) MMFTB pad with a spacer block at the leading edge

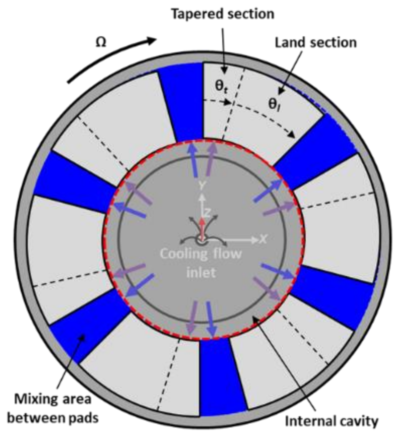

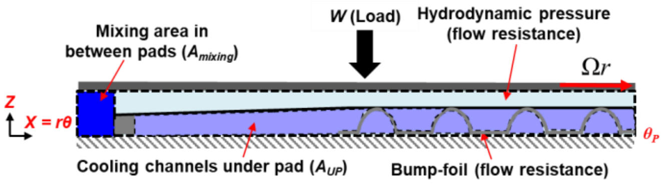

(b) BFTB pad with a spacer block at the leading edge

Figure 66. Schematics of a MMFTB pad and a BFTB pad incorporating spacer blocks at the pads leading edges.

Tables 16 & 17 list the MMFTB and BFTB geometries along with the operating conditions for the current analysis. Both bearings operate in an "open" environment such that the ambient temperature near the rotating collar remains at T_∞ = 310 K. As in Ref. [17] the rotor comprises of a central hub and a press fit aluminum thrust collar, whose thermal conductivity is an order of magnitude higher than traditional high temperature alloys (Inconel 718 for example).

Table 16. Geometry and material properties for a BFTB and a MMFTB.

	ROTOR COLLAR	**BEARING SUPPORT**
Material	Al 7075-T6	Inconel 718
Thermal Conductivity [W/(m.K)]	130	15.4
Inner & Outer Diameters [mm]	43, 101.6	45.72, 107.95
Thickness [mm]	12.7	6.35

	TOP FOIL PADS
Material	Inconel X-750
Elastic Modulus & Poisson's Ratio [GPa, -]	213, 0.29
Thermal Conductivity [W/(m.K)]	16.3
Inner & Outer Diameters [mm]	50.8, 101.6
Thickness [mm]	0.1524
Number of Pads [-]	6
Pad Arc Extent [°]	45
Taper Extent & Height[°,μm]	17, 50

Table 16 Continued. Geometry and material properties for a BFTB and a MMFTB.

	BFTB	MMFTB
Underspring Material	Inconel X-750	Copper
Effective Conductivity[a] [W/(m.K)]	8.0	0.20
Underspring Stiffness [GN/m^3]	13.5 – 32.5	8.76
Bump or Mesh Height [μm]	508	570
Number of Strips or Sheets [-]	5	3
Bumps/Strip or Openings/mm [-]	3, 3, 4, 5, 5	1.58
Strip Width [mm]	5.08	-
Bump Strip Mean Radii [mm]	28, 33, 38, 43, 48	-
Bump Pitches (ID to OD) [mm]	5.36, 5.77, 5.31, 4.52, 5.89	-
Bump Radius [mm]	1.6	-

[a] Closed-form expressions for effective thermal conductivity presented in Refs. [42,72].

Table 17. Operating conditions for a BFTB and a MMFTB.

Operating Conditions	
Ambient Pressure, P_a	101.4 [kPa]
Rotational Speed, Ω	70 [krpm]
Specific Load, W/A	10-50 [kPa]
Bearing Support & Ambient Temperatures, $T_{BS,\infty}$	310 [K]
Cooling Flow Rate, Q_{cf}	0 – 900 [LPM]
Cooing Flow Temperature, T_{cf}	290 [K]

Figure 67 displays a planar schematic of the computational domain indicating heat flows and thermal boundary conditions utilized in the current analysis. The compressible Reynolds equation determines the pressure (P) in the thin film while a bulk flow energy equation determines the film mean temperature (T). Simple mass and thermal energy balances determine the flows into and out of the internal cavity and mixing area between the bearing pads as well as the temperatures in both areas (T_{IC}, T_i). Heat from the thin film convects to the thrust collar and top foil surfaces where energy equations (with appropriate convection or conduction boundary conditions) determine the respective solids temperature (T_{TC}, T_{tf}).

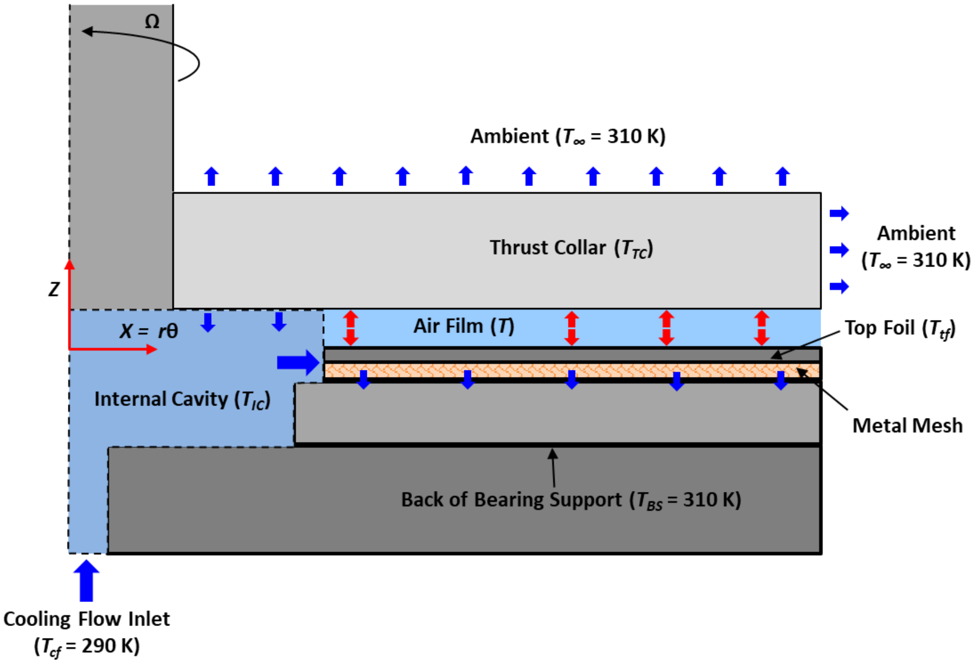

Figure 67. Schematic of a metal mesh foil thrust bearing indicating heat flows and thermal boundary conditions for the current analysis.

Figure 68 displays the mass flow rates through the pad boundaries ($\dot{m}_i$, $\dot{m}_{leak,ID}$, $\dot{m}_{leak,OD}$, and $\dot{m}_e$) for a MMFTB and a BFTB with dimensions as displayed in Table 16 operating at a high surface speed ($\omega \cdot R_{mid}$ ~ 279 m/s), a large specific load (W/A = 50 kPa), and no forced cooling flow. In the following figure, note that positive flow indicates flow entering the pad, while negative flow represents that leaving the domain. A summation of flows through the pad boundaries $\sum \dot{m} \approx 0$, showing continuity is maintained. Most of the flow makes its way along the length of the bearing pad and out the trailing edge. Of the flow that exits through the sides of the pad, the majority exits through the pad OD, and before the land section. As the pressure (and film thickness) fields are similar between the MMFTB and BFTB, the flows through the boundaries of both pads are quantitatively and qualitatively similar. Note that the amount of flow leaking into the internal cavity ($\dot{m}_{leak,ID}$) is inversely proportional to the collar speed (not shown for brevity).

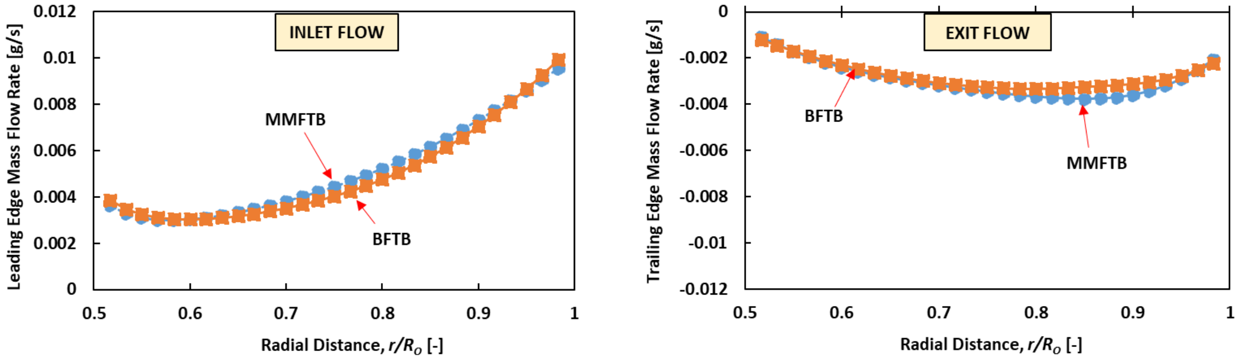

(a) Flow through pad leading edge $\left(\dot{m}_i\right)$ (b) Flow through pad trailing edge $\left(\dot{m}_e\right)$

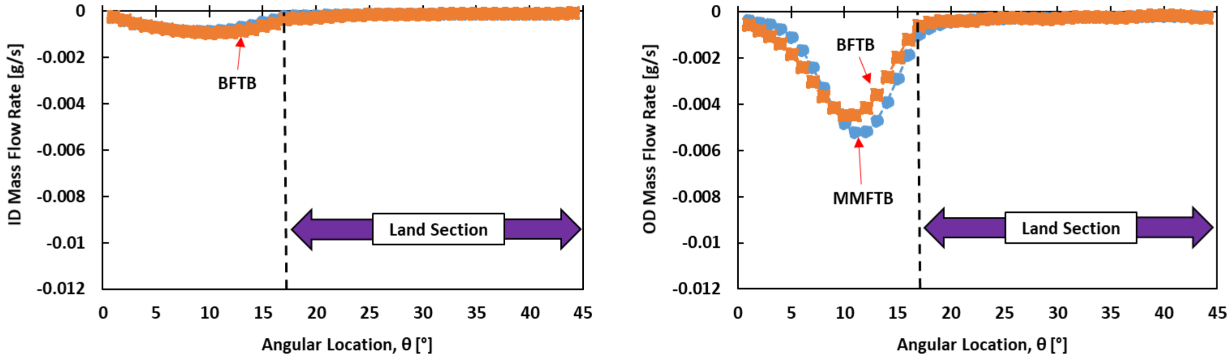

(c) Flow through pad ID $\left(\dot{m}_{leak,ID}\right)$ (d) Flow through pad OD $\left(\dot{m}_{leak,OD}\right)$

Figure 68. Air mass flow rates through the boundaries of a typical pad with dimensions as displayed in Table 16. *W/A* = 50 kPa, Ω = 70 krpm & T_∞ = 310 K.

Figures 69-71 display contour plots of the film thickness, pressure and temperature rise (T-T_{cf}) for a MMFTB and a BFTB with dimensions as displayed in Table 16 and operating with Ω = 70 krpm ($\omega \cdot R_{mid} \sim 279$ m/s), increasing specific load $10 \leq W/A \leq 50$ kPa, and a moderate cooling flow rate Q_{cf} = 300 LPM. Note that the maximum Reynolds number Re ~ 1,200 even for this high speed, denoting flow well within the laminar regime. At the lowest load (10 kPa) the film pressure is low and does not deform the pad much, such that the film thickness decreases linearly from the pad leading edge to the taper/land transition, where it reaches a minimum and is then relatively uniform to the trailing edge. At W/A = 10 kPa, the peak pressure locates at the transition between the taper and land sections, while both the land and the tapered sections contribute to the bearing reaction load (i.e. $P > P_a$). The surface speed increases from the pad inner to outer diameter, yielding a maximum fluid temperature near the pad OD and in the land section where the film thickness is small (i.e. fluid shear is large).

As the specific load increases, the peak pressure locates further downstream of the taper/land transition, and for the BFTB and largest load case, locates directly above the bump crests, where the film thickness is the smallest. In addition, top foil elastic deflections in the tapered section of the pad, where the is no underspring support, increases the local film thickness, which reaches a maximum near the pad midspan and ~12 degrees from the pad leading edge. For loads of 30 kPa and higher, the fluid film mean temperature exhibits local cool spots directly above the bump crests, where heat conducts from the backside of the foil through the bump foil and to the bearing support, which acts as a heat sink. Interestingly, at the highest load, top foil sagging occurs near the trailing edge, between the penultimate and final bumps, leading to a slight diverging zone and a less uniform distribution of the film pressure.

The film thickness, hydrodynamic pressure, and film temperature for the MMFTB are very similar to those exhibited by the BFTB at W/A = 10 kPa. Comparing the two sets of predictions, the peak pressure for the MMFTB locates at the taper/land transition, and near the pad midspan, as with the BFTB. The film temperature has its maximum near the pad OD and in the land, where the fluid shear is the largest. Recall that the cooling flow underneath the pad increases the heat transfer from the foil in the case of the BFTB, whereas no cooling flow applies to the land section of the MMFTB as the mesh sheets are dense and prevent flow (see Figure 66). As such, the BFTB operates slightly cooler (~ 5 K) than the MMFTB for all three loads. At W/A = 25 & 50 kPa, the pressure in the land section is relatively uniform. Comparing the film thickness between the MMFTB and BFTB at higher loads, the BFTB has a small film thickness directly above the bump crests, whereas the MMFTB has a slightly larger film thickness which is relatively uniform over the entire land section and reaches a minim near the pad edges.

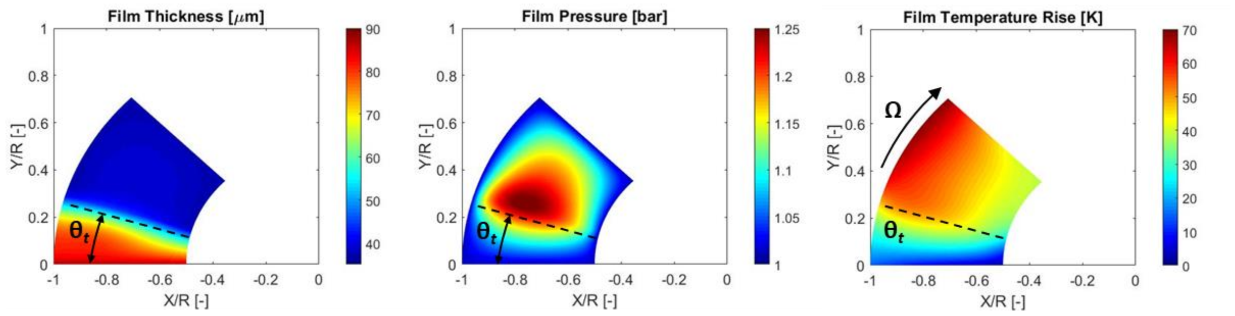

(a) Metal mesh foil thrust bearing (*W/A* = 10 kPa)

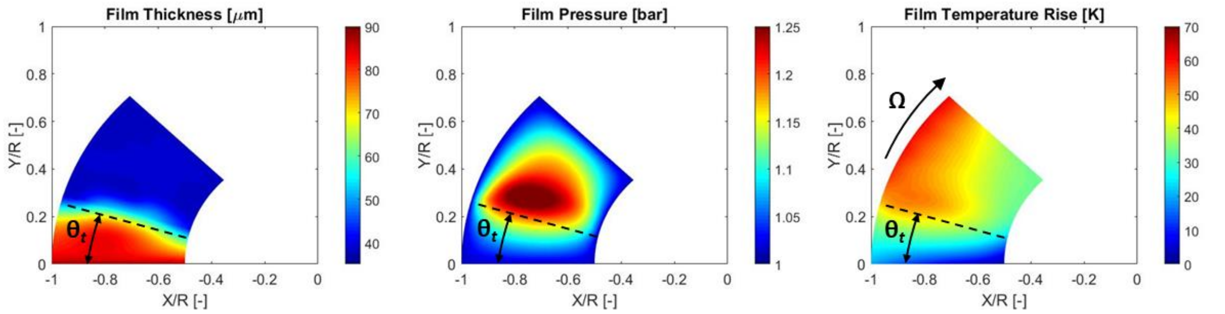

(b) Bump-foil thrust bearing (*W/A* = 10 kPa)

Figure 69. Contour plots of film thickness, pressure and temperature for a six-pad MMFTB and a BFTB operating with geometry and operating conditions as displayed in Tables 14 & 15. *W/A* = 10 kPa, Q_{cf} = 300 LPM.

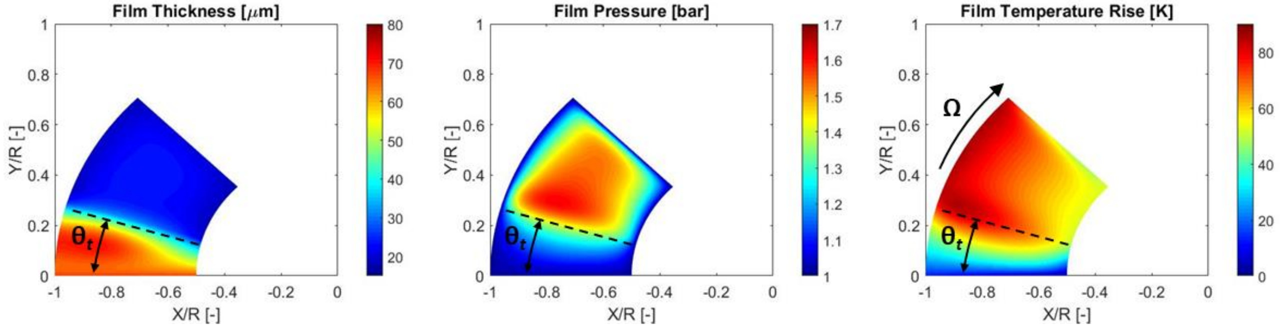

(a) Metal mesh foil thrust bearing (*W/A* = 30 kPa)

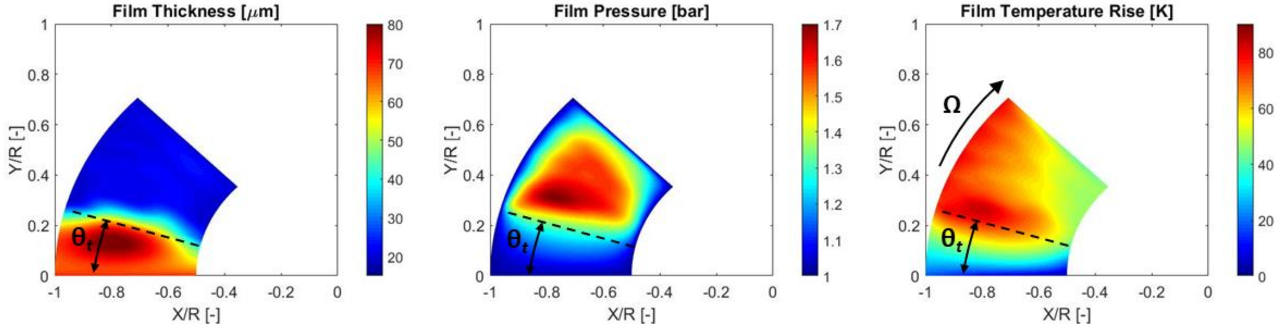

(b) Bump-foil thrust bearing (*W/A* = 30 kPa)

Figure 70. Contour plots of film thickness, pressure and temperature for a six-pad MMFTB and a BFTB operating with geometry and operating conditions as displayed in Tables 14 & 15. *W/A* = 30 kPa, Q_{cf} = 300 LPM.

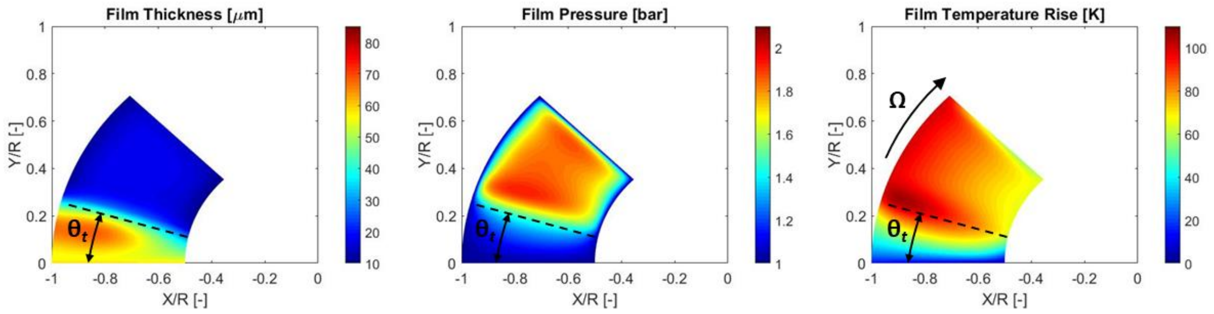

(a) Metal mesh foil thrust bearing (*W/A* = 50 kPa)

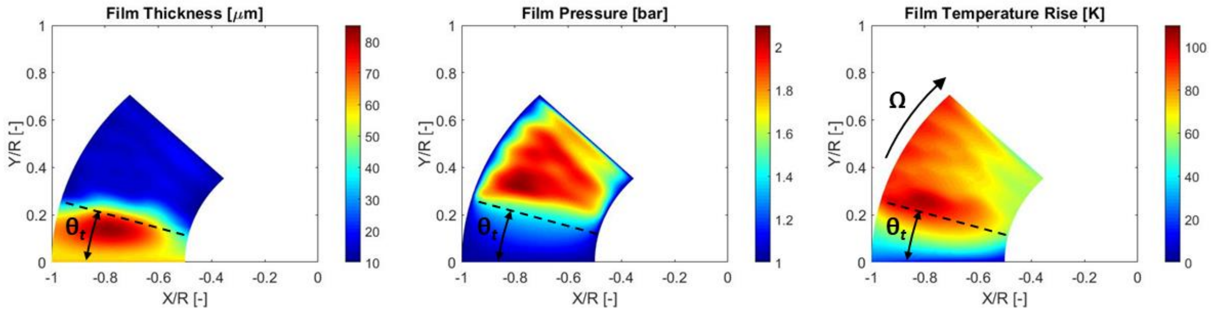

(b) Bump-foil thrust bearing (*W/A* = 50 kPa)

Figure 71. Contour plots of film thickness, pressure and temperature for a six-pad MMFTB and a BFTB operating with geometry and operating conditions as displayed in Tables 14 & 15. *W/A* = 50 kPa, Q_{cf} = 300 LPM.

The contour plots in Figures 69-71 show that the peak pressure and film temperature reach maximums near the pad OD. Figure 72 investigates the local field variables over a bearing pad at a constant radius of R = 43.1 mm (R/R_O = 0.85) and from the pad lead to trailing edge

($0 \le \theta \le 45°$). Note that the specific load W/A = 50 kPa, the rotor speed Ω = 70 krpm, and the cooling flow Q_{cf} = 300 LPM. Referring first to the BFTB performance, the hydrodynamic pressure in the lubricated zone is not uniform, dipping as the top foil sags between bumps. In contrast, the pressure over the MMFTB pad is relatively uniform, as is the film thickness and the foil deformation. For the same applied load (W/A = 50 kPa), the MMFTB has a smaller peak pressure along R = 43.1 mm due to more uniform, smaller film thickness.

In the tapered sections of both the MMFTB and BFTB, the film temperature is noticeably higher than that of the bounding solids (thrust collar & top foil). Large film thicknesses in the tapered sections lead to small heat convection coefficients in the tapered portions ($\bar{h}_{TC}, \bar{h}_{tf} \sim 1{,}000\ \mathrm{W/m^2K}$) when compared to those in the land sections ($\bar{h}_{TC}, \bar{h}_{tf} \sim 3{,}000\ \mathrm{W/m^2K}$). Overall, the BFTB has a higher peak temperature at R = 43.1 mm but operates cooler than the MMFTB in the land section, as the cooling flow underneath the pad significantly increases the heat transfer from the backside of the foil. Figure 75 (displayed later) shows film and bounding solids temperature rises versus angular location for increasing amounts of cooling flow.

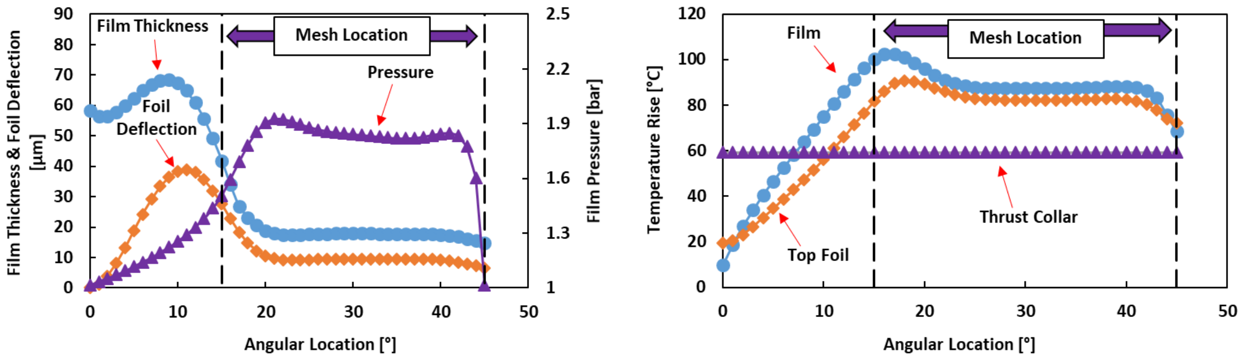

(a) MMFTB

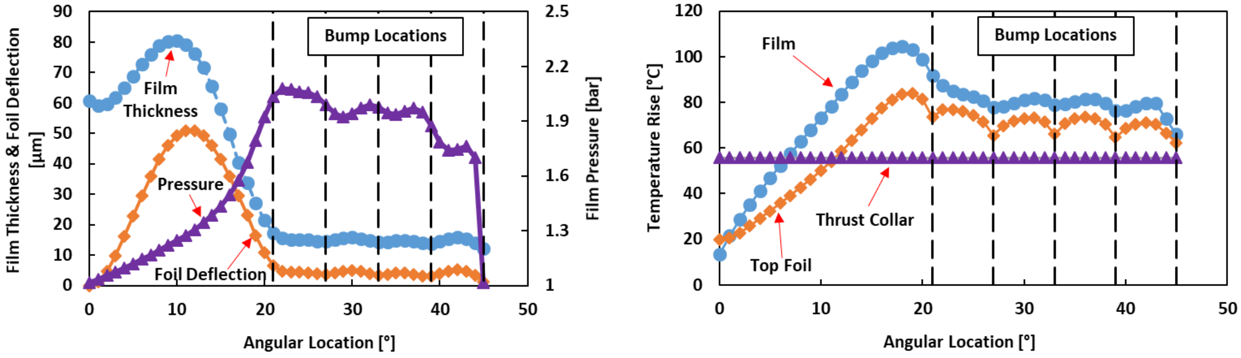

(b) BFTB

Figure 72. Field variables versus angular location for two six-pad compliant foil thrust bearings at a constant radius (R = 43.1). W/A = 50 kPa, Ω = 70 krpm & Q_{cf} = 300 LPM.

Figure 73 displays contours of the Knudsen numbers in the flow domain for a MMFTB and a BFTB operating at Ω = 70 krpm, a specific load W/A = 50 kPa and Q_{cf} = 300 LPM. The Knudsen number compares the fluid mean flow path to the local film thickness (Kn = λ/h). The mean flow path of air at standard conditions λ_a ~ 68 nm [16]. Referring to Eq. (17), this mean flow path is a function of the fluid temperature, viscosity and pressure. Figure 73 shows that the MMFTB and

BFTB operate with Kn ≤ 0.004 over the majority of their pads, indicating the flow is representative of a continuum. The max Knudsen number $\mathrm{Kn}_{\max}$ ~ 0.008 for both bearings near the pads inner and outer radii and in the land regions where the film pressure and film thickness are the smallest. For bearings near their load capacity, note that the film thickness in the middle of the land region is h ~ 5 μm with a corresponding Knudsen number in excess of Kn ≥ 0.01.

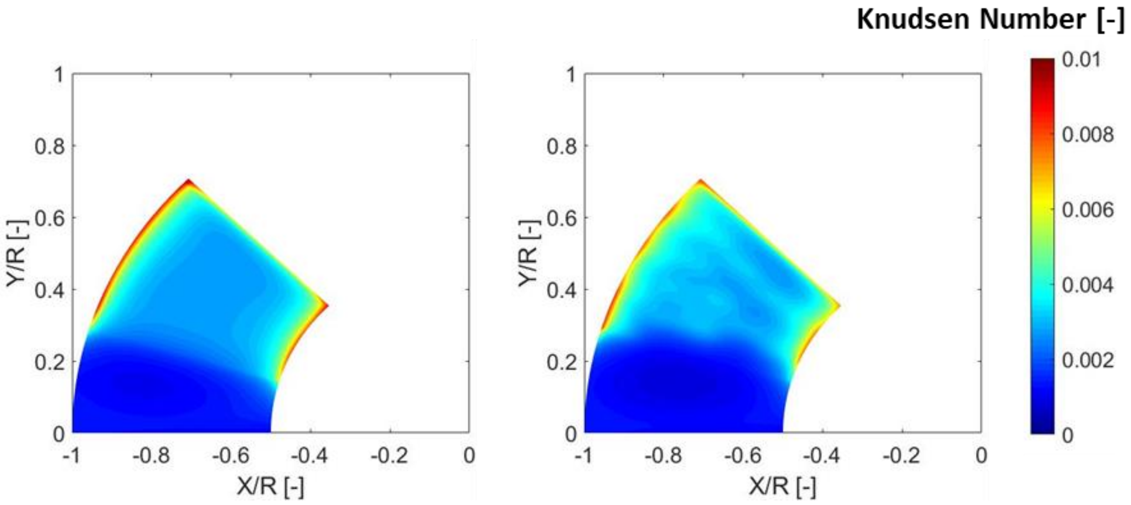

(a) MMFTB (b) BFTB

Figure 73. Contour plots of Knudsen Number for a (a) metal mesh & (b) bump-type foil thrust bearing. W/A = 50 kPa, Ω = 70 krpm, and Q_{cf} = 300 LPM.

Figure 74 displays contours of the thrust collar temperature operating at Ω = 70 krpm, a specific load W/A = 50 kPa and Q_{cf} = 300 LPM. Recall that the current model assumes a constant thrust collar temperature in the circumferential direction, such its temperature only varies radially and through the thickness. Heat adds to the thrust collar at its bottom surface (Z/Z_{TC} = 0) and convects to atmosphere (T_∞ = 310 K) on the collar OD (R/R_{TC} = 1) and back surface (Z/Z_{TC} = 1). The plots show a maximum temperature at bottom surface and at the collar OD, where the surface speed is the highest, and as the previous contours have shown, the film temperature is also the highest. Predictions show that the entire collar operates well above the cooling flow temperature, ΔT_{TC} ~ 57 & 53 K for the MMFTB and BFTB, respectively. Importantly, utilizing a thrust collar with a high thermal conductivity (κ_{TC} = 130 W/m.K) creates a relatively uniform temperature through its thickness, and also in the radial direction for all of the predictions. As noted in Refs. [17-19, 41 & 42], thermal bending of the collar away from the bearing increases the film thickness and limits load carrying capacity. As such, the predictions displayed in Figure 74 advocate implementing a thrust collar with a higher thermal conductivity (like Al 7075-T6) to prevent large thermal gradients and subsequent thermal-elastic deformations.

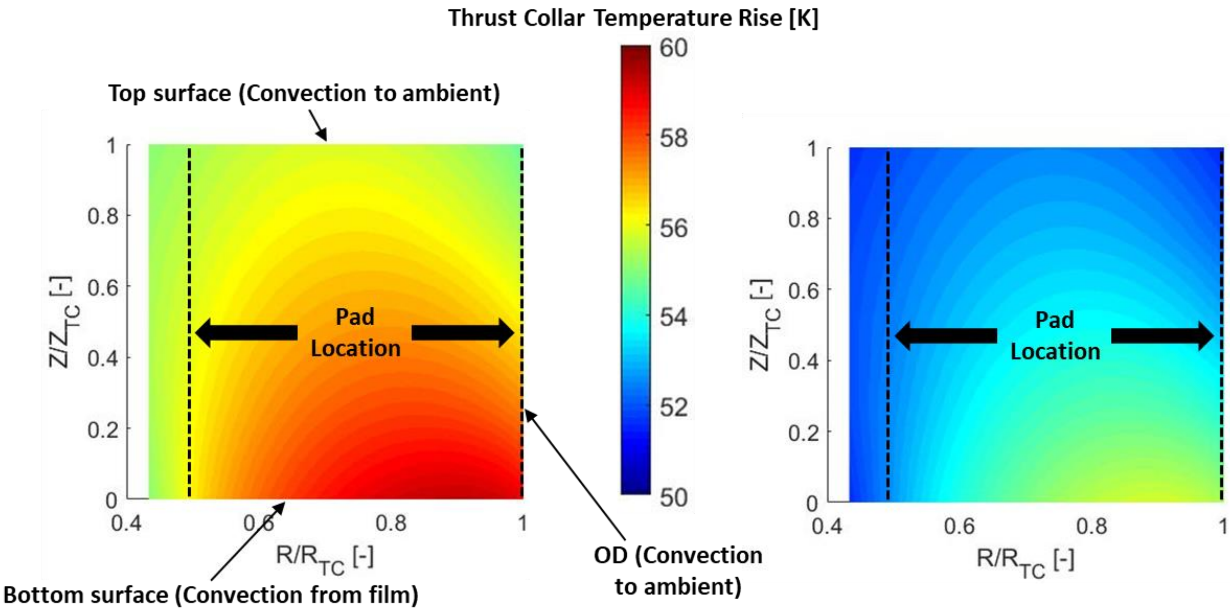

(a) MMFTB (b) BFTB

Figure 74. Contour plots of thrust collar temperature rise for a (a) metal mesh & (b) bump-type foil thrust bearing. W/A = 50 kPa, Ω = 70 krpm, and Q_{cf} = 300 LPM.

Figure 75 displays the steady-state performance (minimum film thickness, bearing power loss and fluid/solid temperature rises) of the two bearings versus specific load for a collar operating at a high surface speed ($\omega \cdot R_{mid} \leq 279$ m/s) and with a moderate cooling flow supply (Q_{cf} = 300 LPM). The predictions show that the two bearings operate with nearly the same minimum film thickness at low loads, with the BFTB h_{min} approximately 1.5 μm larger than that of the MMFTB for loads in excess of W/A = 30 kPa. Despite having a marginally larger minimum film thickness, the BFTB power loss closely resembles that of the MMFTB. The main difference between the two bearings is seen in the thermal performance, with the BFTB foil temperature ~ 10 °C cooler than that of the MMFTB for all loads.

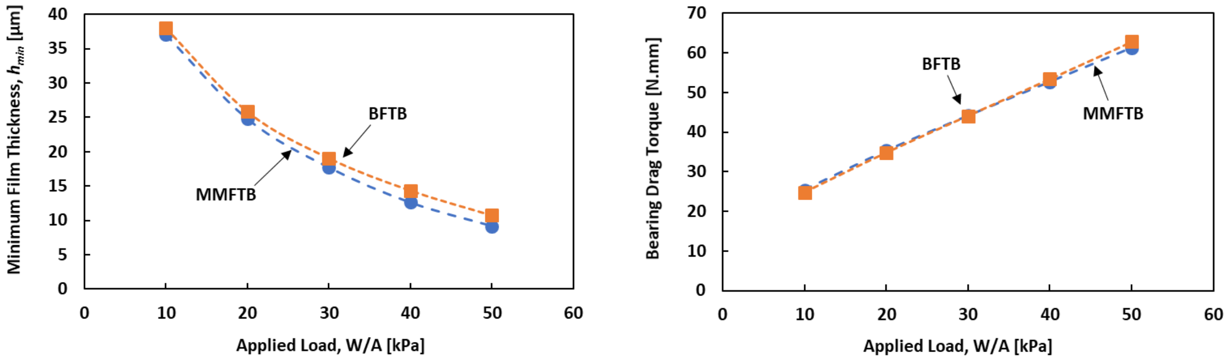

(a) Minimum Film Thickness (b) Bearing Drag Torque

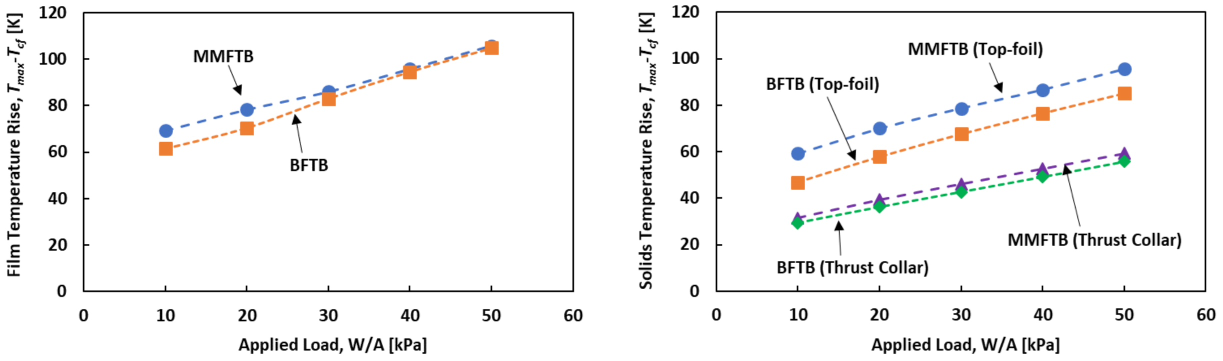

(c) Film Temperature Rise (d) Top-Foil & Thrust Collar Temperature Rise

Figure 75. Steady-state performance of two six-pad foil thrust bearings operating with Ω = 70 krpm and Q_{cf} = 300 LPM.

Figure 76 displays film, top-foil and thrust collar temperature rise ($T - T_{cf}$) versus angular location at a constant radius (R = 43.1 mm) for a MMFTB and a BFTB operating with a modest load (W/A = 30 kPa), a large surface speed ($\omega \cdot R$ ~ 316 m/s), and increasing amounts of cooling flow ($0 \leq Q_{cf} \leq 900$ LPM). When no cooling flow applies to the bearing, the film inlet temperature is large (T ~ 345 K) for both bearings, with the BFTB displaying a slightly higher peak film temperature. With no cooling flow, the top-foil and film temperatures are similar, especially in the tapered sections, where convection from the backside of the foil is limited to natural convection ($\bar{h}_{tf,back} \sim 10$ W/m^{2}K). In addition, the thrust collar temperature is significantly lower than the film (and top-foil) temperature, such that most of the heat from the film transfers to the collar surface, conducting through its thickness, and convecting to ambient (T_∞ = 310 K) at the collar backside and outer diameter.

Applying cooling flow through the bearing center decreases the film inlet temperature for both bearings, with the inlet flow temperature approaching that of the cooling flow inlet (T_{cf} = 290 K) for large amounts of flow (Q_{cf} = 900 LPM). Predictions show the top-foil temperature decreasing dramatically with increasing flow, creating a temperature difference between the film and the foil and facilitating more heat transfer to the thin foil. Comparing the temperature profiles of the MMFTB and the BFTB, the BFTB foil temperature decreases more than that of the MMFTB. As mentioned earlier, the BFTB design allows cooling flow to remove heat under the entire pad, whereas the mesh structure for the MMFTB does not permit cooling flow in the land section, where the film thickness is the smallest and heat generation is the greatest.

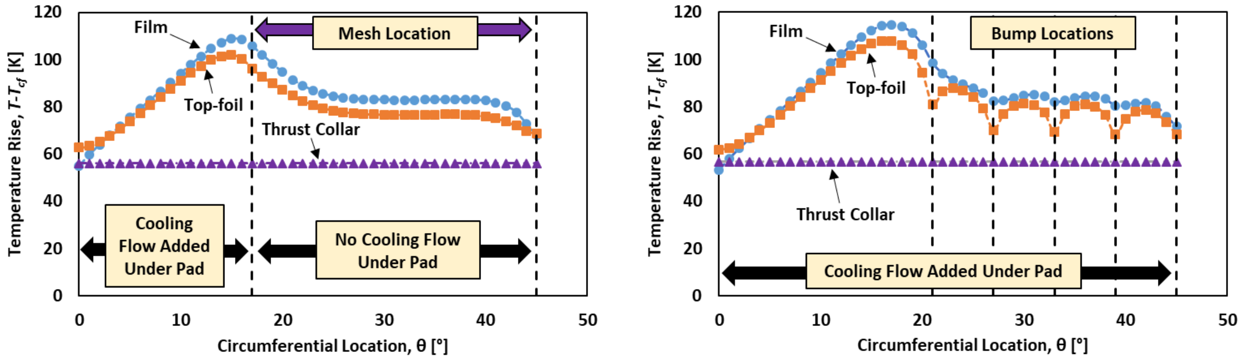

(a) MMFTB (Q_{cf} = 0 LPM)

(b) BFTB (Q_{cf} = 0 LPM)

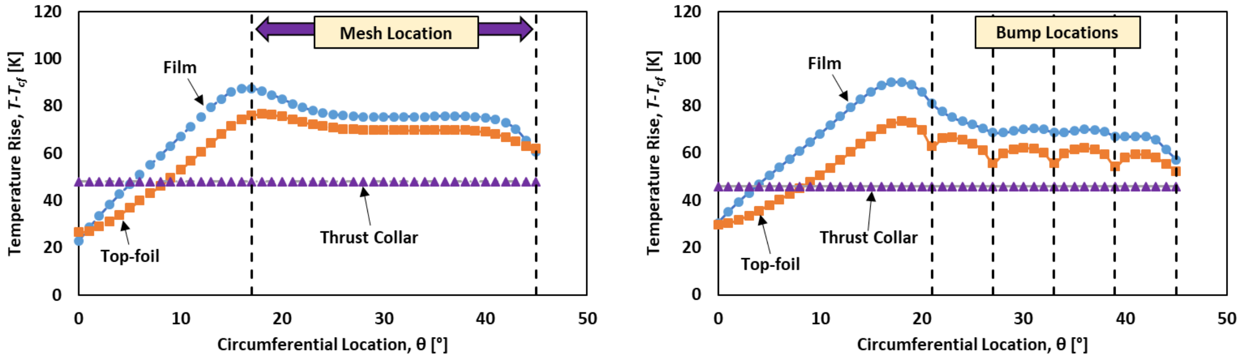

(c) MMFTB (Q_{cf} = 100 LPM)

(d) BFTB (Q_{cf} = 100 LPM)

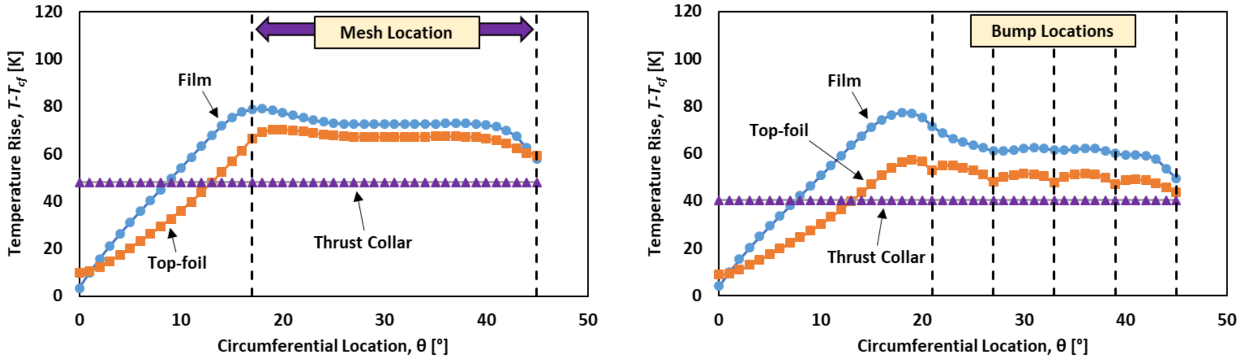

(e) MMFTB (Q_{cf} = 900 LPM)

(f) BFTB (Q_{cf} = 900 LPM)

Figure 76. Film, top-foil and thrust collar temperature rise versus angular location for two six-pad compliant foil thrust bearings at a constant radius (*R* = 43.1). *W/A* = 30 kPa & Ω = 70 krpm.

Figure 77 displays the steady-state performance (minimum film thickness, bearing drag torque and fluid/solid temperature rises) of the two bearings versus cooling flow rate for a modest load (W/A = 30 kPa) and a large surface speed ($\omega \cdot R_{mid} \leq 279$ m/s). Predictions show that the minimum film thickness and bearing drag torque are largely unaffected by increasing the amount of cooling flow supplied to the bearing. This finding is in-line with the measurements displayed in Figure 31 for a single-pad MMFTB. The peak film temperatures for both bearings (as well as the peak temperatures of the top-foil and thrust collar) decrease with increasing cooling flow rate, with the BFTB showing a greater decrease (~ 40 K) over the cooling flow rate range ($0 \leq Q_{cf} \leq 900$ LPM). The mesh in the land section obstructs cooling flow and limits the cooling effectiveness for the MMFTB, hence showing little temperature decrease with increasing cooling flow (after a point).

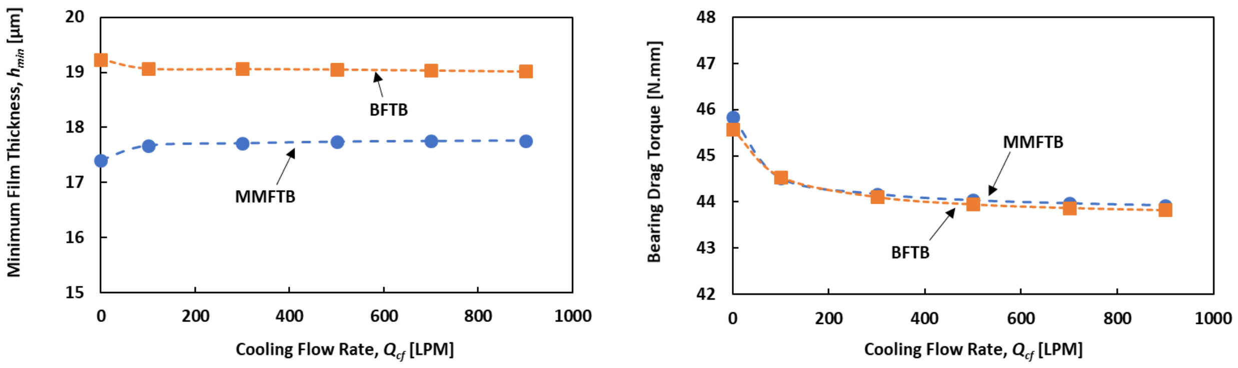

(a) Minimum Film Thickness (b) Bearing Drag Torque

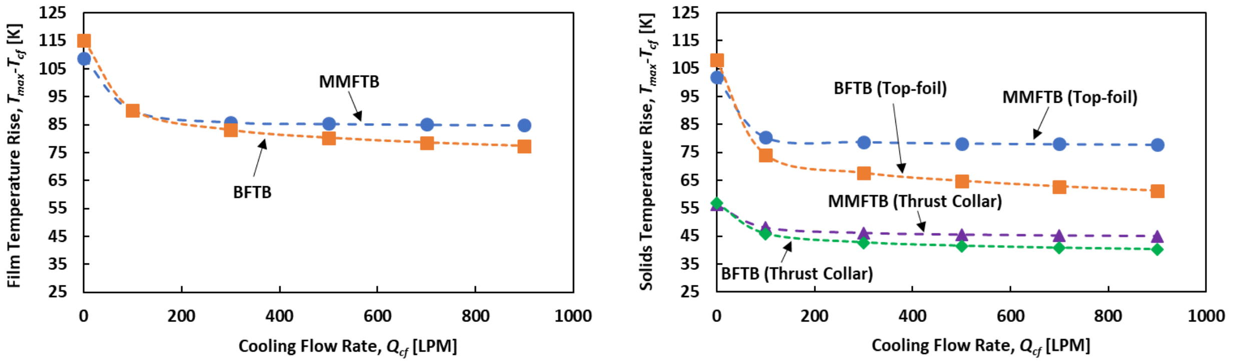

(c) Film Temperature Rise (d) Top-foil & Thrust Collar Temperature Rise

Figure 77. Steady-state performance of two six-pad foil thrust bearings operating with Ω = 70 krpm and *W/A* = 30 kPa.

Predictions with the two compliant surface bearings show that a MMFTB with a relatively stiff mesh (K_{MM}/A_{land} = 8.76 GN/m^3) has a similar steady-state performance to that of a BFTB. The bearing drag torque between the two bearings is nearly identical for a rotor operating at Ω = 70 krpm ($\omega \cdot R_{mid}$ = 279 m/s) applied loads from $10 \leq W/A \leq 50$ kPa and cooling flow rates between $0 \leq Q_{cf} \leq 900$ LPM. Applying cooling flow to the bearing from the pad ID to OD can decrease the film and bounding solid temperatures by more than 45 K, even when the bearing operates with a large rotor speed ($\omega \cdot R_{mid}$ ~ 279 m/s) and a large load (W/A = 50 kPa). Predictions show a small amount of cooling flow (Q_{cf} ~ 100 LPM) decreasing the film and pad temperatures dramatically. In the current model, after Q_{cf} ~ 100 LPM, the MMFTB design (incorporating a dense mesh in the land section under the pad which obstructs cooling flow) limits the bearing cooling effectiveness. Experiments with both bearings are necessary to validate fully the model presented herein and elucidate any potential of a MMFTB.

8. SUMMARY AND CONCLUSIONS

Modern commercial micro-turbomachinery (less than 400 kW) would benefit from low cost, reliable foil thrust bearings. Bump-type foil bearings, while utilized in many commercial applications, rely on a corrugated bump foil structure which requires engineering experience and expertise to design and implement. Metal mesh sheets offer a cheap, and readily available alternative to bump-type foils with a comparable structural stiffness and material damping [3].

The dissertation presents first the concept and manufacture of a novel Rayleigh-step foil thrust bearing, supported by a compliant metal mesh structure. The Rayleigh-step bearing has three components, a thin top foil segmented into six identical arcuate pads, a circular layer (or layers) of copper metal mesh, and a solid steel bearing support. Due to the small thickness of the top foil (t_{tf} ~ 1.016 mm), a photo-chemical etching process forms the steps on each of its pads, while a very thin (~5 μm) coating applies to the entire foil.

Along with the novel bearing, the dissertation details the design of a simple, electric motor driven test rig for hydrodynamic foil thrust bearings. The test rig is capable of rotor collar speeds up to 40 krpm, static loads up to 580 N and dynamic loads up to 100 N. The rig includes the ability to measure bearing drag torque, applied load (static and dynamic), and relative displacement between the rotor collar and test bearing. Measurements of bearing relative displacement and applied dynamic load facilitate the determination of bearing axial force coefficients (stiffness and damping) for static conditions (no rotor speed) and during operation with rotation. In addition, the rig design allows for cooling flow (up to 300 SLPM) to the test bearing surface.

After proving the bearing concept with an incompressible fluid, a rotational speed test ($\Omega = 40$ krpm & $W/A < 5$ kPa) with ambient air as the working fluid failed multiple prototype Rayleigh-step top foils. As the test rig was properly aligned before testing (and verified afterwards), the failures are attributed to the inherent waviness of the copper mesh support structure. This waviness bulged the top foil towards the rotor collar, forcing premature contact during the initial loading phase, before hydrodynamic pressure built on the pad's surfaces. The failure of the Rayleigh-step top foil showed that the thin (5 μm) sacrificial coating (Korlon®) on the foil did little to protect the bearing, pointing to the need for a robust coating for foil bearings to withstand intermittent contact during start-up and shut-down.

A redesigned metal mesh foil thrust bearing, incorporating a circumferential taper, operated successfully with a single pad, a rotor collar speed of Ω = 40 krpm and loads $7 \le W/A \le 35$ kPa. Measurements with the single-pad bearing determined a bearing drag torque which increases linearly with applied load, and that is largely unaffected by applied cooling flow (from 100 to 300 SLPM). After tests with the single-pad bearing, tests with a full six-pad MMFTB proved the bearing concept to a moderate specific load $W/A \sim 25$ kPa. Under-pad temperature measurements for the six-pad bearing show that the bearing pads were not evenly loaded, despite the uniform nature of the mesh, with one pad running 20 °C cooler than the temperatures of the other two measured pads. These results show that, while care was taken to acquire consistent mesh (similar dimensions and weight per square meter), the inherent waviness of the mesh creates different pad taper heights, which loads some pads more than others, and ultimately limited the load carrying capacity of the prototype bearing. Unfortunately, further tests with rotor speed and the prototype bearing failed the test rig after, pointing to a poor initial design, which coupled the heavy thrust collar directly to the router motor via a collet and nut. A redesign of the thrust bearing test rig should incorporate an intermediate shaft and housing to adequately support the rotor collar, as implemented in serval instances in the literature [10,11,17-19].

Predictions made with a thermo-elastohydordynamic model compare well to experimental data for gas lubricated thrust bearings [9] as well as predictions from models which utilize complex bump-foil models and commercial software [42,63]. Despite the validity of the current model, predicted bearing drag torque differs significantly (by ~ a factor of two) from that measured for a six-pad MMFTB. A simple Couette flow approximation for the bearing drag torque reveals a minute film thickness (h_{cont} = 2.7 μm) which produces the measured bearing drag torque (T_{exp} = 180 N.mm) at the highest applied load (W/A = 25 kPa). A minimum film thickness less than 3 μm likely incurs bearing operation in the mixed-lubrication regime. As such, the differences between measurements and predictions are currently attributed to non-uniformity between bearing pads in the prototype bearing as well as (possible) continuous sliding contact between depositions of solid lubricant (MoS_2) on the thrust collar surface and the bearing pads.

Due to a failure of the test rig, a further analysis of the MMFTB utilizes the current model to compare predicted steady-state performance of a MMFTB to that of a BFTB. The comparison shows that the MMFTB and BFTB have a nearly identical drag torque for applied loads comprised between $10 \leq W/A \leq 50$ kPa and for $\Omega = 70$ krpm ($\omega \cdot R_{mid} \sim 279$ m/s) and cooling flows $0 \leq Q_{cf} \leq 900$ LPM. In addition, the MMFTB has a slightly smaller film thickness, and thus, likely a slightly lower load capacity.

For a given bearing geometry, predictions reveal a cooling flow rate (~ 100 LPM) which fully saturates the pad leading edge, such that the bearing draws no fluid from ambient at the OD. Applying cooling flow to the bearing through the ID decreases the film and foil peak temperatures by ~ 40 K, and the collar peak temperature by ~ 10 K for flows up to 900 LPM. Inserting more than 100 LPM of cooling flow decreases the film temperature little, as the pad area in the tapered section is small (limiting convection from the foil backside to the cooling flow). The BFTB has a slightly more effective cooling, as cooling flow distributes to both the taper and land sections beneath the pad, whereas the compact mesh in a MMFTB prohibits air flow underneath the pad in the land section. Importantly, utilizing an aluminum collar (κ_{TC} = 130 W/m.K) results in a relatively constant collar temperature through its thickness, even for a relatively high rotor speed ($\omega \cdot R_{mid}$ = 279 m/s) and modest specific load (W/A = 30 kPa).

The dissertation contributes a novel Rayleigh-step compliant surface foil thrust bearing supported by metal mesh sheets. The failure of multiple prototype top foils points to the need of a robust coating on the top foil, which likely prohibits the use of etched foils in compliant surface thrust bearings. While tests do show that the inexpensive mesh substructure provides a structural stiffness and material damping similar to that of a bump-type foil, difficulties and trials throughout the testing process show that even the circumferentially tapered design is not adequate for commercial implementation.

A more successful MMFTB must ensure similar taper heights between individual pads to ensure an even distribution of the imposed thrust load. A future improvement could implement spacer bars as in Ref. [42] to more evenly distribute the load between the taper and land sections on the bearing pads and control the pads taper heights. Predictions do show that a foil thrust bearing, implementing a uniformly distributed underspring structure and spacer bars, yields a similar steady-state performance to that of the widely used bump-type foil thrust bearing. However, the issues listed above must be rectified, and overcome, if a MMFTB is to be implemented in commercial applications.

REFERENCES

[1] Blok, H. and van Rossum, J. J., 1953, “The Foil Bearing – A New Departure In Hydrodynamic Lubrication,” Lubr. Eng., December, pp. 316-320.

[2] Zarzour, M. and Vance, J., 2000, “Experimental Evaluation of a Metal Mesh Bearing Damper,” ASME J. Eng. Gas Turbines Power, **122**, pp. 1-4.

[3] San Andrés, L. and Chirathadam, 2012, “A Metal Mesh Foil Bearing and a Bump-Type Foil Bearing: Comparison of Performance of Two Similar Size Gas Bearings,” ASME J. Eng. Gas Turbines Power, **134**, pp. 1-13.

[4] San Andres, L., Ryu, K. and Diemer, P., 2015, “Prediction of Gas Thrust Foil Bearing Performance for Oil-Free Automotive Turbochargers,” ASME J. Eng. Gas Turbines Power, **137**, pp. 1-10.

[5] De Santiago, O. and Solórzano, V., 2013, “Experiments with Scaled Foil Bearings in a Test Compressor Rotor,” Proc. ASME Turbo Expo, San Antonio, Texas, USA, GT2013-94087, pp. 1-8.

[6] Ertas, B.H., 2009, “Compliant Hybrid Journal Bearings Using Integral Wire Mesh Dampers,” ASME J. Eng. Gas Turbines Power, **131**, pp. 1-11.

[7] Delgado, A., 2015, “Experimental Identification of Dynamic Force Coefficients for a 110 MM Compliantly Damped Hybrid Gas Bearing,” ASME J. Eng. Gas Turbines Power, **137**, pp. 1-8.

[8] Dykas, B., Prahl, J., DellaCorte, C. and Bruckner, R., 2006, “Thermal Management Phenomena in Foil Gas Thrust Bearings,” Proc. ASME Turbo Expo, Barcelona, Spain, GT2006-91268, pp. 1-7.

[9] Dykas, B., Bruckner, R., DellaCorte, C., Edmonds, B. and Prahl, J., 2009, “Design, Fabrication, and Performance of Foil Gas Thrust Bearings for Microturbomachinery Applications,” ASME J. Eng. Gas Turbines Power, **131**, pp. 1-8.

[10] Balducchi, F., Arghir, M., Gauthier, R. and Renard, E., 2013, “Experimental Analysis of the Start-Up Torque of a Mildly Loaded Foil Thrust Bearing,” ASME J. Trib., **135**, pp. 1-7.

[11] Balducchi, F., Arghir, M. and Gauthier, R., 2015, “Experimental Analysis of the Dynamic Characteristics of a Foil Thrust Bearing,” ASME J. Trib., **137**, pp. 1-9.

[12] Heshmat, H, Walowit, J.a. and Pinkus, O., 1983, “Analysis of Gas Lubricated Compliant Thrust Bearings,” ASME J. Lub. Tech., **105**, pp. 638-646.

[13] Heshmat, H., 1991, “Analysis of Compliant Foil Bearings with Spatially Variable Stiffness”, AIAA/ SAE/ ASME/ ASEE 27th Joint Propulsion Conference, AIAA-91-2102.

[14] Roger Ku, C. P., 1994, “Dynamic Structural Properties of Compliant Foil Thrust Bearing – Comparison Between Experiment and Theoretical Results”, ASME J. Trib, **116**, pp.70-75.

[15] Iordanoff, I., 1999, “Analysis of an Aerodynamic Compliant Foil Thrust Bearing: Method for a Rapid Design,” ASME J. Trib, **121**, pp. 816-821.

[16] Bruckner, R. J., 2004, “Simulation and Modeling of the Hydrodynamic, Thermal and Structural Behavior of Foil Thrust Bearings,” PhD Dissertation, Case Western Reserve University, Cleveland, OH.

[17] Dykas, B., 2006, “Factors Influencing the Performance of Foil Gas Thrust Bearings for Oil-Free Turbomachinery Applications”, PhD Dissertation, Case Western Reserve University.

[18] Dickman, J.R., 2010, “An Investigation of Gas Foil Thrust Bearing Performance and its Influencing Factors,” MS Thesis, Case Western Reserve University, Cleveland, OH.

[19] Stahl, B.J., 2012, “Thermal Stability and Performance of Foil Thrust Bearings,” MS Thesis, Case Western Reserve University, Cleveland, OH.

[20] Bruckner, R.J., 2012, “Performance of Simple Gas Foil Thrust Bearings in Air,” NASA/TM-2012-217262, Glenn Research Center, Cleveland, Ohio, USA.

[21] Lee, D. and Kim, D., 2011, “Design and Performance Prediction of Hybrid Air Foil Thrust Bearings,” ASME J. Eng. Gas Turbines Power, **133**, pp. 1-13.

[22] Xu, F. and Kim, D., 2016, “Three-Dimensional Turbulent Thermo-Elastohydrodynamic Analyses of Hybrid Thrust Foil Bearings using Real Gas Model,” Proc. ASME Turbo Expo, Seoul, South Korea, GT2016-57766, pp. 1-10.

[23] Kim, T.H., Lee., Y.B., Kim, T.Y. and Jeong, K.H., 2012, “Rotordynamic Performance of an Oil-Free Tubo Blower Focusing on Load Capacity of Gas Foil Thrust Bearings,” ASME J. Eng. Gas Turbines Power, **134**, pp.1-7.

[24] Feng, K., Liu, L.J., Guo, Z.Y. and Zhao, X.Y., 2015, “Parametric Study on Static and Dynamic Characteristics of Bump-Type Gas Foil Thrust Bearing for Oil-free Turbomachinery,” IMechE J. Eng. Trib., **229** (10), pp. 1247-1263.

[25] Hunsberger, A., Walton II, J.F. and Heshmat, H., 2015, “Debris Tolerant Compliant Foil Bearings for High-Speed Turbomachines,” Proc. ASME Turbo Expo, Montreal, Canada, GT2015-43712, pp. 1-12.

[26] Kim, T.H., Park, M.S., Lee, J. Kim, Y.M, Ha, K.K., Park, J., Lee, C. and Kim, C., 2016, “Identification of Dynamic Characteristics of Gas Foil Thrust Bearings Using Base Excitation,” Proc. ASME Turbo Expo, Seoul, South Korea, GT2016-56282, pp. 1-10.

[27] Xu, F., Kim, D. and Yazdi, B.Z., 2016, “Theoretical Study of Top Foil Sagging Effect on the Performance of Air Thrust Foil Bearing,” Proc. ASME Turbo Expo, Seoul, South Korea, GT2016-56493, pp. 1-10.

[28] Somaya, K., Yoshimoto, S., and Miyatake, M., 2009, “Load Capacity of Aerodynamic Foil Thrust Bearings Supported by Viscoelastic Material,” Proc. Inst. Mech. Eng., Part J, **223** (4), pp. 645–652.

[29] Zheng, Y., Lai, T., Chen, S, Chen, L., Liu, L. and Hou, Y., 2016, “Static Characteristics of Six Pads Multilayer Protuberant Foil Thrust Bearings,” Proc. Inst. Mech. Eng., Part J, **0** (0), pp. 1-7.

[30] Lai, T., Wang, W., Chen, S. and Hou, Y., 2017, “Elastro-hydrodynamic Lubrication Model of Multi-decked Foil Thrust Bearing with Copper Wire Support,” J. Material Science and Technology, **31** (9), pp. 4371-4379.

[31] Pinkus, O., Thermal Aspects of Fluid Film Tribology, AMSE Press, 345 East 47th St., New York, NY.

[32] Salehi, M., Swanson, E. and Heshmat, H., 2000, “Thermal Features of Compliant Foil Bearings – Theory and Experiments,” ASME J. Trib., **123**, pp. 566-571.

[33] Radil, K. and Zeszotek, M., 2004, “An Experimental Investigation into the Temperature Profile of a Compliant Foil Air Bearing,” Trib. Trans., **47**, pp. 470-479.

[34] Dykas, B. and Radil, K., 2005, “Experimental Measurement of Thrust Foil Bearing Temperature Profiles,” Proc. World Tribology Conference III, Washington, D.C., USA, WTC2005-63564, pp. 1-2.

[35] Kim, T.H., Breedlove, A. and San Andrés, L., 2009, “Characterization of a Foil Bearing Structure at Increasing Temperatures: Static Load and Dynamic Force Performance,” ASME J. Trib., **131**, pp. 1-9.

[36] San Andrés, L. and Kim, T.H., 2010, “Thermohydrodynamic Analysis of Bump Type Foil Bearings: A Model Anchored to Test Data,” ASME J. Eng. Gas Turbines Power, **132**, pp. 1-10.

[37] San Andés, L., Ryu, K. and Kim., T.H., 2011, “Thermal Management and Rotordynamic of a Hot Rotor-Gas Foil Bearings System -Part I: Measurements,” ASME J. Eng. Gas Turbines Power, **133**, pp. 1-10.

[38] San Andés, L., Ryu, K. and Kim., T.H., 2011, “Thermal Management and Rotordynamic of a Hot Rotor-Gas Foil Bearings System -Part II: Predictions Versus Test Data,” ASME J. Eng. Gas Turbines Power, **133**, pp. 1-8.

[39] Ryu, K. and San Andés, L., 2013, “On the Failure of a Gas Foil Bearing: High Temperature Operation Without Cooling Flow,” ASME J. Eng. Gas Turbines Power, **135**, pp. 1-10.

[40] Lee, D. and Kim, D., 2010, “Thermohydrodynamic Analyses of Bump Air Foil Bearings with Detailed Thermal Model of Foil Structures and Rotor,” ASME J. Trib., **132**, pp 1-12.

[41] Lee, D. and Kim, D., 2011, “Three-Dimensional Thermohydrodynamic Analyses of Rayleigh Step Air Foil Thrust Bearing with Radially Arranged Bumps,” Trib. Trans., **54**, pp. 432-448.

[42] Lehn, A., Mahner, M. and Schweizer, B., 2018, “A Thermo-Elasto-Hydrodynamic Model for Air Foil Thrust Bearings Including Self-Induced Convective Cooling of the Rotor Disk and Thermal Runaway,” Trib. Int., **119**, pp. 281-298.

[43] Lehn, A., 2017, “Air Foil Thrust Bearings: A Thermo-Elasto-Hydrodynamic Analysis,” Ph.D. Dissertation, Technical University of Darmstadt, Darmstadt, Germany.

[44] Rieken, M., Mahner, M. and Schweizer, B., 2019, “Thermal Optimization of Air Foil Thrust Bearings Using Different Foil Materials,” ASME Turbo Expo, Phoenix, Arizona, USA, GT2019-91207, pp 1-10.

[45] Qin, K., Jacobs, P.A., Keep, J.A., Li, D. and Jahn, I.H., 2018, “A Fluid-Structure-Thermal Model for Bump-Type Foil Thrust Bearings,” Trib. Int., **121** pp. 481-491.

[46] Qin, K., “Development and Application of Multiphysics Simulation Tools for Foil Thrust Bearings Operating with Carbon Dioxide,” Ph.D. Dissertation, The University of Queensland, Brisbane, Australia.

[47] Hara, F., 1992, “Characteristics of Steel Wire Mesh Friction Damping,” ASME PVP, **229**, pp. 155-161.

[48] Al-Khateeb, E.M. and Vance, J.M., 2001, “Experimental Evaluation of a Metal Mesh Bearing Damper in Parallel with a Structural Support,” Proc. ASME Turbo Expo, New Orleans, Louisiana, USA, 2001-GT-0247, pp. 1-7.

[49] Al-Khateeb, E.M., 2002, “Design, Modeling and Experimental Investigation of Wire Mesh Vibration Dampers,” PhD Dissertation, Texas A&M University, College Station, Texas.

[50] Ertas, B.H. and Luo, H., 2008, “Nonlinear Dynamic Characterization of Oil-Free Wire Mesh Dampers,” ASME J. Eng. Gas Turbines Power, **130**, pp. 1-8.

[51] Ertas, B.H., Luo, H. and Hallman, D., 2009, “Dynamic Characteristics of Shaper Memory Alloy Mesh Dampers,” 50th AIAA/ASME/ASCE/AHS/ASC Structures, Structural

Dynamics, and Materials Conference, Palm Springs, California, USA, AIAA 2009-2521, pp. 1-8.

[52] San Andrés, L. Chirathadam, T.A. and Kim, T.H., 2010, “Measurement of Structural Stiffness and Damping Coefficients in a Metal Mesh Foil Bearing,” ASME J. Eng. Gas Turbines Power, **132**, pp. 1-7.

[53] Feng, K., Liu, Y., Zhao, X. and Liu, W., 2016, “Experimental Evaluation of the Structure Characterization of a Novel Hybrid Bump-Metal Mesh Foil Bearing,” ASME J. Trib., **138**, pp. 1-9.

[54] Feng, K., Zhao, X., Zhang, Z. and Zhang, T., 2016, “Numerical and Compact Model of Metal Mesh Foil Bearings,” Trib. Trans., **59** (3), pp. 480-490.

[55] Zhang, K., Zhao, X., Feng, K. and Zhao, Z., 2018, “Thermodydrodynamic Analysis and Thermal Management of Hybrid Bump-Metal Mesh Foil Bearings: Experimental Tests and Theoretical Predictions,” Int. J. Thermal Sciences, **127**, pp. 91-104.

[56] Cable, T.A. and San Andrés, L., 2018, “On the Design, Manufacture and Premature Failure of a Metal Mesh Thrust Bearing: How Concepts that Work on Paper, Actually Do Not,” ASME J. Eng. Gas Turbines Power, **140** (12), pp. 1-13.

[57] Rayleigh, L., 1918, “Notes on the theory of lubrication,” Philosophical Magazine, Series 6, **35** (205), pp. 1–12.

[58] Archibald, F.R. and Hamrock, B.J., 1967, “The Rayleigh Step Bearing Applied to a Gas-Lubricated Journal of Finite Length,” ASME J. Lub. Tech., January, pp. 38-46.

[59] Maday, C.J., 1968, “The One-Dimensional Optimum Hydrodynamic Gas Slider Bearing,” ASME J. Lub. Tech., January, pp. 281-284.

[60] Wylie, G.M. and Maday, C.J., 1970, “The Optimum One-Dimensional Hydrodynamic Gas Rayleigh Step Bearing,” ASME J. Lub. Tech., July, pp. 504-508.

[61] Beckwith, T.G, Marangoni, R.D. and Lienhard V, J.H., 2007, *Mechanical Measurements*, 6th Ed., Pearson Education, Inc., Upper Saddle River, NJ, ch. 3.

[62] White, F. M., 1994, Fluid Mechanics, McGraw-Hill, New York, Appendix A.

[63] Chirathadam, T.A., 2012, “Metal Mesh Foil Bearings: Prediction and Measurement of Static and Dynamic Forced Performance Characteristics,” Ph.D. Dissertation, Mechanical Engineering Dept., Texas A&M University, College Station, TX.

[64] Reddy, J.N., 1993, An Introduction to the Finite Element Method, McGraw Hill, Singapore, pp. 516-520.

[65] San Andrés, L., 2010, *Modern Lubrication Theory*, “A Thermohydrodynamic Bulk-Flow Model for Fluid Film Bearings,” Notes 10, Texas A&M University Digital Libraries, [07/2017].

[66] Faria, M. and San Andrés, L., 2000, “On the Numerical Modeling of High Speed Hydrodynamic Gas Bearings,” ASME J. Trib., **122** (1), pp.124-130.

[67] San Andrés, L., 2010, *Modern Lubrication Theory*, “Gas Film Lubrication,” Notes 15, Texas A&M University Digital Libraries, [07/2017].

[68] Gad, A.M. and Kaneko, S., 2014, “A New Structural Stiffness Model for Bump-Type Foil Bearings: Application to Generation II Gas Lubricated Foil Thrust Bearing,” ASME J. Trib., **136**, pp. 1-13.

[69] Gad, A.M. and Kaneko, S., 2016, “Tailoring of the Bearing Stiffness to Enhance the Performance of Gas-Lubricated Bump-Type Foil Thrust Bearing,” Proc. IMechE Part J: J. Eng. Trib., **230** (5), pp. 541-560.

[70] Le Lez, S., Arghir, M. and Frene, J., 2007, "A New Bump-Type Foil Bearing Structure Analytical Model," ASME J. Gas Turbines Power, **129**, pp. 1-11.

[71] Feng, K. and Kaneko, S., "Analytical Model of Bump-Type Foil Bearings Using a Link-Spring Structure and a Finite-Element Shell Model," ASME J. Trib, **132**, pp. 1-11.

[72] Bejan, A. and Kraus, A., 2003, Heat Transfer Handbook, Volume 1, John Wiley & Sons, Inc., Hoboken, New Jersey, Ch 11.

[73] Latour, B., Bouvier, P. and Harmand, S., 2011, "Convective Heat Transfer on a Rotating Disk with Transverse Air Crossflow," ASME J. Heat Transf., **133** (2), pp. 1-10.

[74] aus der Wiesche, S., 2006, "Heat Transfer from a Rotating Disk in a Parallel Crossflow," Int. J. Thermal Sciences, **46**, pp. 745-754.

[75] Eckert, E.R. and Irvine, T.F. Jr., 1960, "Pressure Drop and Heat Transfer in a Duct with Triangular Cross Section," ASME J. Heat Transf., **82** (2), pp. 125-136.

[76] Li, C. and Peterson, G.P., 2006, "The Effective Thermal Conductivity of Wire Screen," Int. J. Heat Mass Transf., **49**, pp. 4095-4105.

[77] Chang, W.S., 1990, "Porosity and Effective Thermal Conductivity of Wire Screens," ASME J. Heat Transf., **112**, pp. 1-5.

[78] Hsu, C.T., Wong, K.W., and Cheng, P., 1996, "Effective Stagnant Thermal Conductivity of Wire Screens," J. Thermophysics, **10** (3), pp. 1-4.

[79] Pellé, J. and Harmand, S., 2009, "Heat Transfer Study in a Rotor-Stator System Air-Gap with an Axial Inflow," J. Applied Thermal Eng., **29**, pp. 1532-1543.

[80] Arghir, M., 2015, "About the Stiffness of Bumps in Aerodynamic Foil Bearings," 70th STLE Conference, Dallas, TX, USA, May, pp. 1-19.

APPENDIX A

AN INTERMEDIATE PEDESTAL FOR A FOIL THRUST BEARING TEST RIG

As described at the end of Chapter 5, during testing with a foil thrust bearing, the heavy steel thrust collar decoupled from the electric motor, causing severe damage to the collar, but luckily, nothing else. This failure highlights a poor initial design, coupling the steel thrust collar directly to the electric motor. Even when dynamically balanced, the rotor collar has a short shaft which fit into the rotor collet nut, not providing a large surface area to grip. Over time, the collet and nut fatigue due to cycles of tightening and loosening, creating a dangerous situation.

Figure A1 displays an isometric view of a ball bearing pedestal and rotating shaft for a thrust bearing test rig. The rotating shaft is coupled to an electric motor (40 krpm max) via an elastic coupling and secondary shaft. A test thrust bearing (not pictured) applies a thrust load (1.3 kN max) to the rotating shaft (from left to right) and reacted by a set of angular contact ball bearings in the front and a spring preloaded bearing in the back.

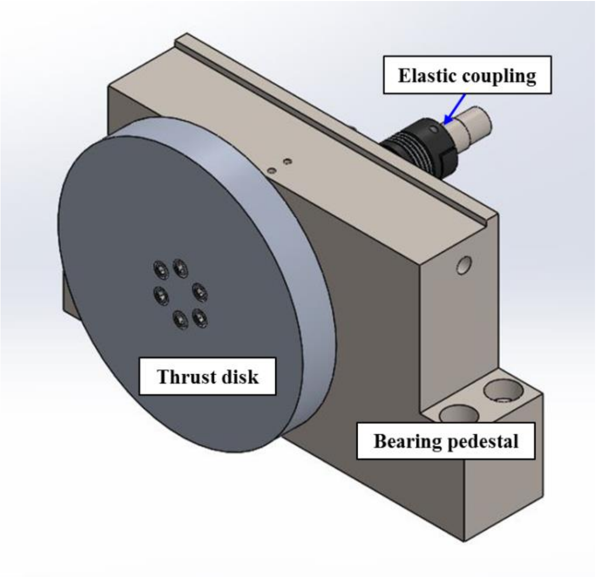

Figure A1. Isometric view of a ball bearing pedestal and rotating shaft assembly.

This intermittent pedestal serves several purposes:

1. The ball bearings in pedestal absorb the thrust load imposed by the test bearing, rather than the ceramic ball bearings in the electric motor.
2. The elastic coupling provides a fail-safe in the event of a rotor-touchdown and bearing seizure event.
3. The bearing pedestal itself provides an opportunity to machine a precison surface to use as a datum when aligning the test bearing and rotor collar.
4. The secondary shaft, which couples to the electric motor via a collet and nut, has a small diameter and can be machined from a small piece of bar stock, saving on machining costs.

Figure A2 displays a cut section view of the pedestal, indicating the direction of the thrust load as well as the load path through the ball bearings and a list of the individual components in the assembly. The hybrid ceramic ball bearings pictured in Figure A2 are grease packed and rated to 60 krpm. Despite the manufacturer guarantee, the pedestal contains two access holes to the bearings, which should contain thermocouples to monitor the bearing health during operation.

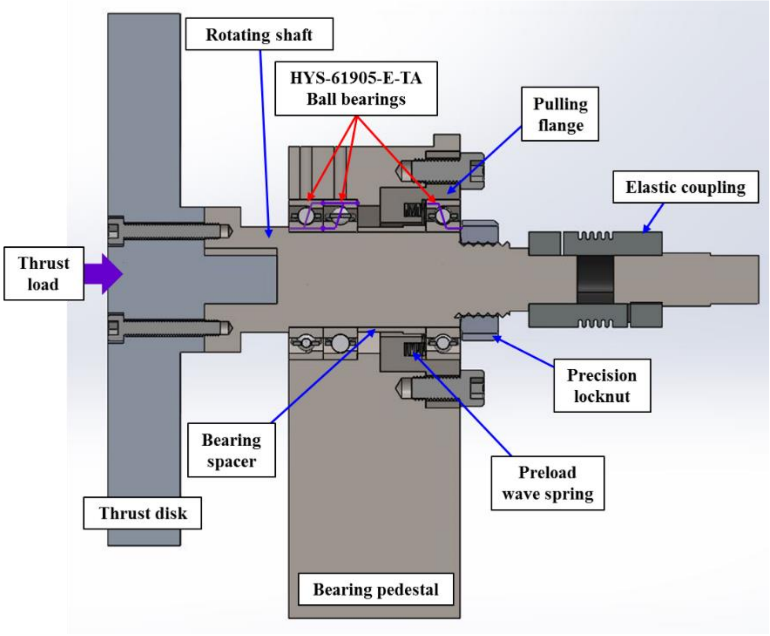

Figure A2. Cut section view of a bearing pedestal and rotating shaft assembly indicating the direction of the thrust load and load path through the ball bearings.

Figure A3 displays an exploded cut section view of the bearing pedestal and the rotating shaft assembly. First, the front two bearing press onto the rotating shaft, up to the machined shoulder. Next, the bearing spacer presses onto the shaft, up to the inner race of the second ball bearing. After the front bearing assemble on the shaft, the thrust disk bolts onto the rotating shaft, and the assembly slides into the pedestal. Once the assembly locates in the pedestal, the pulling flange installs into the pedestal and a preload wave spring inserts over the shaft, seating in the flange. Finally, the back bearing presses onto the shaft and a precision locknut fixes the assembly in place.

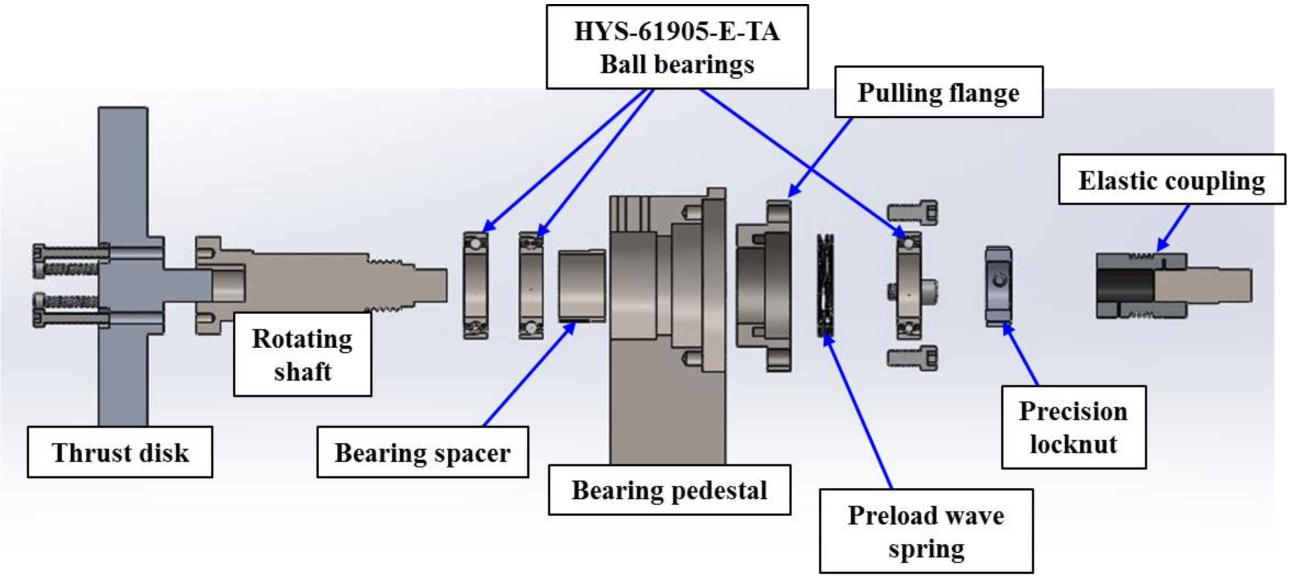

Figure A3. Exploded cut view of a bearing pedestal and rotating shaft assembly.

APPENDIX B

HEAT TRANSFER COEFFICIENTS

B.1 CONVECTION FROM THE FLUID FILM TO BOUNDING SOLIDS

Figure B1 displays a single bearing pad, with a thin film of air (highlighted in red) between the thin top foil and the thrust collar surface (not pictured). The top foil and thrust collar remain parallel (for the most part) during operation. Thus, the geometry can be approximated as a parallel plate channel for the purposes of determining an appropriate heat transfer coefficient ($\bar{h}$).

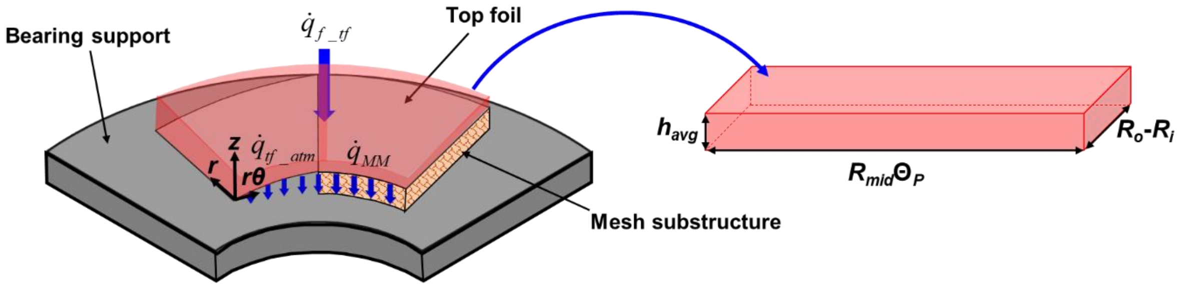

Figure B1. Schematic of a single bearing pad approximated as a parallel plate channel.

A hydraulic diameter is defined as four times the wetted cross-sectional area, divided by the wetted perimeter; and for the parallel channel from Figure A1, the hydraulic diameter equals to

$$D_h = \frac{4A}{P} = \frac{4\left\{h_{avg}\left(R_o - R_i\right)\right\}}{2\left\{h_{avg} + \left(R_o - R_i\right)\right\}} = 2\left\{\frac{h_{avg}\left(R_o - R_i\right)}{h_{avg} + \left(R_o - R_i\right)}\right\} \tag{B.1}$$

With a defined hydraulic diameter, and a known fluid thermal conductivity, a convection coefficient can be extracted from an empirical Nusselt number

$$\bar{h} = \mathrm{Nu}\left(\frac{\kappa}{D_h}\right) \tag{B.2}$$

The Nusselt number for thermally and hydrodynamically developing laminar flow and constant wall temperatures (Hausen model) is given by Ref. [72] as

$$\mathrm{Nu} = 3.657 + \frac{0.19\left(\mathrm{Re}\,\mathrm{Pr}\,\frac{D_h}{L}\right)^{4/5}}{1+0.117\left(\mathrm{Re}\,\mathrm{Pr}\,\frac{D_h}{L}\right)^{0.467}} \tag{B.3}$$

where Re is the local Reynolds number, Pr is the Prandtl number $\left(\mathrm{Pr} = c_p\mu/\kappa\right)$, D_h is the hydraulic diameter and L is a characteristic length ($L = R_{mid}\Theta_P$ for the channel from Figure B1).

Reynolds numbers towards the thrust collar and top foil surfaces are defined with the mean fluid flows (Eq. (7)), i.e.

$$\begin{aligned}\mathrm{Re}_{f\_TC} &= \frac{\rho_f h}{\mu_T}\left[\left(\bar{U}_r - U_{r(z=h)}\right)^2 + \left(\bar{U}_\theta - U_{\theta(z=h)}\right)^2\right]^{\frac{1}{2}} = \frac{\rho_f h}{\mu_T}\left[\bar{U}_r^2 + \left(\bar{U}_\theta - r\Omega\right)^2\right]^{\frac{1}{2}} \\ \mathrm{Re}_{f\_tf} &= \frac{\rho_f h}{\mu_T}\left[\left(\bar{U}_r - U_{r(z=0)}\right)^2 + \left(\bar{U}_\theta - U_{\theta(z=0)}\right)^2\right]^{\frac{1}{2}} = \frac{\rho_f h}{\mu_T}\left[\bar{U}_r^2 + \bar{U}_\theta^2\right]^{\frac{1}{2}}\end{aligned} \tag{B.4}$$

Substitution of the Reynolds numbers from Eqs. (B.4) into Eq. (B.2) renders heat convection coefficients towards the thrust collar and top foil as

$$\bar{h}_{f\_TC} = \mathrm{Nu}_{f\_TC}\left(\frac{\kappa_f}{D_h}\right),\ \bar{h}_{f\_tf} = \mathrm{Nu}_{f\_tf}\left(\frac{\kappa_f}{D_h}\right) \tag{B.5}$$

B.2 CONVECTION COEFFICIENTS FOR A ROTATING CYLINDER

As mentioned in the body of the report, heat transfer between the thrust collar's surface and atmosphere occurs through convection and is characterized with an empirical Nusselt number. Several researchers [73,74] discuss heat transfer from a rotating disk to a quiescent media. Ref. [45] uses a mean heat transfer coefficient for the entire disk surface, defined as

$$\mathrm{Nu}_m = \frac{\bar{h}_m R_o}{\kappa} \tag{B.6}$$

For laminar and turbulent flows, the Nusselt number is

$$\mathrm{Nu}_m = \begin{cases} 0.33 \cdot \mathrm{Re}_\omega^{1/2} & \mathrm{Re}_\omega \le 2\times10^5 \\ 0.015 \cdot \mathrm{Re}_\omega^{0.8} & \mathrm{Re}_\omega \ge 5\times10^5 \end{cases} \tag{B.7}$$

where the rotational Reynolds number

$$\mathrm{Re}_\omega = \frac{\omega R_o^2 \rho_{atm}}{\mu_{atm}} \tag{B.8}$$

Refs. [44,74] include the media Prandtl number as well as a transitional regime, where the flow moves between laminar and turbulent. Aus def Weische [74] defines the Nusselt number for discrete points along the disk surface, i.e.

$$\mathrm{Nu}_r = \begin{cases} 0.33 \cdot \mathrm{Re}_\omega^{1/2} \cdot \mathrm{Pr}^{1/3} & \mathrm{Re}_\omega < 1.95\times10^5 \\ 10 \cdot 10^{-20} \cdot \mathrm{Re}_\omega^{4} \cdot \mathrm{Pr}^{1/3} & 1.95\times10^5 \le \mathrm{Re}_\omega \le 2.5\times10^5 \\ 0.0188 \cdot \mathrm{Re}_\omega^{4/5} \cdot \mathrm{Pr}^{1/3} & \mathrm{Re}_\omega > 2.5\times10^5 \end{cases} \tag{B.9}$$

Where the Nusselt number and rotational Reynolds number are both determined via the radial location (r) along the disk surface

$$\mathrm{Re}_\omega = \frac{\omega \cdot r^2 \rho_{atm}}{\mu_{atm}} \quad \text{and} \quad \mathrm{Nu}_r = \frac{\bar{h}_r r}{\kappa} \tag{B.10}$$

Figure B2 displays the heat convection coefficient ($\bar{h}_r$ or $\bar{h}_m$) versus radial location for a disk with an outer radius R_O = 50.8 mm operating with a rotational speed Ω = 21 krpm (ω ~ 2,200 rad/s) and in air at standard conditions (P_a = 101.4 kPa, T_a = 300 K). For the operating conditions (Ω = 21 krpm), $\mathrm{Re}_\omega = 3.81\cdot10^5$ and the flow over the disk surface is turbulent. The mean heat transfer coefficient is significantly larger than that given by Eqs. (B.9) & (B.10). Considering the discrete heat transfer coefficient ($\bar{h}_r$) along the disk surface, the transition occurs at ~ 3/4 of the disk radial length, and it turbulent for ~ 1/5 of the collar surface. The current analysis utilizes the correlations from aus der Wiesche [74] for the disk heat convection coefficients along the back surface and outer diameter.

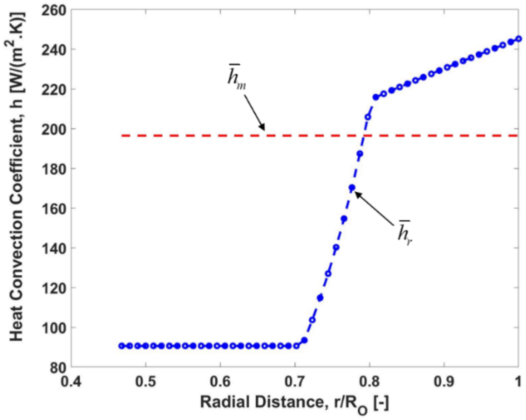

Figure B2. Convection coefficient for a rotating disk in a quiescent media.

In addition to the heat transfer from the backside of the disk, when cooling flow applies to the bearing through the center of the support shaft the cooling flow jet impinges on the thrust collar’s front face, moving radially outwards through the areas between bearing pads as well as the areas under the pads tapers. Pellé & Harmond [79] give correlations for the mean Nusselt number for a disk with a round cooling flow jet impinging on its surface, as a function of the cooling flow Reynolds number ($\mathrm{Re}_{cf} = \rho_{cf} U_{cf} D_{cf} / \mu_{cf}$), the distance between the cooling flow jet and the disk surface ($G = t_{BS} + t_{MM} / R_{TC}$) and the disk rotational Reynolds number ($\mathrm{Re}_{\omega} = \omega R_o^2 \rho_{atm} / \mu_{atm}$), i.e.

$$\mathrm{Nu}_r = \begin{cases} 0.08 \cdot G^{-0.07} \cdot \mathrm{Re}_{cf}^{0.5} \cdot \mathrm{Re}_{\omega}^{.25} & 0.01 \le G < 0.04 \\ 0.006 \cdot G^{0.15} \cdot \mathrm{Re}_{cf}^{0.5} \cdot \mathrm{Re}_{\omega}^{0.5} & 0.04 \le G < 0.08 \\ 0.06 \cdot \mathrm{Re}_{cf}^{0.5} \cdot \mathrm{Re}_{\omega}^{0.5} & 2.5 \times 10^5 < G \end{cases} \tag{B.11}$$

The current analysis utilizes a cooling flow inlet diameter D_{cf} = 6.35 mm and a bearing support thickness t_{BS} = 9.525 mm, which gives $400 \leq \overline{h}_m \leq 700$ W/m^{2}K for the front of the thrust collar and for cooling flows comprised between 100 and 1,000 LPM.

B.3 CONVECTION COEFFICIENT UNDERNEATH A TAPERED PAD

Figure B3 reproduces the schematic of a single MMFTB pad from Figure 37. Note that the area beneath the tapered portion of the top foil resembles a right triangle with inclination angle α, length $R_{mid}\theta_t$ and height t_{MM}.

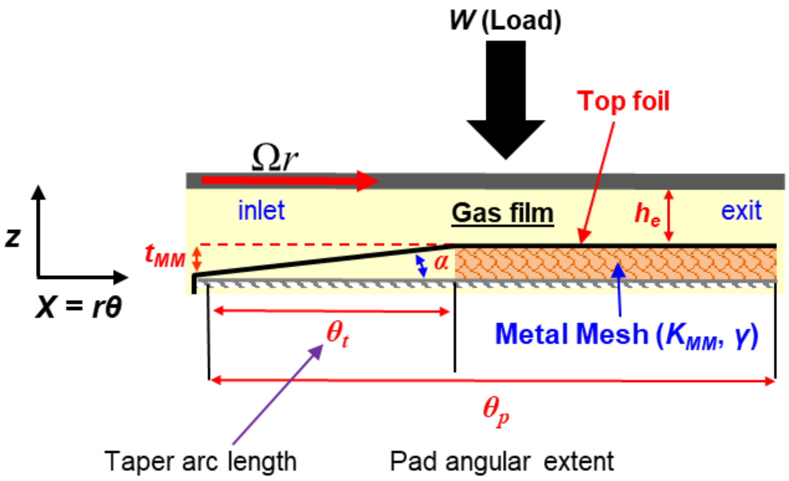

Figure B3. Schematic of a single pad tapered metal mesh foil thrust bearing.

Ref. [75] gives Nusselt numbers for triangular ducts for three types of boundary conditions and for laminar and turbulent flow conditions. The Reynolds number for flow in the duct utilizes a mean flow velocity, such that

$$\mathrm{Re}_{cf} = \frac{\dot{m}_{cf} D_h}{A_{taper} \mu} \tag{B.12}$$

where the mean cooling flow velocity for the current analysis is and the hydraulic diameter for the tapered portion of the top foil is

$$D_H = \frac{2 t_{MM} R_{mid} \theta_{taper}}{\left[t_{MM} + R_{mid} \theta_{taper} + \left\{ t_{MM}^2 + \left(R_{mid} \theta_{taper} \right)^2 \right\}^{\frac{1}{2}} \right]} \tag{B.13}$$

A linear fit of the experimental data in [69] gives the Nusselt number for a duct with a triangular cross-section as

$$\mathrm{Nu} = 0.0325\,\mathrm{Re}^{0.66} \tag{B.14}$$

Since the tapered portion of the top foil only represents half of an isosceles triangle, the Nusselt number from Eq. (B.11) divides by 2. In addition, when no cooling flow applies to the test bearing, convective heat transfer in the tapered portion occurs via natural convection, with a heat transfer coefficient $\overline{h}_{cf} = 10 \left[\mathrm{W}/\left(\mathrm{m.K} \right) \right]$ [35].

B.4 EFFECTIVE HEAT TRANSFER COEFFICIENT FOR METAL MESH LAYERS

Heat transfer through wire screens (mesh) saturated with a stagnant (or flowing) fluid is a prevalent topic in the literature. Ref. [76] provides a comprehensive review of the literature dedicated to heat transfer through mesh structures, showing that the effective thermal conductivity of sintered (i.e. bonded) mesh structures can be as high as $0.5 \cdot \kappa_{material}$. However, for a single layer of mesh, or stacks of unbonded layers, diminished contact area between wires significantly decreases the effective thermal conductivity of the entire structure.

Chang [77] provides a detailed lumped parameter model for the effective thermal conductivity of mesh structures as well as a comparison to published data. Figure B4 displays a schematic showing a layer of mesh as well as what the authors refer to as a unit cell (dashed area in the figure).

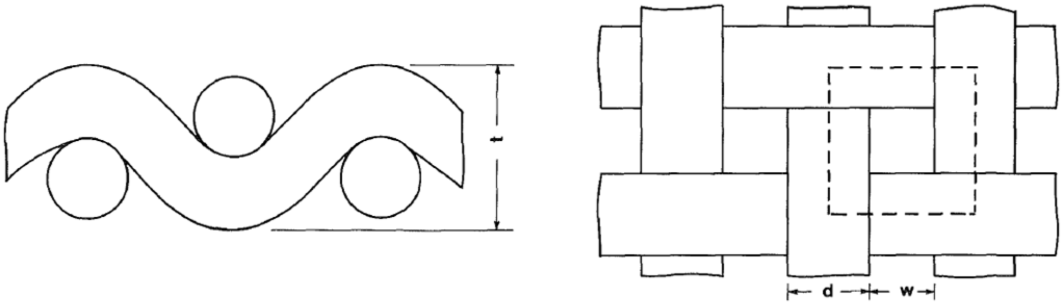

(a) Front view (b) Top view

Figure B4. Front and top views of a section of a metal mesh layer made of wires having circular cross sections [77].

By considering the dimensions of the mesh, along with the contact conditions in each section of the unit cell, the authors develop an equivalent thermal conductivity for the layer based on thermal resistances in series and parallel. Hsu *et al.* [78] extend the model of Chang [77] to include a parameter for the contact condition (which increases with applied load and bonding such as sintering) between wires. Hsu *et al*. give the effective thermal conductivity of a mesh layer as

$$\frac{\kappa_e}{\kappa_f} = \left(1-\gamma_{ay}\right)\left(1-\gamma_{ax}\right) + \frac{\left(\gamma_{ax}+\gamma_{ay}-2\gamma_{ax}\gamma_{ay}\right)}{\gamma_{bz}\left(\lambda-1\right)+1} + \frac{\gamma_{ax}\gamma_{ay}\left(1-\gamma_c^2\right)}{2\gamma_{bz}\left(\lambda-1\right)+1} + \frac{\gamma_c^2\gamma_{ax}\gamma_{ay}}{\lambda} \qquad \text{(B.15)}$$

where the parameters

$$\lambda = \frac{\kappa_f}{\kappa_s} \;,\; \gamma_{ax} = \frac{a}{l_x} \;,\; \gamma_{ay} = \frac{a}{l_y} \;,\; \gamma_{bz} = \frac{b}{l_z} \;\text{ and }\; \gamma_c = \frac{c}{a} \qquad \text{(B.16)}$$

and Figure B5 gives details on the mesh dimensions. Note that the parameters a, b relate to the amount of deformation in the individual wires, with more deformation leading to a larger contact width c.

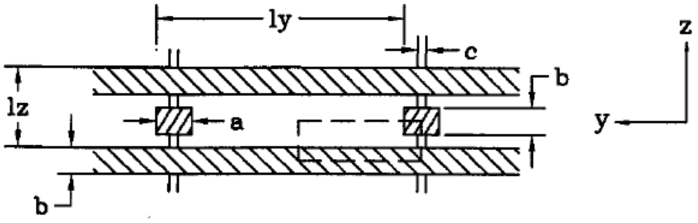

Figure B5. Schematic of a unit cell of metal mesh [78].

The 40 OPI copper mesh utilized for the experiments herein has square openings (o_w x o_w) with wires having circular cross sections (diameter w_d). Referring to the schematic in Figure B4,

$$\begin{gathered} l_x = l_y = w_d + d \\ l_z = 2d \\ a = b = \left(\pi \frac{d}{2} \right)^{1/2} \end{gathered} \tag{B.17}$$

For the copper 40 OPI mesh saturated with air at 293 K (κ_{copper} = 381 W/m.K κ_{air} = 0.025 W/m.K) and having dimensions w_d = 0.254 mm and o_w = 0.381 mm, Eq. (B.13) predicts κ_e = 0.06 - 47.91 [W/(m.K)] for a contact parameter γ_c = 0 - 1, respectively. Experiments in Ref. [78] show that a contact parameter γ_c = 0.1 yields the best correlation, and gives κ_e = 0.59 [W/(m.K)] per sheet for the 40 OPI mesh utilized for tests herein.

APPENDIX C

VALIDATION OF FOIL BEAIRNG STRUCTURAL MODEL WITH COMMERCIAL SOFTWARE

Foil bearings, both radial and thrust, experience local elastic deformations of both top-foil and underspring support during operation. As such, accurate modeling of these bearings necessitates a precise model for the bearing structural elastic deformation. Chapter 6 of this dissertation details briefly the structural model for a MMFTB, where two dimensional shells and first-order shear deformable plate theory describe the mechanics of the thin top-foil.

Figure C1 displays a schematic of a single pad bump-type foil thrust bearing while Table C1 contains its dimensions and material properties [9]. Note that the bump foil is organized into five separate strips, each with a different number of bumps, and each with a different bump-pitch. Commercial finite element software provides predictions for the displacement of the top foil, and then the top foil supported by the bump-foil strips, serving as a baseline for validating the current structural model.

Table C1. Top & bump foil geometries and material properties.

Top Foil & Bump Foil Geometry	
Bump & Top-Foil Materials	Inconel X-750
Elastic Moduli, $E_{bf,tf}$ [GPa]	213
Poisson's Ratio, v [-]	0.29
Bump Foil & Top Foil Thicknesses, $t_{BF,tf}$ [mm]	0.1016, 0.1524
Top Foil Inner and Outer Diameters, $D_{i,o}$ [mm]	50.8, 101.6
Top Foil Extent, θ_P [°]	45
Number of Bump Strips, n_{strips} [-]	5
Strip Width, w_b [mm]	5.08
Bump Strip Mean Radii, R_{mid} [mm]	28, 33, 38, 43, 48
Bump Pitches (ID to OD), b_p [mm]	5.36, 5.19, 4.65, 3.77, 5.90
Number of Bumps/Strip (ID to OD), n_{bump} [-]	3, 4, 5, 6, 5
Bump Height, h_b [mm]	0.508
Bump Radius, R_b [mm]	1.6
Coefficient of Friction, μ_{BF}	0.1

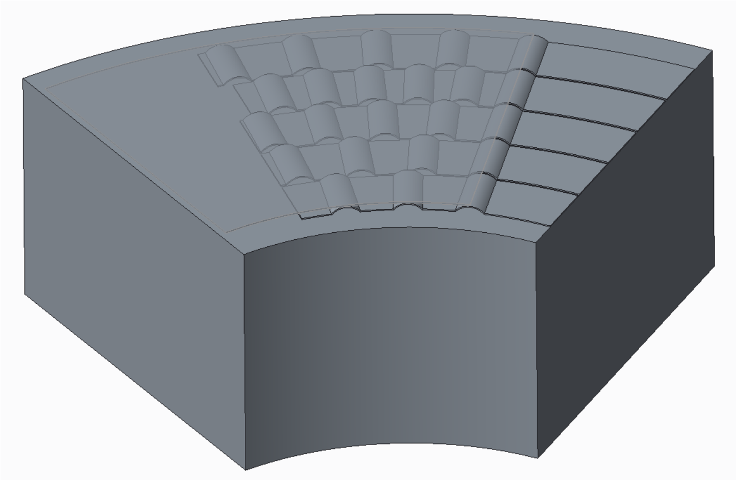

Figure C1. Schematic of a single pad bump-type foil thrust bearing pad with geometry as displayed in Table C1.

Figure C2 displays a model of the thin top foil in a commercial FE software. Eight-nodded, three-dimensional brick elements mesh the top foil 30x45x1 (radial x circumferential x transverse). The current analysis fixes the leading edge of the foil while a uniformly distributed load (*W/A* = 100 Pa) applies over 30° of its angular extent. Despite the small load, predictions displayed in Figure C3 show that the specific load (*W/A* = 100 Pa) produces a maximum foil displacement on the order of that observed in foil bearing analysis (~ 100 μm).

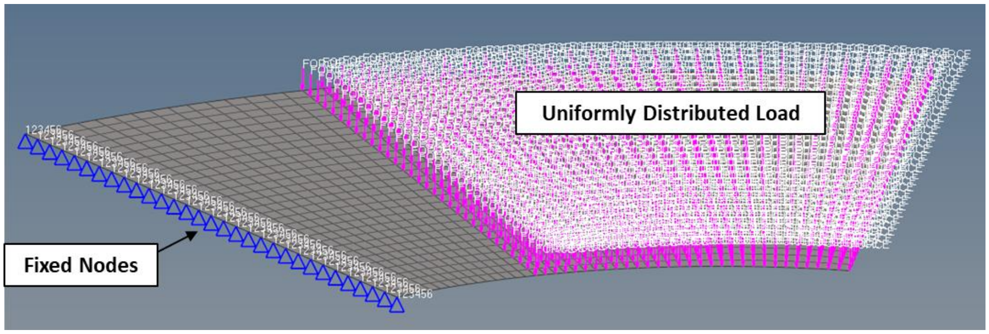

Figure C2. Finite element model of a thin top foil with geometry as displayed in Table C1.

Figure C3 displays contour plots of the top-foil displacement predicted with commercial software and also with the current model. Both methods predict similar displacements, with the maximum displacement occurring at the outer radius and at the foil trailing edge. Note that the commercial software predicts δ_{max} ~ 165 µm, while the current model predicts δ_{max} ~ 170 µm, a difference of ~ 3%. As noted in Chapter 6, the current structural model neglects membrane forces, yielding a slightly more compliant foil.

Figure C4 displays predicted top-foil displacement along the pad mid-radius (R_{mid} = 38.1 mm) versus angular location from both the commercial software and also from the current model. As mentioned, the current model slightly overpredicts the top-foil deflection (~3%). However, the agreement (both qualitative and quantitative) is sufficient for the current analysis.

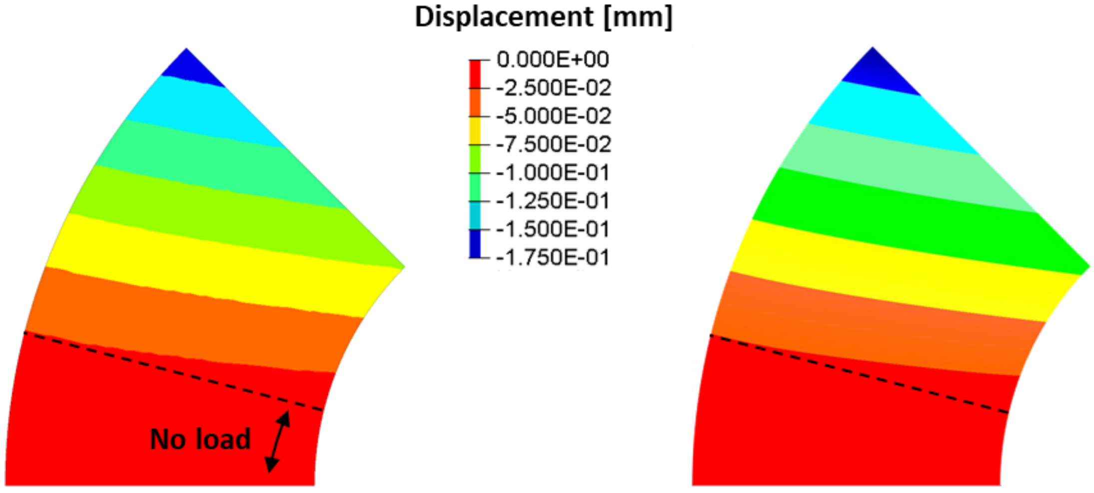

(a) Commercial software

(b) Current model

Figure C3. Contour plots of top-foil displacement for a uniform applied load over 30° of the top-foil angular extent. *W/A* = 100 Pa.

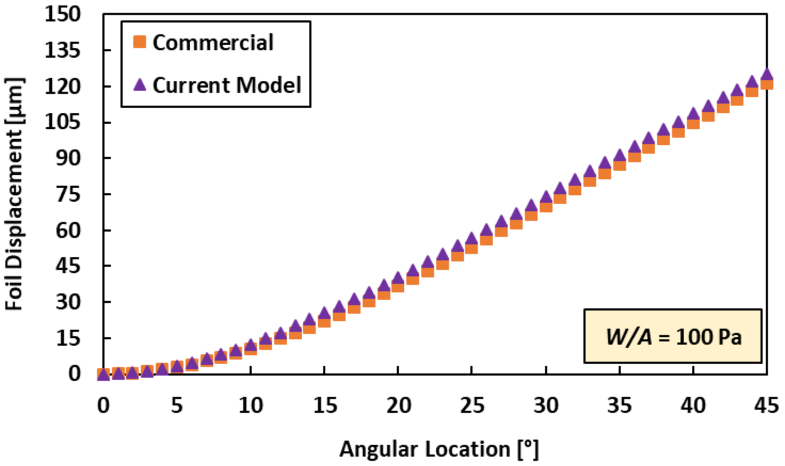

Figure C4. Top-foil deflection versus angular location at the pad mid-radius. *W/A* = 100 Pa.

Chapter 7 of this dissertation compares predictions for the steady-state performance of a metal mesh foil thrust bearing to that of a bump-type foil thrust bearing. The literature forwards several models for the structural behavior of a bump-foil, ranging from simple closed-form solutions [15] to more complicated multi-degree of freedom (MDOF) models considering bump interactions [69-71].

For the MMFTB, the current model idealizes the metal mesh screen support as a uniform stiffness which supports the thin top-foil. This approach is simple and does not require of further validation. There are several different options for the bump-foil model, however, and the chosen one should be verified. Currently, Iordanoff's closed form solution [15] provides a simple and expedient approach to determine the individual bump stiffnesses, which add to the top foil stiffness matrix at the appropriate locations. Bump foils typically affix to a bearing housing via tack-welds, such that Iordanoff (and later Arghir) forwards expressions for bump compliance (inverse of stiffness) for both the fixed and free bumps in the bump foil strip, i.e.

$$\begin{aligned} &\text{Fixed-free bump:} \quad s = \frac{12 l_0^3 i J \left(1-\nu^2\right)}{E e^3 \sin^3\left(\alpha/2\right)} \\ &\text{Free-free bump:} \quad s = \frac{6 l_0^3 i J \left(1-\nu^2\right)}{E e^3 \sin^3\left(\alpha/2\right)} \end{aligned} \tag{C.1}$$

where the parameters in Eq. (C.1) are as defined in Ref. [80]. The model herein calculates the stiffness for the fixed-free and free-free bumps according to Eq. (C.1) and assumes a linear variation for the stiffness of the in-between bumps.

As with the previous predictions, 30x45x1 (radial x circumferential x transverse) mesh the top foil while 10x52x1 elements mesh each of the five bump-foil strips. The commercial software utilizes a penalty type contact model to determine locations of bump-foil to top-foil and bump-foil to bearing support contact. In addition, the analysis considers the leading edge of the top-foil and the trailing edges of the bump-foil strips fixed, while a uniform load (*W/A* = 35 kPa) applies to the 30° of the top foil which overlaps with the bumps.

Figure C5 displays contour plots of the top-foil displacement also indicating the locations of the bump crests. The contours show large displacements in the sections before the bumps begin, and also at the pad inner and outer radii. Recall that the current model assigns the bump stiffnesses at single nodal locations, not altering these locations as the bump foil deflects. The commercial software, alternatively, solves for the lateral and vertical displacements of the bump and top foils, utilizing a contact model to determine where the structures contact. Despite the simplicity of the current model, predictions for the top-foil displacement match well with those from the commercial software.

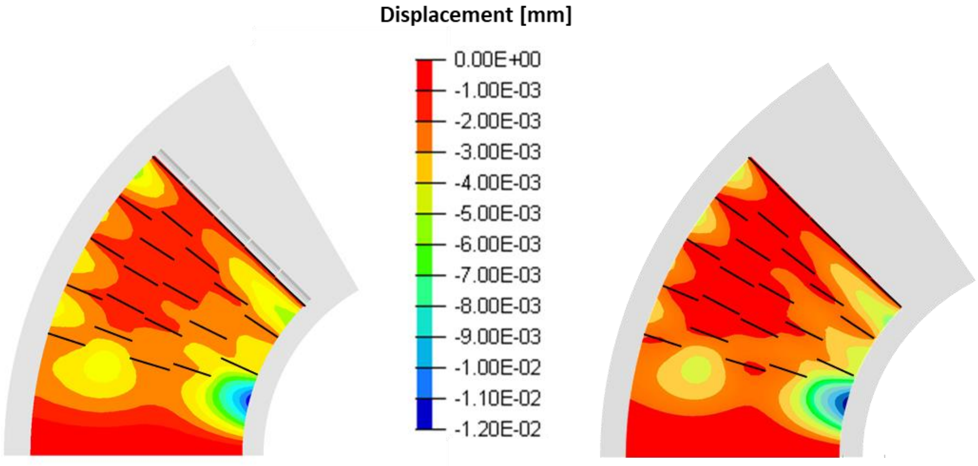

(a) Commercial software (b) Current model

Figure C5. Contour plots of top-foil displacement for a single bump-type foil thrust bearing pad with dimensions as displayed in Table C1.

Figure C6 presents top-foil displacement (at the bump-strip midspan) versus angular location predicted with commercial software as well as with the current model. As gleaned from the contour plots in the previous figure, the current model (utilizing Iordanoff''s expression for bump stiffness) delivers top-foil displacements which match well with commercial software. Strip #1, closest to the inner radius, has only three bumps, and a large bump pitch (b_P > 5 mm). As such, the displacement near the inner radius is the largest and with pronounced displacements between the bump locations (known as top-foil sag). Conversely, Strips #3 & #4 have large numbers of bumps and small bump pitches, yielding small displacements and little top-foil sag between the bumps.

During operating with a fluid film, a non-uniform pressure field develops over the pad surface, deforming the pad the most where the underspring is most flexible. As such, the bump foil design displayed in Figure C1 should have (comparatively) large deflections near the pad inner radius, while displaying smaller deflections (and therefore larger pressure) near the pad outer radius. Overall, the current model captures well the top-foil displacements under static loading conditions and is deemed acceptable for the current analysis.

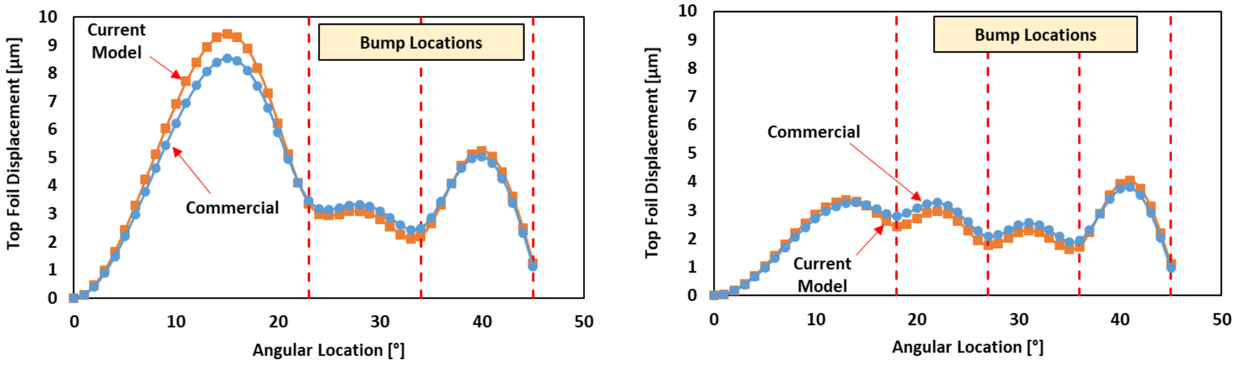

(a) Strip #1 (R_{mid} = 28 mm) (b) Strip #2 (R_{mid} = 33 mm)

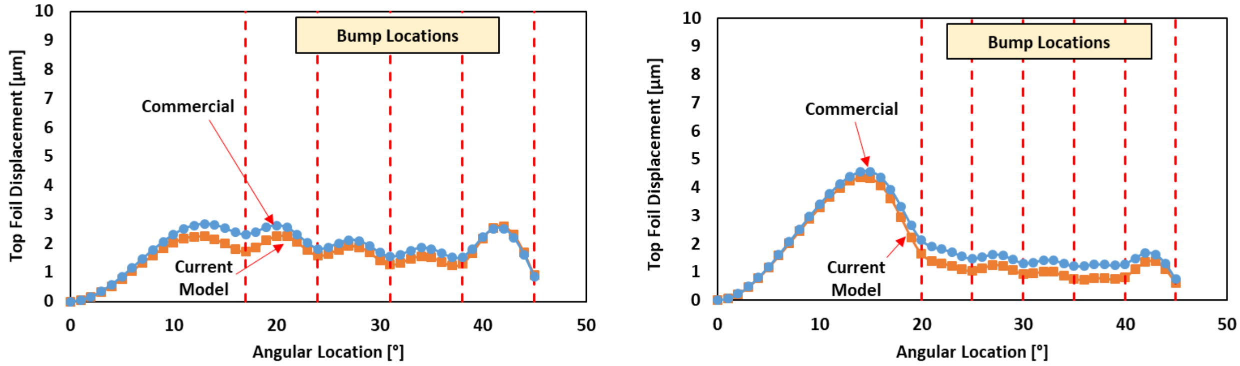

(c) Strip #3 (R_{mid} = 38 mm) (d) Strip #4 (R_{mid} = 43 mm)

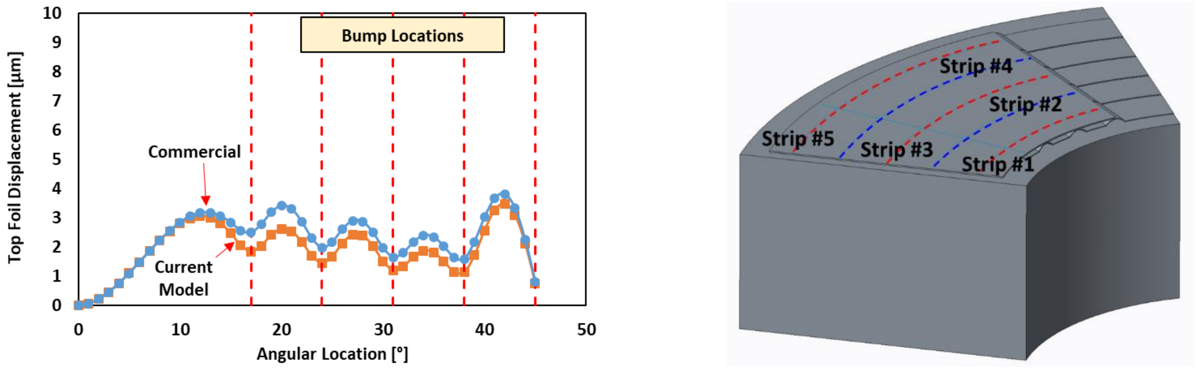

(d) Strip #5 (R_{mid} = 48 mm) (e) Strip locations

Figure C6. Predicted top-foil displacement versus angular location for a single bump-type foil thrust bearing pad with dimensions as displayed in Table C1.